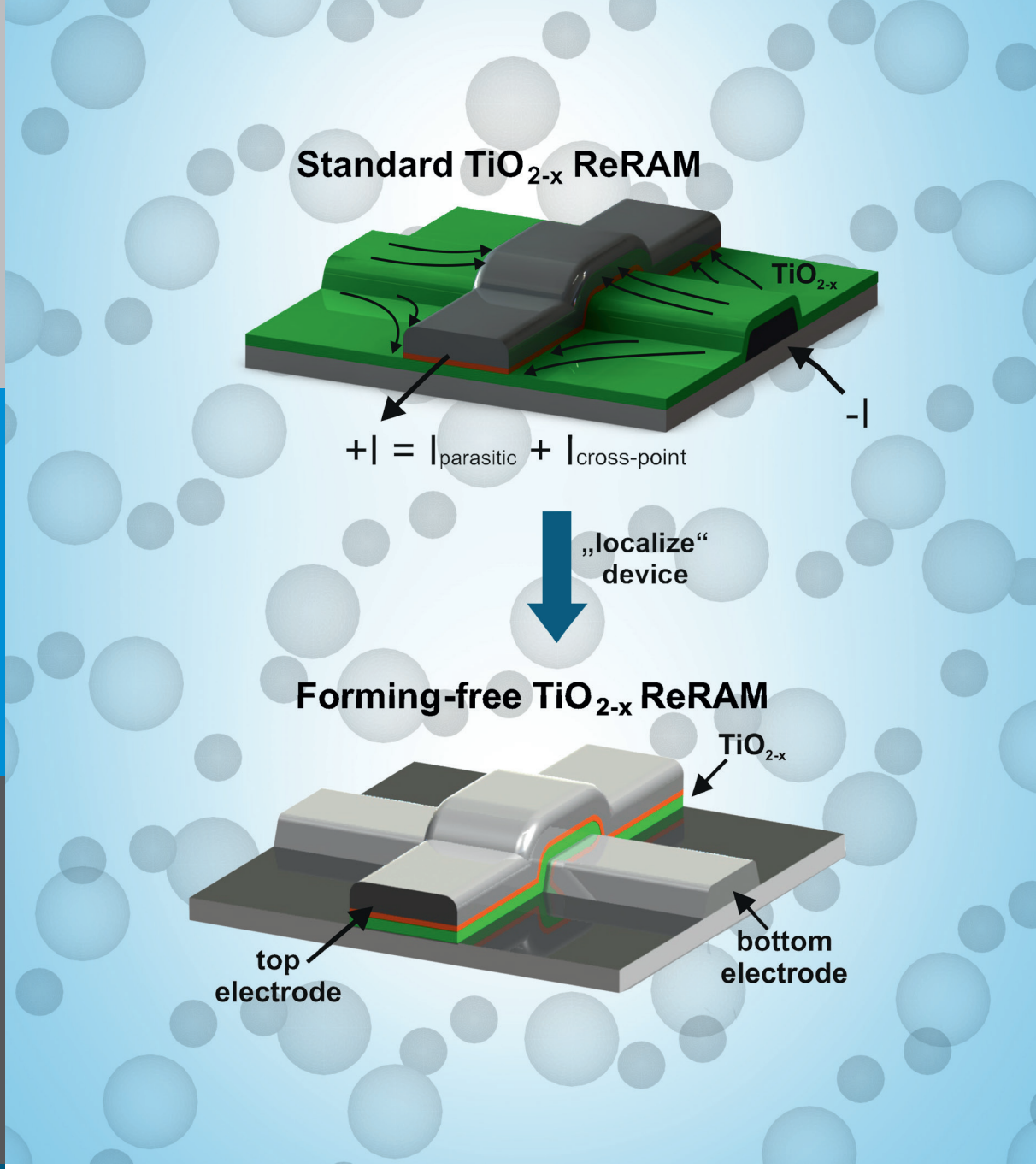

Integration and Characterization of Atomic Layer Deposited TiO_2 Thin Films for Resistive Switching Applications

Marcel Reiners

JÜLICH
FORSCHUNGSZENTRUM

Member of the Helmholtz Association

Schriften des Forschungszentrums Jülich
Reihe Information / Information Band / Volume 36

Forschungszentrum Jülich GmbH
Peter Grünberg Institute (PGI)
Elektronische Materialien (PGI-7)

Integration and Characterization of Atomic Layer Deposited TiO_2 Thin Films for Resistive Switching Applications

Marcel Reiners

Schriften des Forschungszentrums Jülich
Reihe Information / Information Band / Volume 36

ISSN 1866-1777 ISBN 978-3-89336-970-6

Bibliographic information published by the Deutsche Nationalbibliothek.
The Deutsche Nationalbibliothek lists this publication in the Deutsche Nationalbibliografie; detailed bibliographic data are available in the Internet at http://dnb.d-nb.de.

Publisher and Distributor: Forschungszentrum Jülich GmbH
Zentralbibliothek
52425 Jülich
Tel: +49 2461 61-5368
Fax: +49 2461 61-6103
Email: zb-publikation@fz-juelich.de
www.fz-juelich.de/zb

Cover Design: Grafische Medien, Forschungszentrum Jülich GmbH

Printer: Grafische Medien, Forschungszentrum Jülich GmbH

Schriften des Forschungszentrums Jülich
Reihe Information / Information, Band / Volume 36

D 82 (Diss., RWTH Aachen University, 2014)

ISSN 1866-1777
ISBN 978-3-89336-970-6

The complete volume is freely available on the Internet on the Jülicher Open Access Server (JUWEL) at www.fz-juelich.de/zb/juwel

Preface

In the last decades the commercialization of computer and multimedia applications for consumer electronics increased the desire for faster, denser, and non-volatile memory. At present, FLASH memory is the standard non-volatile memory based on complementary metal oxide semiconductor (CMOS) technology. But actual research is already dealing with concepts for the next era 'aside FLASH' or 'beyond FLASH'. Resistive random access memory (ReRAM) is one of the new candidates which has the potential candidate to replace FLASH in future. The concept of ReRAM is based on the change of the resistance state of a passive device by an electrical stimulus. Typical devices are built from chalcogenide thin films sandwiched between metallic conducting electrodes. In general, transition metal oxide based ReRAM needs an electroforming process to enable resistance switching. This is an obstacle if ready-to-use devices are required. The focus of this thesis adresses the question if it is possible to design 'forming-free' ReRAM devices by a control of TMO thin film defect structure. As a material which is intensively investigated for ReRAM applications, titanium oxide is used. TiO_2 in ready-to-use ReRAM should be oxygen deficient, and should contain a certain amount of well-conducting Magnéli-phases within a crystalline TiO_2 matrix. In addition, semiconductor industry requires a deposition method which enables precise, defect-free, shadow-free and 3D coverage by the functional layer for a stacked ReRAM architecture. These requirements are fulfilled by the atomic layer deposition (ALD) technique.

For the integration of TiO_2 into ReRAM an ALD process was investigated and further optimized to achieve the desired properties. The process parameters were elaborated to grow amorphous and crystalline TiO_2 thin films in order to study the effect of the films' morphology and structure on the resistive switching behavior. Detailed studies on the crystallization of TiO_2 while the ALD thin film growth reveal that the crystallization kinetics allow to explain the control of the phase composition of TiO_2 by the growth temperature, the thickness, and the process time. The deeper understanding of the crystallization of TiO_2 into different phases additionally revealed how to suppress the surface roughening for thicker TiO_2 layers which is an important aspect for extremely thin films. The structural investigations on crystalline grown TiO_2 reveal, that corundum Ti_2O_3 could be deposited within a matrix of rutile and anatase TiO_2. From these studies, the presence of Magnéli-type phases could deduced by thermodynamical stability considerations. ALD TiO_2 thin films of amorphous and crystalline state were integrated into nano cross-point devices to systematically study their resistive switching properties. The comparison of the transport, the electroforming, and the resistive switching measurements clearly revealed that as-deposited crystalline TiO_2 films which contain Magnéli-phases are advantageous of functioning TiO_2 based ReRAM. Crystalline TiO_2 films exhibited soft forming characteristic at low voltages which were in the range of the SET voltages of the subsequent switching hysteresis. In contraction to that, amorphous TiO_2 showed abrupt forming at higher voltages resulting in a strongly linear ON state after electroforming as compared to crystalline TiO_2. The gained knowledge on the correlation of the electrical transport properties of the pristine device state, the resistive switching properties, and the material properties of the crystalline TiO_2 was utilized to develop a new promising concept for the design of forming-free TiO_2 ReRAM. This concept involves the elimination of parasitic current paths which are linked to the well-conducting crystalline phase. By the change of the device process flow from a lift-off to a top down approach for the structuring of the top electrodes, the parasitic current paths aside the device stack are eliminated. Parasitic paths within the device stack are actively circumvented by their destruction by an initial reset sweep instead of an electroforming step. The newly developed ReRAM concept exhibits low switching voltages, a non-linear characteristic, and a memory window greater than 10.

Vorwort

In den letzten Jahrzehnten erhöhte sich durch die Verbreitung von Computer- und Multimediaanwendungen in der Konsumelektronik der Bedarf an immer schnelleren, dichteren nichtflüchtigen Speicher. FLASH Speicher sind momentan der Standard für nichtflüchtige Speicher in der komplementären Metall-Oxid-Halbleiter-Technologie. Aktuelle Forschungen beschäftigen sich bereits mit neuen Speicherkonzepten, wie z.B. dem wahlzugriffsfreien Resistiven Speicher (ReRAM), welcher ein hohes Potenzial aufweist, den FLASH Speicher in Zukunft zu ersetzen. ReRAM basiert auf der Änderung des elektrischen Widerstands durch elektrische Stimulation. ReRAM besteht typisch aus dem zu schaltenden Chalkogenid, welches innerhalb zweier metallisch leitender Elektroden angeordnet ist. ReRAM, der im Speziellem auf Übergangsmetalloxiden (TMO) basiert, benötigt im Allgemeinen einen Elektroformierschritt, um das resistive Schalten zu ermöglichen. Dieses Elektroformieren stellt in Bezug auf für die Integration fertig einsetzbarer Speicherbausteine ein deutliches Hindernis dar. Ziel dieser Arbeit ist aufzuklären, ob elektroformierfreier ReRAM durch kontrolliertes Design der Defekte in der TMO Schicht möglich ist. Für die Studien wurde TiO_2 eingesetzt, welches in Bezug auf resistives Schalten intensiv erforscht wurde. Dabei spielt die Existenz von sauerstoffdefizitären, elektrisch leitfähigen Magnéli-Phasen in lokalen Bereichen der TiO_2 Schichten eine wichtige Rolle. Für gestapelte ReRAM Speicherarchitekturen wird darüberhinaus eine Methode verlangt, welche präzise, defekt- und schattenfreie und 3D konforme Deposition der funktionellen Schicht ermöglicht. Solche Anforderungen erfüllt die Atomlagenabscheidung (ALD).

Für die Integration von TiO_2 wurde ein ALD Prozess entwickelt, der die geforderten Materialeigenschaften liefert. ALD Prozessparameter wurden gefunden, um amorphe und kristalline TiO_2 Dünnschichten abzuscheiden. Untersuchungen der Kristallisation von TiO_2 zeigten, dass die Kristallisationskinetik erlaubt, die Kontrolle der Phasenzusammensetzung durch die Wachstumstemperatur, die Schichtdicke und die Prozesszeit zu erklären. Abgeschiedene kristalline Dünnschichten enthielten mitunter die Korundphase Ti_2O_3, deren Präsenz eindeutig Magnéli-Phasen indiziert. TiO_2 von amorphem und kristallinem Zustand wurden in ReRAM als Nanokreuzungspunkte integriert, um deren elektrisches Schaltverhalten systematisch zu untersuchen. Der Vergleich von Transport-, Elektroformier-, und den resisitiven Schalteigenschaften zeigte eindeutig, dass Magnéli-Phasen enthaltende kristalline TiO_2 Dünnschichten für das resistive Schalten zu bevorzugen sind. Kristallines TiO_2 zeichnete sich durch weiches Elektroformieren bei niedrigen Spannungen aus, die im Bereich der Einschaltspannungen der nachfolgenden Schalthysteresen lagen. Im Gegensatz dazu, zeigten amorphe TiO_2 Schichten ein abruptes Elektroformieren mit erhöhten Spannungen, was ein stark linearen Einschalt-Zustand unmittelbar nach dem Elektroformierschritt zur Folge hatte.

Die gewonnen Erkenntnisse über die Korrelation der elektrischen Transport-, Schalt-, und Materialeigenschaften konnten in ein vielversprechendes, neuartiges, elektroformierfreies TiO_2 ReRAM Konzept umgesetzt werden. Dieses Konzept beinhaltet die Eliminierung von parasitären Leitpfaden, welche auf die elektrisch gut leitenden Phasen in kristallinen TiO_2 Filmen zurückzuführen sind. Parasitäre Strompfade durch das Material außerhalb des Nanokreuzungspunktes konnten durch ein geändertes Zellendesign eliminiert werden. Parasitäre Strompfade innerhalb der Zellen konnten durch initiales Ausschalten unterbrochen werden. Die vorgeschlagene ReRAM Struktur auf der Basis sauerstoffdefizitärer TiO_2-Schichten zeichnet sich durch geringe Schaltspannungen, nichtlineare Charakteristik und Widerstandsverhältnissen größer als 10 aus.

Acknowledgment

I would like firstly thank Prof. Dr. Rainer Waser for giving me the opportunity to participate in the interesting field of non-volatile memory investigation. Furthermore, I would like to thank Prof. Dr. Michael Heuken to be my co-examiner.
Special thanks to my supervisor Dr. Susanne Hoffmann-Eifert for the support over the years, remarkable help, and a lot of fruitful discussions. I thank Nabeel Aslam, my brother-in-office for the great time together and endless hours of fun while the nightshifts and in the weekends. I would like to thank Florian Lentz and Nabeel Aslam for their personal engagement to develop new lithography processes to ensure the success of this work. I owe René Borowski thanks for his support in the clean room and finishing samples just in time. I thank Hannes Mähne at the Namlab GmbH for the Raman measurements and Valentino Longo at the TU Eindhoven for the conducted ellipsometry experiments. For the LC-AFM and XPS investigations I thank Christian Rodenbücher and Prof. Kristof Szot. I also want to express my gratitude to Manfred Gebauer for the technical introduction into the ALD reactors. For the discussions on transport theory I thank Dr. Stephan Menzel and Dr. Paul Meuffel. Marcel Gerst, Friedrich Jochen, and Stephan Masberg should not be forgotten for their maintenance of the ALD reactors and help to recover the deep temperature cryostat.
I also would like to express my gratitude Dr. Christoph Hermes, Bernd Rösgen, Dr. Felix Gunkel, Michael Paßens, Max Mennicken, and all others for the nice time and atmosphere at the PGI-7 at the Research Center Jülich.
I also would like to thank my family for their support over the years during my studies. Special thanks to my friends, here to mention especially Guido Rüdelstein and Thomas Heysel who encouraged me to continue my work!

CONTENTS

LIST OF FIGURES

CHAPTER

ONE

INTRODUCTION

Since the revolution of the computer industry in the beginning of the 1980's, personal computer were the first time affordable for most people. With the usage of personal computers the consumers discovered that not only word and data processing is possible, also a variety of other applications like communication over networks, graphic and audio processing and any other kind of digital processing were available the first time at home. The computer industry experienced its self-reinvention: The more computer and computer applications appeared, the more the need for better and faster computer increased. This self-reinvention spawn mobile applications like FLASH cards for digital cameras, USB-sticks, mp3-players, handhelds, smart phones, and tablet computers which appeared in the last two decades. All these appliances need a reliable, cheap, and non-volatile memory. Hard disk drives are not appropriate because of their weight, their power consumption, and the slow write and read access. At the moment FLASH-EEPROM memory posses a solution which is based on complementary metal oxide semiconductor (CMOS) technology like dynamic random access memory (DRAM) and microprocessors. In personal computers this objective is already achieved applying FLASH in the solid state disk (SSD) enabling fast access and acceptable endurance. But professional market applications like server-rooms require non-volatile memory which fulfills write access at the same time scale of read access to bridge the gap between fast volatile memory and slow hard disk storage. This storage class memory (SCM) should combine the advantages from solid state memory, i.e. high performance and robustness, and benefits from low cost production of archival hard disks [1].
In any case, the demand for more and faster memory increases rapidly. The cost of memory scales with the chip size, and as result the 'device per chip' density has to be increased continuously to ensure constant cost or cost below. In the late 1960's, the semiconductor industry already discovered Moore's law that predicts the doubling of the components on a chip every two years [2]. But the prediction will fail, because continuously down-scaling will finally cause the physical failure of CMOS components.
Figure 1.1 shows the concepts which are actually followed and discussed to overcome physical limits of Moore‘s law. To extend the density of components in standard CMOS scaling, func-

tions are being expanded by vertical transistors, for example. The expansion of Moore's law is called 'More Moore'. Besides 'More Moore', new architectures and data processing concepts are parallely developed. These so-called 'Beyond-CMOS' elements may allow to overcome binary data operations or enable further down-scaling. Beside 'Beyond CMOS' elements, the heterogeneous integration of 'More-than-Moore' (MtM) extends the functionality of standard CMOS. In the last years MtM memory concepts emerged in research and some of them are planned to replace FLASH and maybe DRAM in production in 2018 [3]. The ITRS road map lists the Phase Change RAM (PCRAM), and the Spin Transfer Torque Magneto-static RAM (SST-RAM) already as prototypical memories, followed by the Redox Memory, the Mott Memory, the ferroelectric resistive random access memory (FeReRAM), and the the ferroelectric field effect transistor (FeFET) as newly from research emerged. Among these, the PCRAM and the Redox Memory belong to the class of the Resistive RAM (ReRAM). From all newly emerged memory concepts, the redox-based ReRAM has drawn a lot of attention, because the fast development in research reveals excellent scalability, endurance, multi level capability, and low fabrication cost. [4, 5, 6].

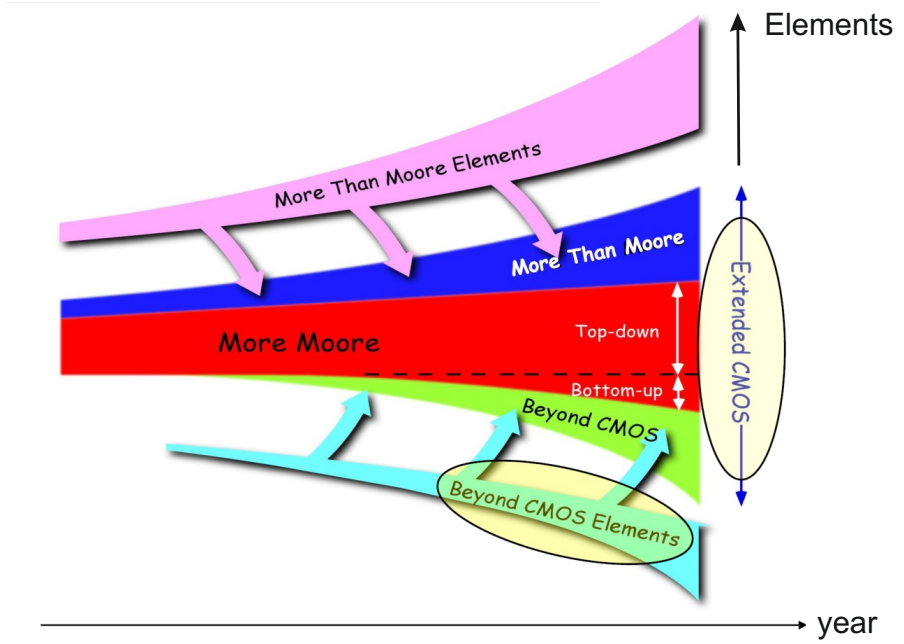

Figure 1.1: Expansion of Moore's law by heterogeneous integration of new functionalities (More than Moore) and replacement of standard CMOS elements by 'Beyond CMOS' elements. Reprinted with permission [3].

1.1 Resistive Switching Random Access Memory

Resistive Switching Random Access Memories (ReRAM) are very simple passive, two-terminal devices which basically consist of a functional layer sandwiched between two metallic conducting electrodes or molecules attached to metallic electrodes. The resistance state of such a layer stack can be switched by applying either an unipolar or a bipolar voltage operation. First reports on resistive switching phenomena in transition metal oxides (TMO) [7, 8, 9] and higher chalcogenides, for example telluric alloys [10, 11] were already published in the 1960s. The research continued until the early 1980s, but at this time such memories were not able to concur with FLASH memory due to its compatibility to standard CMOS technology. In the late 1990s research on resistive switches was rediscovered on perovskites like $Pr_{1-x}Ca_xMnO_3$ (PCMO) [12], silver in sulfides and arsenides [13], titanates, and zirconates [14]. Finally, industry's interest was drawn back to resistive switches and reinvestigation on binary oxides like TiO_2 started [15, 16]. In the following years a large body on resistive switching literature grew on a variety of simple binary and more complex chalcogenides with different type of metallic electrodes. Figure 1.2 shows a very important scheme of Waser and co-workers who classified emerging types of resistive switches by the underlying physical effect, the material class, and the polarity of the voltage operation. The assessed MtM memories which are potential for the integration onto the CMOS platform are highlighted. When the simple stack of a resistive switch is considered, the physical effects can be divided into chalcogenide related and electrode related effects. Electrostatic and electronic effects, such as trapping of charge carriers into interface states at the metal/semiconductor oxide interface which cause a modulation of the Schottky barrier [17] belong to the electrode dominated effects. [1] Another electrode dominated memory system are solid electrolytes which show the ability to dissolve their electrodes. This is called Electrochemical Metalization Mechanism (ECM) [20]. Turning from electrode dominated to chalcogenide related phenomena, there exist four types of physical origin for resistive switching. One physical effect is the phase change of higher chalcogenides (telluride alloys), where unipolar electrical stimulus causes crystallization and reamorphization [21, 22]. The contrast in resistance is due to the change in the material order. The switching in oxides is attributed to the thermochemical mechanism (TCM) and the valence change mechanism (VCM) with unipolar and bipolar operation, respectively. The redox-related memories effects, TCM, ECM, and VCM will be further considered, because they are most promising candidates for MtM memory elements (Redox Memory) [3].

[1] Other electronic effects have to be considered for this classification, such as correlated electron systems in $SmNiO_3$ [18] and AM_4X_8 (A = Ga, Ge; M = V,Nb,Ta; X = S,Se) [19] which exhibit insulator-metal-transitions (Mott memory). But these are not attributed to the function of the electrode in the sense of a resistive switch, and therefore are excluded from further discussion.

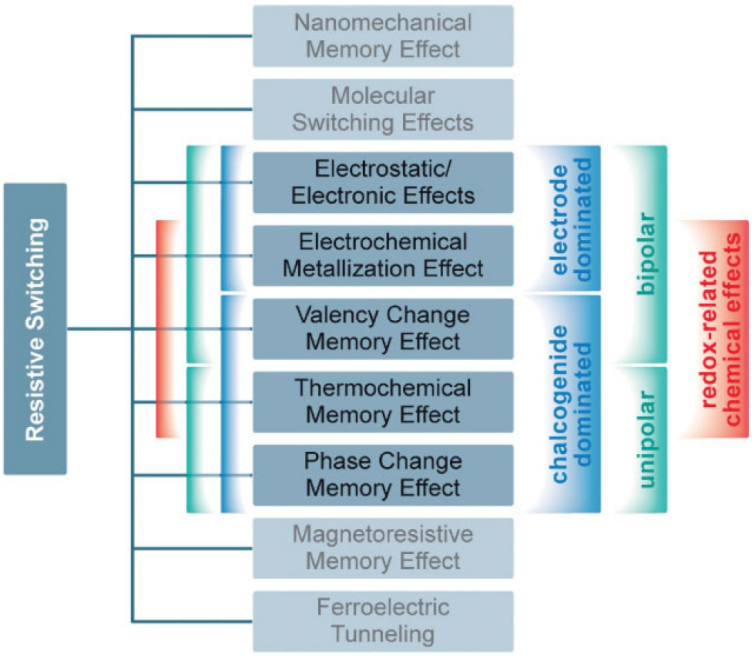

Figure 1.2: Resistive switching effects classified by their physical principle, their material, and their switching polarity. Reprinted with permission by the author [4].

1.1.1 Basic Principles of Redox-Related ReRAM

All redox-related switches have in common that the pristine functional layer or a stack of an oxide layer and an active electrode have to be electroformed by application of a voltage stimulus. Electroforming is a process which degrades the device resistance state to a low resistance state (LRS) or a high resistance state (HRS). This enables reversible resistive switching between high resistance state(s) and low resistance state(s).

1.1.1.1 Thermochemical Mechanism

The thermochemical switching relies on the material change within the functional layer without involvement of any electrode. For this type of mechanism all oxide and inert electrode materials can be taken into account, but this does not mean that each inert electrode/oxide stack is a TCM resistive memory. Here, the electroforming and the SET process to the LRS are found to be initiated by the dielectric breakdown of the oxide and subsequent Joule's heating creating a filamentary conducting path between the two metallic electrodes. The reason for the change in the resistance within the conducting filament is reduction of the oxide within the filament which creates better conducting suboxide phases or if the oxygen deficiency is high enough, metallic

phases. This process depends strongly on the oxide and its thermodynamically properties to establish new phases or metallic parts. One prominent material for the TCM resistive switching is NiO [23]. In NiO based metal insulator metal (MIM) structures the stoichiometric oxide is thermochemically reduced to impure metallic Ni while the forming and SET process. The RESET process is carried out unipolar, but with lower voltage as compared to the SET process.

1.1.1.2 Electrochemical Metalization Mechanism

Resistive switches which undergo electrochemical metalization have an electrochemically active electrode, a chalcogenide which acts as a solid electrolyte, and an inert counter electrode. As illustrated in figure 1.3 while the forming or SET process, the active electrode is partly anodically dissolved at the interface and electrodeposited as metallic dendrites at the inert counter electrode by applying a positive voltage sweep. The SET process is completed if one growing dendrite finger connects to the active electrode. The RESET process needs opposite polarity to disrupt the metallic filament. Here the metal is dissolved again in the solid electrolyte and accumulates at the reactive electrode.

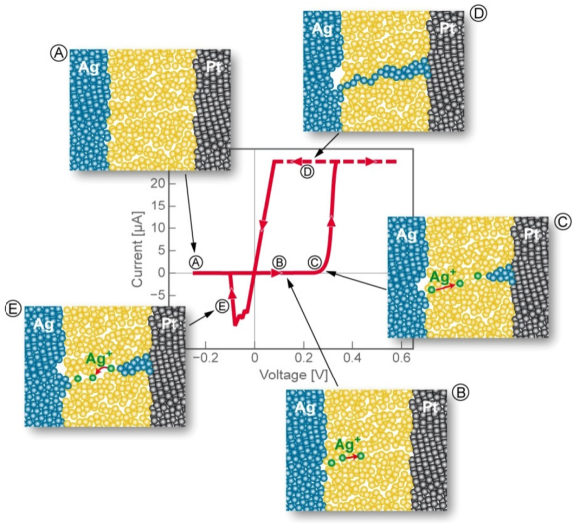

Figure 1.3: Illustration of the Electrochemical Metallization Mechanism. The active electrode is dissolved by the application of a positive voltage and filamentary electrodeposited in Ⓑ and Ⓒ. The ECM cell is set to ON if a metallic filament connected to the counter electrode. Reverse polarity leads to the OFF state by the rupture and reverse cation migration. Reprinted with permission of the authors [20].

1.1.1.3 Valence Change Mechanism

The valence change mechanism (VCM) is primarily attributed to internal changes of the transition metal oxide in between the electrodes. These changes are mainly related to intrinsic defects. Interstitials do not play a major role for resistive switching in VCM type systems, but possible defects are related to the corresponding sublattice [4]. Cations as related defects do usually exhibit low mobilities at temperatures where VCM type resistive switching takes place, but anionic defect motion of oxygen vacancies shows mobilities high enough under the influence of a electric field at moderate temperatures. Because of the fact, that oxygen vacancies are electrically charged defects, the valence change mechanism operates bipolar, as shown for example in many systems like HfO_2 [24, 25], TiO_2[16, 26, 27], doped $SrTiO_3$ [28], and PCMO [17]. The attraction and repulsion of oxygen vacancies lead to the change of their concentration near to electrode site dependent on the polarity at high electric field strength. This may result in the modulation of the Schottky barrier by the depletion and enrichment of oxygen vacancies. As a consequence the electronic conduction at low electric field strength is altered and different resistance states can be read out. Filamentary VCM switching was observed for example in STO [28], but also area dependent switching in PCMO. Both mechanism may coexist in one system. This was demonstrated by Münstermann et al. for STO [29]. As depicted in figure 1.4 varying the switching voltage above a certain threshold causes a change in switching behavior. The counter-8-wise hysteresis is related to filamentary switching and 8-wise hysteresis to homogeneous switching. It has to be stated, that the resistive switching is dominated by a filament or the active area.

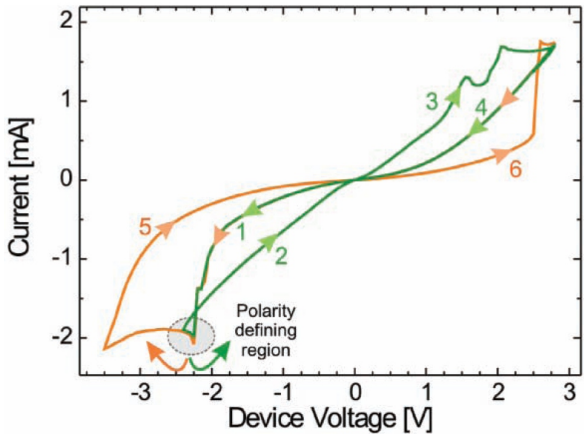

Figure 1.4: Coexistence of filamentary and homogeneous resistive switching in STO. The green hysteresis curve 1-2-3-4-1 represents filamentary switching, the orange hysteresis curve 1-5-6-4-1 is related to homogeneous switching. Reprinted with permission of the authors [29].

1.2 Integration of Atomic Layer Deposited Oxide Layers into ReRAM

The progressive down-scaling has increased industry's interest in modern deposition techniques that allow defect-free, shadow free, and three dimensional coverage of any kind of three-dimensional topography based on standard CMOS technology, bottom up devices, 'More Moore' devices, and future MtM devices [3]. The most prominent method which can provide these criteria is the Atomic Layer Deposition (ALD). ALD facilitates excellent thickness control, 100 % step coverage on any geometry, low deviation (< 2%) with respect to thickness on large areas, and deposition temperatures below 400 °C. ALD is already established in any kind of application, DRAM, high-k dielectrics, metal gates, and contact metallization [3]. Therefore, the investigation of atomic layer deposited functional layers concerning resitive switching properties is of tremendous importance for the progress of ReRAM development.

1.2.1 Nano Cross-point Arrays

To produce non-volatile memory accessible at a low price, a high integration density has to be targeted at a low number of integration steps. The highest density can be achieved using cross-point arrays which need only $4F^2$ of the minimum feature size F for each memory cell in a single layer. Each device in these M x N arrays can be peripherally selected by M+N select transistors. Stacking such memory arrays will only require repetition of the same process steps [30]. The advantage of such a memory is that the number of select transistors scales only with the number of stacks and not with total number of memory cells as depicted schematically in figure 1.5. Such an approach can be realized by nano-imprint lithography or by extreme UV-lithography. Both processes need a planarization step by dry etching or chemical metal polishing after one memory stack is finalized. Such a planarization needs dense, and defect-free coverage with precise thickness of the metallic conducting word and bit lines by ALD. Otherwise uncontrolled, irregular morphology will cause difference in effective MIM device thickness and as consequence high scatter in device properties.

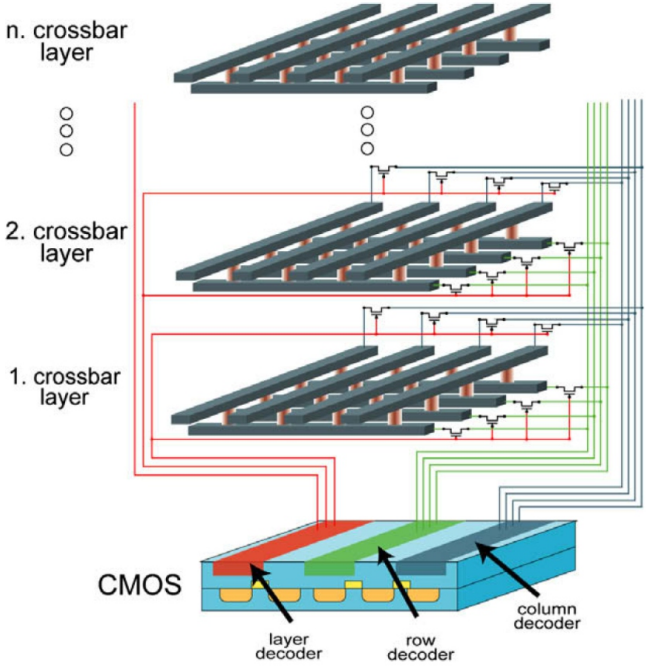

Figure 1.5: Schematic view of stacked ReRAM in a cross point array. Each level needs only single decoding of each stack. Reprinted with permission of the author [30].

1.2.2 Three-dimensional and Vertical Devices

Simple stacking of devices is one approach to achieve high memory density. Instead of crossing metallic conducting lines which have to be addressed at the memory architecture's periphery, vertical electrodes like vias can be used to increase memory density further. This posses a new challenge for the integration of ReRAM as a vertical memory. In figure 1.6(a) the schematic drawing of a vertical ReRAM testified by Samsung is shown [31]. Vertical electrodes are crossing layer by layer stacked planar electrode line stripes which are separated vertically by highly insulating material and horizontally by the functional switching layer within an insulating matrix. In this geometry the active cell area is limited to the area where the horizontal electrodes touches the circumference of the active oxide layer. This means, that a significant number of ReRAM cells can be fabricated in a certain memory layer for each vertical electrode. It depends on the number of surrounding electrodes in the horizontal layer and reasonably the memory density can be potentially further increased. The deposition of the oxide layer and the metallic conducting vertical electrode on the sidewall of a pinhole is challenging. This challenge can be solved by utilizing ALD as demonstrated by multilayer deposition of AlO_{2-x} and TiO_{2-x} in figure

1.7. In this approach the highest field drop is at the minimum distance of the core electrode and the horizontal electrode. For this geometry, the cell size is defined by the width and thickness of the horizontal metal lines.
Similarly, the control of the functional area was demonstrated in a three-dimensional device in a cavity depicted in figure 1.6(b) [25]. A small pillar was anisotropically etched down through CVD deposited SiO_2 to reduce the contact area to a Pt electrode beneath. As functional layer HfO_2 was conformally deposited by ALD, followed by ALD grown TiN.

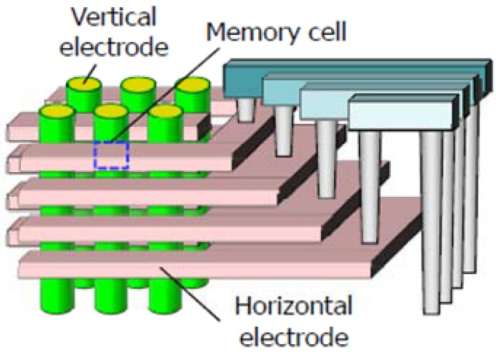

(a)

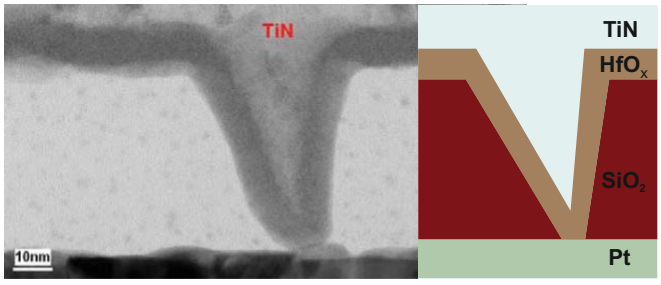

(b)

Figure 1.6: (a) Scheme of Vertical ReRAM. The vertical functional oxide layer is sandwiched between vertical electrodes and horizontal electrodes each level. (b) Three-dimensional ReRAM device in a cavity. On the left a HRTEM image is shown, on the right the corresponding scheme. Conformal deposition of HfO_2 and TiN is realized by ALD. Reprinted with permission of the authors [31, 25].

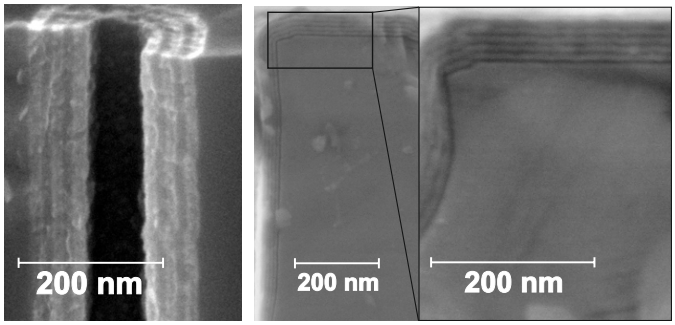

(a) (b)

Figure 1.7: Cross-sectional SEM images of TiO_{2-x}|AlO_x multilayers. (a) Broken test structure before HF dip. (b) After HF dip: Only 5 nm TiO_2 layers left at the fraction.

1.3 Review on Resistive Switching of TiO_2

In recent years researchers interest grew to understand the resistive switching phenomena of TiO_2 based on the motion of oxygen vacancies. The key to understand the mechanism of resistive switching of TiO_2 is to elucidate the microscopic processes while the electroforming and the resistive switching itself. In this context, the research on electroforming and resistive switching revealed that a clear distinction has to be drawn between the electrode symmetry, material properties itself, and the kind of the electroforming and resistive switching. In TiO_2 different switching modes were reported. Unipolar resistive switching (URS)[32, 33], bipolar resistive switching (BRS) [16, 27], and the coexistence of both switching modes [32] were found. As shown in figure 1.8 URS often needs very high currents above 30 mA for the RESET operation [32], whereas BRS was demonstrated to enable switching currents widely below 1 mA in nano cross-point devices [16, 34]. Reasonably, the research on TiO_2 resistive switching is focused on the bipolar operation due to lower power consumption.

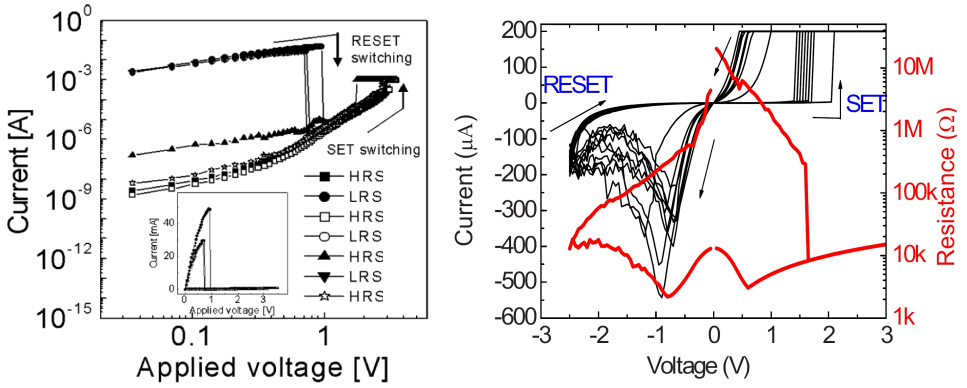

(a) (b)

Figure 1.8: Examples for resistive switching of TiO_2. (a) Unipolar switching of a Si|SiO_2 |ZrO_2|Pt|TiO_2(27 nm) |Pt stack. (b) Bipolar switching of atomic layer deposited TiO_2 in a nano cross-point device Si|SiO_2 |Ti |Pt |TiO_2(8 nm)|Ti |Pt. Reprinted with permission of the authors [35, 34].

1.3.1 Electroforming of TiO_2

The electroforming procedure essentially influences the resistive switching of TiO_2. Jeong et. al have demonstrated on a Si|SiO_2|ZrO_2|Pt(27nm)|TiO_2 |Pt stack, that a different current compliance while voltage driven forming lead to different resistive switching modes [32]. The application of current compliances $\geq$ 1 mA enables URS, whereas current compliances $\leq$ 100 μA activate BRS. BRS is more desirable and as a consequence, the investigation on the forming behavior on such a symmetric memory cell stack Si|SiO_2|ZrO_2|Pt|TiO_2|Pt was thoroughly conducted to achieve BRS. Two kind of forming procedures were performed: Voltage driven electroforming with a current compliance and current driven electroforming with an upper current limit for the better control of the current overshoot. This is of importance, otherwise electroforming may result in URS. It was demonstrated by the authors, that by both polarities BRS can be only activated if a second electroforming step with opposite polarity of the preceding forming was carried out. But, the second forming step could be also successfully avoided under UHV condition [36]. The authors conclude, that elementary oxygen may dissociates and oxidize the oxygen deficient TiO_{2-x} by an annihilation reaction at the top electrode interface if a positive voltage is applied. Therefore a second electroforming step with opposite (negative) polarity is needed, to attract further oxygen vacancies which are known to be created in TiO_2 while electroforming [16, 37, 38]. The attracted oxygen vacancies penetrate the very first layer next to the Pt electrode, and locally lower the Schottky barrier of the TiO_2|Pt interface [36]. This gained knowledge was put into application of asymmetric electrodes which allow to overcome the Schottky barrier and to enrich oxygen vacancies in TiO_2 dependent on the electrode material. In this way, Nauenheim et al. demonstrated single step forming in a Si|SiO_2|Ti|Pt|TiO_2|Ti|Pt to enable BRS. This enables lower forming voltages with the Schottky diode in forward direction as depicted in figure 1.9. Similarly, Yang et al. reported on the swap of ohmic and Schottky interface by changing the stacking order of a reduced and an oxidized TiO_2 thin film [16]. In this experiment, the reduced interface site was always ohmic and showed no rectifying behavior.

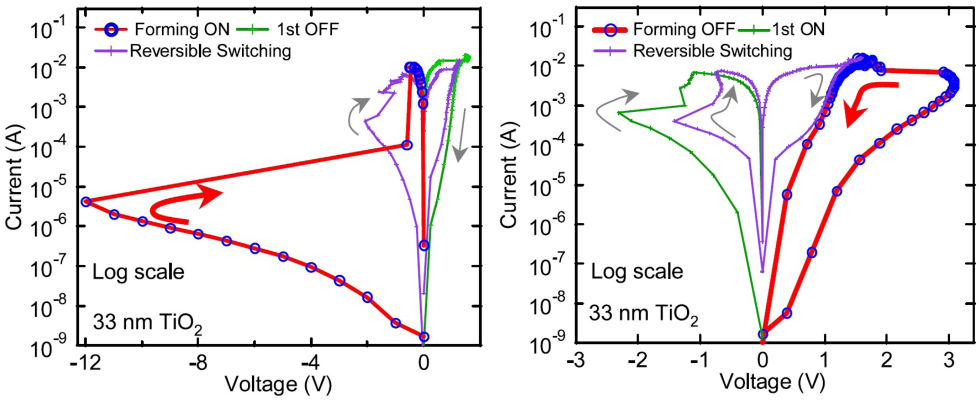

(a) (b)

Figure 1.9: Red curves demonstrate voltage driven electroforming of asymmetric TiO_2 resistive switching cells with negative and positive polarity in (a) and (b), respectrively. Lower forming voltages were achieve with positive bias applied on the top electrode. Reprinted with permission of the authors [37].

1.3.2 Identification of the Switching Site in TiO_2 ReRAM

Pristine TiO_2 devices with Schottky-like behavior show area dependent conductance. But only from this point of view, the forming experiments do not allow to conclude whether the BRS switching is area-related (8-wise) or filamentary (counter-8-wise). Thermal heating and electroreduction are known to lead to formation of elementary oxygen. In the case of evolution of molecular oxygen, it is questionable if by electroforming the TiO_2 will show morphological changes within the MIM device. Therefore, topographic investigations were carried out by several groups. Jeong et al. employed atomic force microscopy (AFM) on a TiO_2|Pt stack [36]. Their analysis showed an eruptive feature on the TiO_2 surface which correlates with an increased conductance parallely measured by conductive AFM (c-AFM). Such an eruptive feature on a cross-point device is reproduced in figure 1.10.

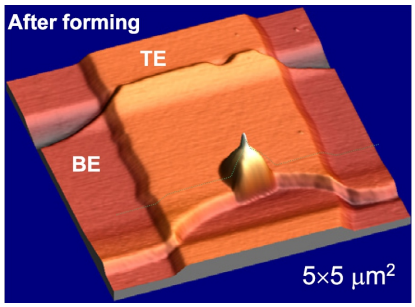

Figure 1.10: Eruptive feature after electroforming of a Si|SiO_2|Ti|Pt|TiO_2|Pt cross-point device. Reprinted with permission of the author [37].

To clarify what causes this eruptive feature, thoroughly polarity dependent investigation on a micro-scaled Si|SiO_2|Ti|Pt|TiO_2|Pt stack were done. The analysis showed that electroforming with positive polarity leads to the evolution of bubbles beneath the Pt top electrode [37]. The bubbles disappeared if the positive bias is no longer applied. Negative bias led to less bubbles which do not vanished after releasing the voltage. The same results were found under UHV condition. From the electromigration experiments the appearance of oxygen ions O^{2-} were concluded. Such species are attracted by positive voltage. As a corollary, molecular oxygen is built at the top easily leaving the stack but remains at the bottom electrode layer. After delamination of the top electrodes [39], topographic analysis by AFM revealed that positive electroforming does not essentially change the TiO_2 thin film. But devices which were formed with reverse Schottky polarity exhibit a crater [37]. In fact, the TiO_2 was taken away by delamination technique. In this regard, local deformation by evolving elementary oxygen decreases adhesion between the TiO_2 thin film layer and the subjacent bottom electrode [1]. The deformation spots were found to be electrically higher conducting than the surrounding [39]. This supports the hypothesis that the switching is filamentary type in this device configuration under given electroforming condition. The higher electrical conductance of such a spot may be attributed to oxygen vacancies ($V_O^{\bullet\bullet}$) in TiO_2 which are left after releasing oxygen O_2 from the material. Several approaches were made to highlight, what exactly causes the highly conducting filament in TiO_2. Strachan et al. applied near edge extended x-ray absorption fine structure spectroscopy (NEXAFS) to resolve spatially the structure of electroformed microdevices. After delamination of the top electrode, photoemission electron microscopy (PEEM) showed no crater-like destruction was left on a Si|SiO_2|Ti|Pt|TiO_2|Pt stack after positive electroforming. Furthermore, oxygen deficienct TiO_2 was detected in this region according to NEXAFS reference spectra. Near to the reduced regime, the anatase phase was found in addition. The authors argue that the electrically well-conducting spot enables Joule's heating which induces thermally-assisted crystallization into the anatase phase. Among the crystalline suboxides of stochiometric titanium oxide the Magnéli-phases are known to be better conductive as compared to the insulating stochiometric titanium oxide. Kwon et al. prepared from Pt|TiO_2|Pt plug devices lamellae as shown in figure

[1] It has to be mentioned that such a local deformation was not found in nano cross-point devices.

1.11 by focused ion beam (FIB) cutting for high resolution transmission electron microscopy (HRTEM). The right inset shows the HRTEM picture of the lamella cut from the blown off adjacent region. Within the lamella a conical shaped pillar was found which connected the top and bottom electrode. Fourier analysis revealed that the corresponding structure of this pillar is the Magnéli-phase with the stochiometry Ti_4O_7. It is also reported that within the lamella more than one Ti_4O_7 Magnéli-pillar was found, but not every pillar connected the bottom and top electrode. In addition, the authors carried out FIB cutting from a HRS state device. The analysis revealed also Magnéli-pillars, but they do not connect the electrodes. Non-destructive scanning transmission x-ray microscopy (STXM) confirmed the Ti_4O_7 Magnéli -phase on a functioning nano-cross-point device, fabricated on a Si_3N_4 window. As shown in figure 1.12 the highly conducting filament was spatially-resolved identified with the Magnéli -phase Ti_4O_7 [40].

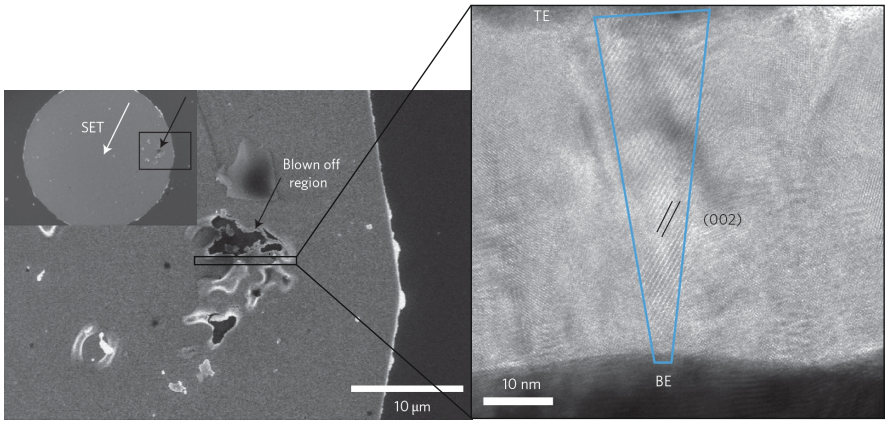

Figure 1.11: SEM picture of a plug Pt|TiO_2|Pt after electroforming. On the right the HRTEM image cutted from the neighbouring MIM structure next to the crater region is shown. Reprinted with permission from the authors [41].

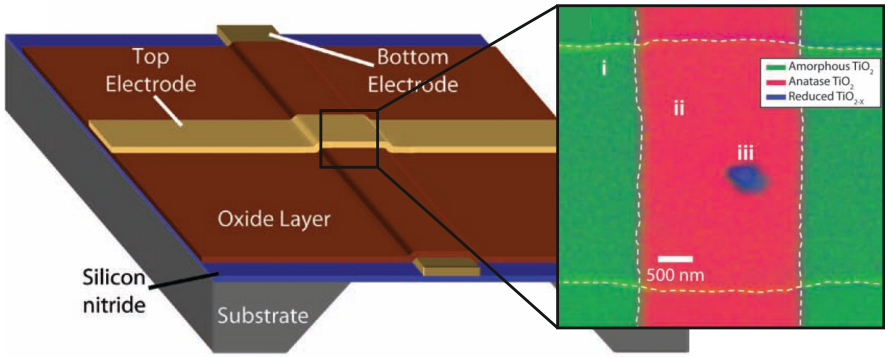

Figure 1.12: On the left side a schematic drawing of a Si|SiO_2|Cr|Pt|TiO_2|Pt cross-point device on a Si_3N_4 TEM window is drawn. The corresponding TEM image is shown on the right. Reprinted with permission of the author [37].

1.3.3 Mechanism of resistive switching in TiO_2

Among the numerous publications on the bipolar resistive switching of TiO_2 several models were proposed to explain the resistive switching mechanism of TiO_2. From the experimental findings it is obvious that resistive switching of TiO_2 is related to the formation of a filament where switching takes place. All major models include the migration of oxygen vacancies. But how the oxygen vacancies contribute to the resistive switching is still a hot topic and may depend on the exact device stack. Mostly, devices with inert Pt electrodes are investigated [41, 42, 43] and all models focus on the filament and/or the interface between the Pt electrode and the filament. Early attempts try to explain the resistive switching by the modulation of the Schottky barrier heigth at one active interface [16, 36] which is reasonable because of the bipolar operation. This model was refined by Jeong et al. in a way that the oxygen vacancies are pushed and repelled from the Helmholtz layer between reduced TiO_{2-x} and the Pt electrode [42]. In detail, the model describes the electrochemical annihilation of the oxygen vacancies by oxygen bond to the Pt at the interface site. This results in a change of the oxygen vacancy concentration profile within the Helmholtz layer and its vicinity. As a consequence, the resistive switching phenomenon is ascribed to the modulation of the Schottky barrier by a voltage and/or time variation [42]. It has to be noted that this model underlies the assumption that no oxygen is exchanged with the ambient atmosphere, only extrinsic oxygen from the active Pt surface is taken into account. Later models arised when the Magnéli-phase Ti_4O_7 was possibly identified to be the conducting channel through the stochiometric TiO_2. Hewlett Packard states that the change of the device resistance is due to a modulation of a tunnel gap between the active electrode and the well-conducting Ti_4O_7 channel by electromigrating oxygen vacancies [44]. This allows to model multilevel switching between different resistance states. Their further findings describe the resistive switching is a thermally assisted change of the barrier by

Joule's heating of the filament [43]. Szot et al. have thorougly argued that several facts should not be forgotten because of the found Magnéli-phase Ti_4O_7. On the one hand the transformation of the oxygen vacancies in rutile TiO_2 into the Ti_4O_7 Magnéli structure is from thermodynamically point of view a transient process. The transformation can happen along the homologeous series of the TiO_2 Magnéli-phases [45]. Ti_4O_7 is metallic conductor at room temperature, but all other Magnéli-phases show different semiconducting behavior. This may explain in another way why multiple resistance states can be programmed into TiO_2 devices. On the other hand, the possibility of electroreduction may play an role to achieve different conducting Magnéli-phases besides thermally-assisted reconfiguration of the material under oxygen vacancy flux. Nevertheless, all major models have in common that oxygen anions are involved in TiO_2 resistive switching elements. Therefore, resistive switching in TiO_2 is mainly attributed to the valence change mechanism. Of course, maybe other effects have to be considered. Miao et al. have demonstrated that soft OFF-forming of TiO_2 with very low current compliance does not only enable switching with counter-8-wise operation, but also allows 8-wise operation with a common state. The 8-wise BRS operation was found to be caused by filling deep traps. As a consequence, resistive switching of TiO_2 may not be purely redox-related.

1.4 Scope of this Work

An obstacle for the application of resistive switching of TiO_2 is the electroforming. From industrial point of view electroforming operation needs to be avoided in terms of ready-for-use memory. The preceding summary on bipolar resistive switching of TiO_2 highlighted which material properties are in favor of functioning TiO_2 ReRAM devices. Oygen vacancies play an important role to enable resisitive switching. In addition to the oxygen vacancies, the crystallinity of TiO_2 and its influence on resistive switching are worthwhile to investigate since Magnéli-phases were found to play a major role in the conducting filament. Concerning the integration into future three-dimensional memory arrays, for example vertical ReRAM, this investigation has to be combined with the atomic layer deposition of TiO_2. Therefore this work focuses are subdivided into the development of a suitable atomic layer deposition process and the electrical characterization of TiO_2 ReRAM devices. In detail, the first part will focus on the crystallization of oxygen deficient TiO_2 in a single ALD process step. The influence of the process growth parameters like thickness, temperature, and time are studied in detail to highlight how to achieve most matching properties to resisitively switchable TiO_2. The second part of this work will deal with integration and characterization of TiO_2 with different crystallinity; the amorphous state and crystalline phase. The electrical transport properties of pristine devices will be elucidated with respect to thin film thickness and crystallinity. Especially, regarding forming-free devices the electroforming as well as the resistive switching is performed under the same electrical test condition. In the final step all achieved knowledge will be put into application, and additional change of device fabrication strategy to achieve forming free devices.

CHAPTER

TWO

ANALYTICAL METHODS

This chapter will give a short introduction into the methods for thin film analysis and the electrical characterization of resistive switching devices utilized during this thesis. The thin film analysis methods comprise investigation of the topography, the structural, the chemical, and the optical properties. The resistive switching properties were analyzed by means of DC sweeps and low temperature measurements to reveal their electrical transport characteristics, in addition.

2.1 Thin Film Characterization

The characterization of atomic layer deposition processes typically need several thin film analysis methods to clarify the chemical impurities within the grown films, the growth rate, and the structural and topographic properties. In addition to that, highly resolved imaging is necessary to investigate conformal growth and device structures.

2.1.1 X-ray Photoemission Spectroscopy

The chemical analysis can be carried out by x-ray photoemission spectroscopy (XPS). It is based on the determination of the binding energy by the excitation of core level electrons by x-rays. For that purpose, monochromatic x-rays are irradiated onto a sample surface as depicted in figure 2.1. The energy-rich photons penetrate the bulk material the very first nanometers in depth [46]. On their way through the bulk electrons are ejected from their core levels. Under UHV condition, the transfered energy from the x-ray photons allow the electrons to travel through the bulk material and leave the surface as schematically shown in figure 2.2. The energy of the photons

$$h\nu = E_{\mathrm{b}} + E_{\mathrm{kin}} + W \tag{2.1}$$

equals the sum of the binding energy E_b of the ejected electrons, their kinetic energy E_{kin} after release from the sample, and the apparatus' work function W. Thus, for the determination of the binding energy the kinetic energy of the electrons has to be detected at given apparatus' work function and the photon energy. The detection is carried out by an hemispherical sector analyzer (HSA). The electrons, emitted from the surface are collected and focused by an electron lens system and deflected by the HSA depending on their kinetic energy. For the detection, the electrons are collected by a channeltron or a multichannel detector as a function of the voltage applied on the hemispherical conductors. Each element causes different characteristic peaks depending on the energy. The chemical composition can be derived by the integration of the characteristic peaks and calculation of the partial fraction of the total signal sum. For the estimation of impurity contents usually the material is dry etched by Ar^+ sputtering because surface contaminants contribute to the atomic concentration. Generally, different stoichiometric compositions exhibit distinct binding states of each element. In XPS, such changes can be observed by the chemical shift of the element specific signal peaks. Since sputtering cause severe damage of the material and as a consequence the change of its binding states, angle resolved XPS (ARXPS) is carried out to preserve the binding states within the material. The depth information decreases with increasing angle of electrons ejected from the surface. Reasonably, measurement under different angles allows to qualify the contribution from bulk states to the XPS signal.

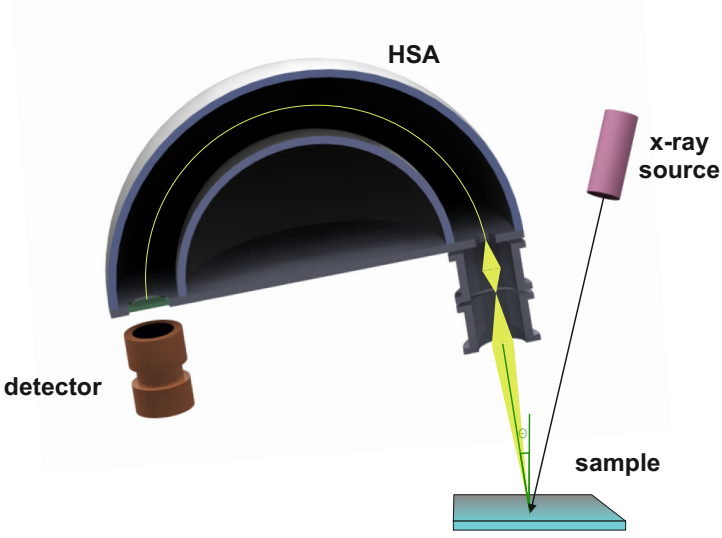

Figure 2.1: Scheme of the working principle of a XPS measurement tool. Energy-rich x-rays are irradiated onto the sample surface under UHV condition. The excited electrons which leave the surface of the sample are collected by the analyzing optics. The electrons are focussed before entering the hemispherical analysator. After passing the hemispherical analysator the electrons are detected depending on their kinetic energy.

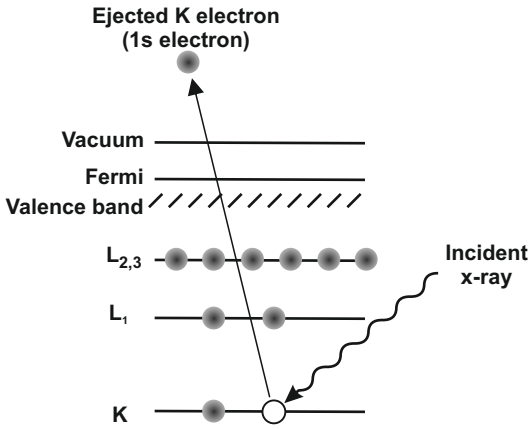

Figure 2.2: Excitation of an electron from the core shell level by the irradiation of a x-ray photon. The amount of transfered energy is high enough to extract the excited electron to the surface of a material above the Fermi level. After [46].

2.1.2 X-ray Fluorescence

XPS is based on the ejection from electrons in the very few nanometers in depth from the surface of a sample. Reasonably, no absolute concentrations overall can be determined. But the detection of elements is not limited to ejection of electrons since the irradiation of x-rays cause fluorescence of x-ray photons of lower energy as depicted in figure 2.3. Thus, an element specific spectrum can be detected energy-dispersive or by an appropriate spectrometer. This is called x-ray fluorescence (XRF) and is a well-established method for tracing elements in matter down to several ppb and below. Reasonably, this allows the quantification of elements in thin films of only a few nanometer. Utilizing classic XRF, the quantification is done similar to XPS by taking the integral number of detected counts from the recorded spectra. To quantify the mass layer density in absolute numbers, a standardization is needed. This is the most precise method. However, if the spectrometer's fundamental parameters, the behavior of the optical apparatus and the sensitivity to a certain elemental line is known, estimation of the concentration without any standardization is possible. This is called fundamental parameter analysis XRF (FPA-XRF). FPA-XRF utilizes the theoretical prediction of the intensity of the fluorescence x-ray spectra from a known chemical composition based on the Sherman equations [47]. If the composition is unknown, it can be backward calculated from a measured spectra. From that, a theoretical intensity profile can be initially calculated and compared to to measured one. From the comparison, the convergence can be taken. If the convergence criteria is fulfilled, the back calculated composition allows an estimation of the absolute concentration. If the convergence values are too high, the assumed composition can be modified until the theoretical intensity profile matches the measured one. Thus, the FPA-XRF is a powerful method to determine the mass

layer density of thin film samples with varying composition. This represents an advantage in the optimization in atomic layer deposition where the composition may change due to incomplete reactions, see chapter 3. Nevertheless, utilizing the FPA-XRF methods needs to be regularly checked by standards to ensure that the physical fundamental parameters do not shift. Giving one example, the aging of the x-ray tube causes already a strong deviation from the estimated fundamental parameters in a XRF system.

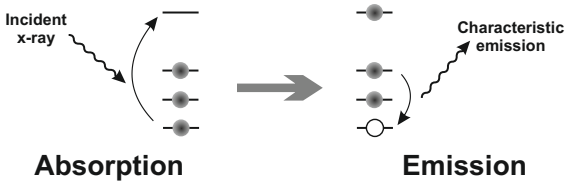

Figure 2.3: Physical principle of x-ray fluorescence. One electron from a lower orbital state of an atom is excited by an incident x-ray photon on the left. One electron of an higher energy level drops down to the lower one free energy level under emission of a characteristic photon.

2.1.3 X-ray Reflectivity

The thin film deposition needs a very precise method to measure the thin film thickness. A very accurate method is the x-ray reflectivity (XRR). It is based on specular reflection of monochromatic x-rays under an incident beam angle of Θ. This is usually done with a Bragg-Brentano optics depicted in figure 2.4(a) which ensures an optimum focused reflection.

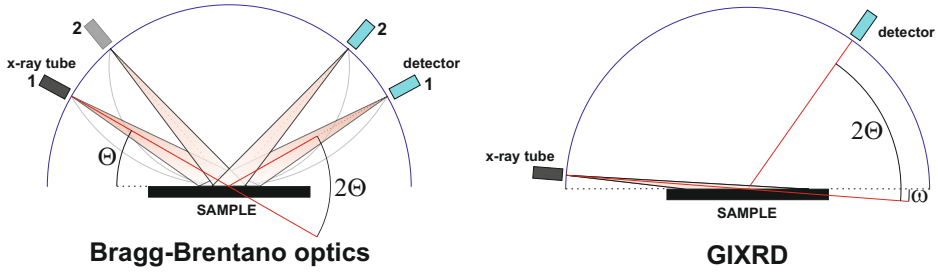

Figure 2.4: Typically goniometer configuration in a x-ray diffractometer. (a) Bragg-Brentano optics utilized for the measurement of the thin film thickness. The x-ray source, the sample stage, and the detector moving simultaneously at the same angular speed. (b) Measurement of x-ray diffraction for polycrystalline thin films under glancing angle. The glancing angle is fixed while the detector moves.

In this configuration the sample focuses the x-rays on the detector with the same radius

as for the incident x-ray source. In detail, the XRR method is based on Snellius' law which describes the propagation of light in matter. Its dispersion δ and absorption β is described by the diffraction index [48].

$$\tilde{n} = 1 - \delta + i\beta \tag{2.2}$$

The reflection phenomena of x-rays of thin films is subdivided into two distinct regimes below and above the critical angle of total reflection. The critical angle Θ_C can be calculated by Snellius' law

$$1 - \delta = \cos\Theta_c \tag{2.3}$$

$$\Theta_c \approx \sqrt{2\delta} \tag{2.4}$$

Below the critical angle, the reflection intensity increases rapidly to its maximum. This is related to the fact that not the full x-ray beam irradiates the sample. Above the critical angle, x-rays can penetrate the thin film and are reflected on the next interface layer drawn as the substrate layer in figure 2.5.

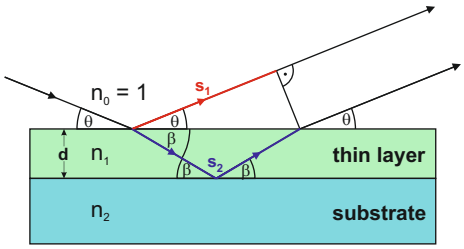

Figure 2.5: Reflection of x-rays on a single thin film layer on a substrate.

The path difference of the x-ray light from the first reflection on the surface of the thin film and the next layer calculates to [49]

$$\Delta s = \tilde{n}_1 \cdot s_2 - s_1 \tag{2.5}$$

$$\Delta s = 2\tilde{n}_1 \frac{d}{\sin\beta} - s_0 \frac{\cos\Theta}{\tan\beta} \tag{2.6}$$

$$\Delta s = 2d\sqrt{\tilde{n}^2 - \cos^2\Theta} = 2d\tilde{N} \tag{2.7}$$

where $\tilde{N}$ is the generalized refractive index as a function of the angle Θ. In the focus point of the detector the two different reflections interfere and reasonably the intensity shows fringes as a function of Θ. In the case of the thin film layer's refractive index $\tilde{n}_1$ is lower than the substrate's refractive index $\tilde{n}_2$, the Bragg's law for constructive interference writes

$$m\lambda = \Delta s = 2d\tilde{N} \tag{2.8}$$

In case of $\tilde{n}_1 > \tilde{n}_2$, in equation 2.8 m needs to be replaced by $m+1$ and π has to be added on the right hand side. For small angle Θ_m equation 2.8 can be approximated to [50]

$$\Theta_m \approx m^2 \frac{\lambda^2}{4d^2} + \Theta_\mathrm{C}^2 \tag{2.9}$$

In this form, Θ_m clearly reveals its dependence on the critical angle which is a function of the dispersion. The dispersion is linked to the density of the thin film layer. This is of importance for the detection limit of a deposited thin film. Does a thin film exhibit similar density and atomic form factors [49], the observation of fringes is quite complicated and XRR does not meet the requirements of precise thin film layer analysis. Nevertheless, the thickness can be derived from the angular distance from $\Theta_{\mathrm{m}+1}$ and Θ_m:

$$d \approx \frac{\lambda}{2} \frac{1}{\sqrt{\Theta_{m+1} - \Theta_C^2} - \sqrt{\Theta_m - \Theta_C^2}} \tag{2.10}$$

For angles $\Theta_m >> \Theta_\mathrm{C}$ the equation can be simplified an rewritten to

$$\Delta\Theta = \frac{\lambda}{2d} \tag{2.11}$$

For that simplification, the fringe to fringe angle is a constant function of the thin film thickness at fixed x-ray wavelength for high angles as demonstrated in figure 2.6. The measurement plot also shows, that the intensity continuously changes by several orders of magnitude. For angles $\Theta > 1.5\Theta_\mathrm{C}$ the specular reflection on a perfect layer without any surface or boundary layer roughness drops in intensity by $I \propto \Theta^{-4}$ [51]. In figure 2.6 the damping of the interference oscillation is pointed out which relates to the influence of the RMS roughness $\left\langle z^2 \right\rangle$ deviating from perfect interface layers. The damping exponentially depends on the RMS roughness and on the quadratic argument of the reflection angle [52].

$$I \propto \exp\left(-16\pi^2 \sin\Theta^2 \frac{\left\langle z^2 \right\rangle}{\lambda} \right) \tag{2.12}$$

Thus, XRR is limited to relatively smooth surfaces with roughnesses up to 5 nm depending on the substrate and material composition [48]. The derived equations 2.10,2.11 are only valid for small angles up to 5 ° [49]. For the determination of very thin films such a simplification is not satisfactory and fitting and simulation of the linked intensity is needed. Besides that, the XRR method has got an absolute lower detection limit for the thickness depending on the thin film materials reported to be about 1 nm with sufficient accuracy [48]. Recently, the NIST [1] reported on the limitations of XRR on even conformally grown HfO_2 layers which reproduce the substrate layers low roughness well [53]. The investigations on such a perfect thin film layer system revealed that the absolute lower limit of thickness measurements by XRR is 0.8 nm. This value even saturates independent if the signal to noise ratio is improved by higher integration time.

[1] National Institute of Standards and Technology

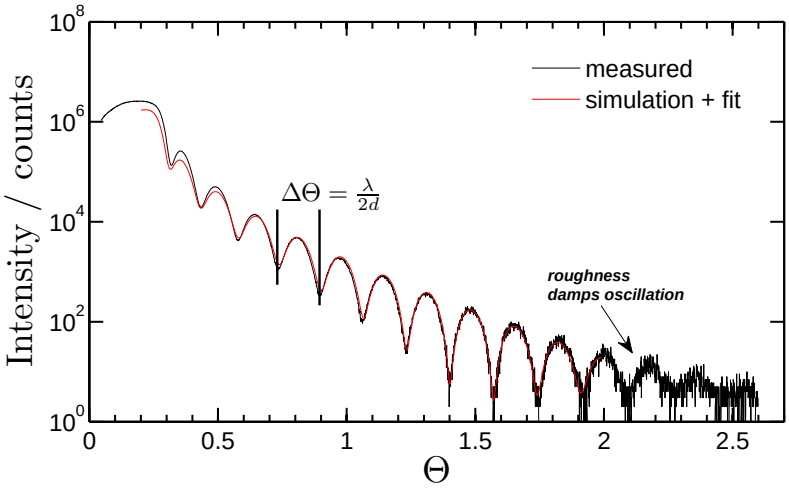

Figure 2.6: Example for the reflection of x-rays on a thin film layer. Several fringes with aquidistant maxima appear.

2.1.4 X-ray Diffraction

X-rays does not only allow to measure the thickness, also structural investigation can be carried out. Bragg discovered the scattering of x-rays creates x-ray diffraction (XRD) pattern from crystalline structures [54]. Hereby, the electromagnetic waves undergo Rayleigh scattering on the cloud charge of the atoms. By this, the x-rays in phase are scattered from each atomic plane of the solid and the reflected x-rays are no longer in phase. Reasonably, interference patterns appear under a specific glancing angle as depicted in figure 2.7. The diffraction peaks can be only observed under a certain angle according to Bragg's law

$$n\lambda = 2d_{\mathrm{h,k,l}} \sin\Theta \tag{2.13}$$

where $d_{\mathrm{h,k,l}}$ is the distance between two adjacent planes in the crystal lattice of given orientation to the normal of the incident x-ray beam indicated by the Miller indices $\{hkl\}$. The distance between the planes depends on the structure of the Bravais lattice of the crystal. That means, the lattice parameter and the type of crystal lattice are the determining parameters. For example, the distance from plane to plane for the cubic lattice is given by

$$d_{\mathrm{h,k,l}} = \frac{a}{\sqrt{h^2 + k^2 + l^2}} \tag{2.14}$$

where a is the lattice parameter. Therefore, the diffraction pattern is a fingerprint of a specific crystal lattice. In addition to that, the scattering from different kind of atoms modulates the intensity of observable diffraction peaks. For that reasons monochromatic x-rays allow to identify the crystal structure of an unknown crystal. In case of thin films, the symmetric Bragg-Brentano

optics enables penetration of x-rays into the substrate. Reasonably, the substrate diffraction intensity dominates the diffraction pattern intensity of the thin film layer since less matter is crossed by the x-ray beam. To increase thin film diffraction intensity, gracing incidence x-ray diffraction (GIXRD) [2] offers a better solution. Instead of symmetric incident and diffracted beam paths, a small fixed incident angle is used as depicted in figure 2.4(b). The incident beam does not penetrate much the substrate and more thin film is crossed by the beam in sum. In this way, more crystallites which fulfill Bragg's law can contribute to the diffraction pattern.

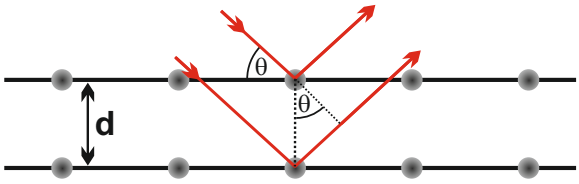

Figure 2.7: Scattering of x-rays on a crystal lattice.

However, very small crystallites decrease the intensity further and result in a bad signal to noise ratio. This makes the identification of different phases in thin films difficult. In such a case, Mierzwa et al. successfully demonstrated the application of Wiener Fourier Filtering (WFF) to recover diffraction peaks from a noisy GIXRD measurement [55]. The detected signal $c(t)$ is the sum of the diffraction signal $s(t)$ and the noise $n(t)$.

$$c(t) = s(t) + n(t) \tag{2.15}$$

The equation writes in Fourier space

$$C(f) = S(f) + N(f) \tag{2.16}$$

where f denotes here the reciprocal measured angle as a frequency. The WFF needs to find an optimized filter function $\Psi(f)$ to remove noise from the rest of the frequency spectra in Fourier space.

$$\tilde{S}(f) = \Phi(f) \cdot C(f) \tag{2.17}$$

which gives an approximation $\tilde{S}(f)$ of the true frequency spectra by least-square fit optimization. The filter function calculates by

$$\Phi(f) = \frac{|S(f)|^2}{|S(f)|^2 + |C(f)|^2} \tag{2.18}$$

$$\Phi(f) \approx \frac{|S(f)|^2}{|C(f)|^2} \tag{2.19}$$

Practically, the fraction of $|S(f)|^2$ from $|C(f)|^2$ can be distinguished in the power spectra plot of $C(f)$. The noise contribution in the power spectra marks the frequency range where the

[2] In literature often gracing incidence diffraction (GID) is used.

least square fit is applied. This can be functionalized for example by a straight line through the noise. This gives a frequency dependent function which can be subtracted from the power spectra $|C(f)|^2$ leading to the power spectra $|S(f)|^2$. Such a procedure needs a definition of an truncation point in Fourier space. The truncation point can be set manually where noise cannot be longer recognized in the power spectra $|C(f)|^2$ similar to the common Fourier filtering procedure. Recorded GIXRD data additionally need to be periodized for WFF, or simply to be background corrected. In this work, background correction was done by a least square fit through data points which do not contribute to any diffraction peak in Fourier space. This additionally allows to compare the absolute diffraction peak intensities values if the x-ray source does not vary much.

2.1.5 High Resolution Transmission Electron Microscopy

The structural investigation of solid state matter is not limited only to x-rays. Transmission electron microscopy (TEM) uses electrons to reveal the structural properties. TEM is a direct imaging method which also enables observation of diffraction patterns similar to XRD due to the wave-particle duality. In a TEM electrons are accelerated by voltages ranging from several 10 kV to 400 kV to pass through a very thin specimen of several 100 nm down to 10 nm [56]. While passing the specimen, the electrons undergo Rutherford scattering. This characteristic scattering is utilized in TEM: Electrons which directly pass through the specimen are separated from scattered electrons as depicted on the right of figure 2.8. This results in a direct contrast image which can be magnified by an electron lens system. The contrast depends on the atomic number of the elements and the thickness of the sample. Hence, also direct imaging of amorphous structures is possible. To observe diffraction patterns from scattering on crystalline structures, the electrons can be focused on a region of interest and the aperture has to be changed to inhibit passing of unscattered electrons. Not only the intensity of electrons can be used to create direct images of structures. In High Resolution TEM (HRTEM) the phase information of the electron waves can be used to achieve atomic resolution. Since the phase information cannot be directly measured, the electron beam has to be split up into a specimen beam and a reference beam and both beams are focused on the detector. This results in a phase contrast on the detector and spatially resolves the atomic order.

2.1.6 Scanning Electron Microscopy

The atomic layer deposition of thin films allows conformal deposition into any kind of structures. For sectional views of thin films, scanning electron microscopy (SEM) can be applied. SEM relies on the detection of secondary and back-scattered electrons from the surface of a specimen [57]. In contradiction to TEM, only a very small focused electron beam is used to generate a picture. Electrons are emitted from an electron gun and accelerated by up to 30 kV. The resulting electron beam is modeled in shape and focused on the surface of the specimen by

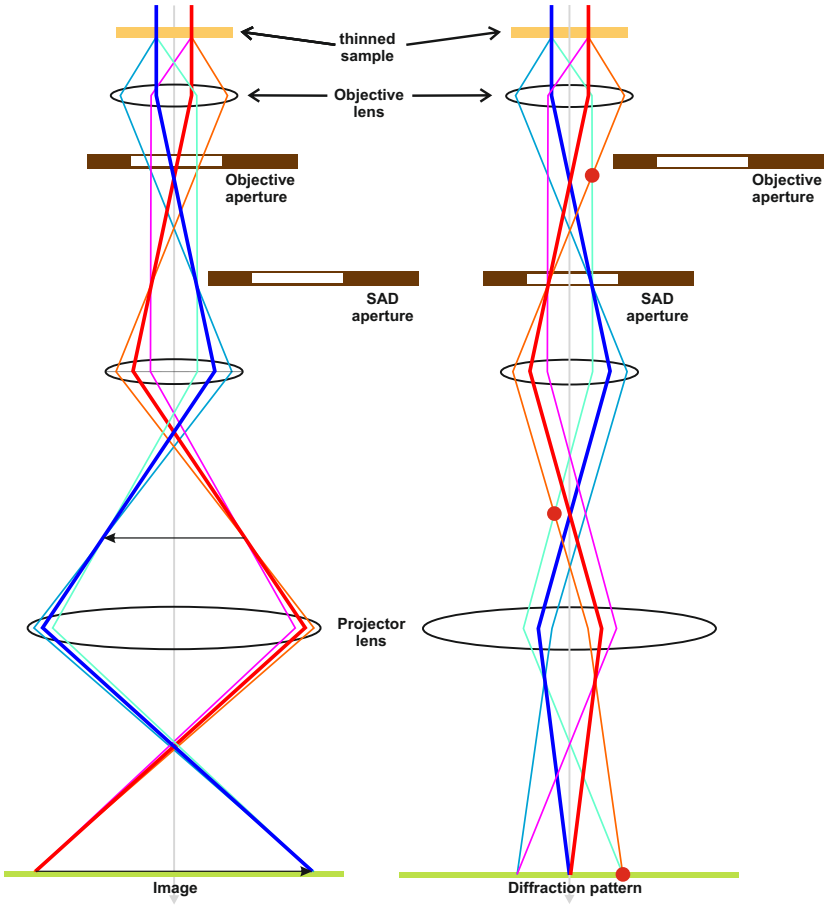

Figure 2.8: Principle of transmission electron microscopy. An electron beam is optimized to pass a thinned specimen. The electrons scatter on regular crystalline patterns and the diffraction pattern can be imaged in the right. Filtering of scattered electrons enables direct imaging of the investigated samples' region on the left. After [56].

a complex condensor lens system. To built up a picture, the electron beam is scanned over the surface by deflection coils and the detector signal is synchronously converted into a greyscale. The incident electron beam penetrates the specimen depending on the accelerating voltage and the material properties. The interaction of the electron beam basically involves emission of secondary electrons (SE) and backscattered electrons (BSE). SE are excited from atoms of the specimen. Since the electron beam can penetrate the matter, secondary electrons contain information down to a certain depth of several nm. Therefore, SE allow to map topographic pictures and does only contain electron information on a very small regime as compared to BSE. Reasonably, the SE enable a very high resolution. Tilted surfaces, as well as edges appear different in the SE mode. This knowledge can be applied, to reinforce the contrast by tuning the landing or the acceleration voltage. BSE electrons are of several keV energy and allow to generate contrast of different materials. Here, the material contrast depends mainly on the atomic number.

2.1.7 Atomic Force Microscopy

Atomic force microscopy (AFM) is a scanning probe microscopy method to resolve the topographic information from objects. In 1986, the inventors Binnig, Quate and Gerber already demonstrated the ability of AFM to resolve vertically less than 1 Å in air [58]. AFM is based on the measurement of ultra low forces on a probe tip while the line-by-line scan over surfaces. Such forces can be Van-der-Waals forces or simply the reset force of the cantilever on which the tip is mounted. AFM can be done in different modes as depicted in figure 2.9. Among these, the contact-mode is the simplest. The AFM probe on a cantilever is in contact with the specimen. While the scan, the deflection is measured and the topographic information is taken. Here only a fixed average distance from AFM probe to the surface to the region of interest of the specimen is needed.

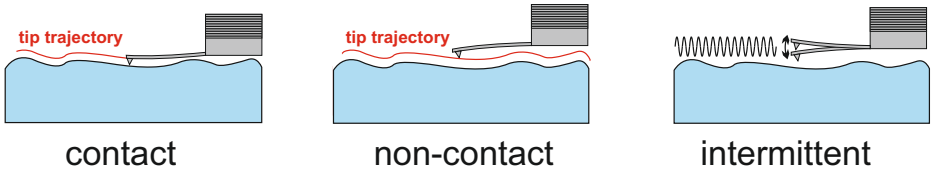

Figure 2.9: The three different AFM scan modes from left to right: The contact mode, the non-contact mode and the intermittent mode.

For sensitive surfaces the non-contact mode can be used. While the non-contact mode the AFM probe is in a close approach to a surface. Here, the Van-der-Waals forces deflect the cantilever. Thus, damage of the AFM tip can be prevented as compared to the contact mode which needs regular replacement of the AFM tip. Usually, in the non-contact mode, the AFM probe is excited to very small oscillations in resonance. In this range the Van-der-Waals forces change the frequency. At ambient conditions, the sample develop a liquid meniscus which attracts the AFM probe in approach. Thus, to regulate a constant distance to the surface is quite

complicated. The intermittent mode represent an improved non-contact mode to overcome this problem. The AFM probe is excited to oscillations and the phase as well as amplitude response is measured. When the AFM probe is getting close to the surface, the amplitude is reduced and the AFM probe can be lifted up. In addition to the topographic information, also other physical parameter can be recorded. For example Kelvin probe or current measurements by the AFM probe are possible. In figure 2.10 the basic working principle of an AFM is exemplified for the intermittent mode. The AFM probe is mounted onto Piezo crystal to actuate ultra precise scanning over the specimen in x, y, and z-direction. Depending on the distance to the surface, the amplitude of the oscillation changes. The change is measured as the deflection in height measured optically by a position sensitive detector (PSD) and the resulting signal is digitized. A change in height corresponds an error signal which is used to readjust the tip height above the surface. The readjustment is carried out by an DSP[3]-based z-feedback PI controller to enable accurate and fast response to the error signal. This allows to keep the forces in average constant while the scan and minimizes measurement errors. The error signal is recorded as topographic information and can be individually manipulated for example to correct the curvature of a substrate and remove scan errors.
The investigation of surfaces by AFM has to be carried out carefully. Besides artificials, also wrong usage can falsify the surface analysis of thin films. From technical point of view, the control P constant has to be adjusted correctly, otherwise each steep topographic object on the surface cause a jump of the probe and the surface information is strongly influenced. Another problem in thin film surface analysis by AFM is that sufficient data have to be collected. If crystallization takes place while thin film growth, large crystallites can falsify the determination of the rms roughness. This is taken into account by the dynamic scaling theory. The dynamic scaling theory describes the influence of the growth time while continuous growth and the AFM scan length [59]. If large objects are grown within a smooth thin film, the scan length has to be chosen high enough, otherwise the rms roughness is underestimated. Hence, saturation of the roughness has to be proved as a function of the scan area if crystallization occurs.

[3]DSP = Digital Signal Processor

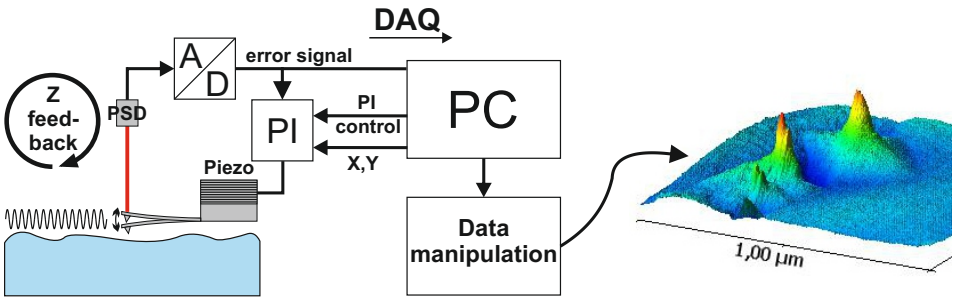

Figure 2.10: Technical principle of atomic force microscopy in the constant distance mode. The surface is scanned by the probe in XY direction. The deflection is measured by an phase sensitive detector (PSD). The derived error signal is fed as an Z-position feedback into a PI controller and the probe height is readjusted while scanning over the topography. The data are recorded by a computer and can be manipulated to accurate data interpretation.

2.1.8 Raman Spectroscopy

Raman spectroscopy is based on the scattering of light on matter which wavelength is much more greater as compared to atoms, molecules, and the inter atomic distance in a solid [60]. Reasonably, the interaction is of totally different nature as compared to x-rays or electron scattering. Scattering of light in the UV-VIS and IR range can be subdivided into Rayleigh scattering and Raman scattering. Rayleigh scattering is elastic and the photon energy is not changed. The Raman process happens inelastically and incident and emitted photon are different in energy. The shift in wavelength, the Raman shift is characteristic for the specific matter. Thus, Raman spectroscopy can be utilized to reveal phases in matter. The Raman effect can be explained by the change of the polarizability by the incident light. In classic theory polarization by light is described by an electric field [61]

$$F = F_0 \cos(2\pi\nu_0 t) \tag{2.20}$$

of the frequency ν_0 stimulating polarization. In a diatomic molecule the polarization writes

$$P = \alpha F = \gamma F_0 \cos(2\pi\nu_0 t) \tag{2.21}$$

where α denotes the polarizability. An molecule exhibits vibrational states with a motion

$$q = q_0 cos(2\pi\nu_m t) \tag{2.22}$$

with the frequency ν_m. As a consequence of the molecular vibration the polarizability changes as a function of the deflection. For small deflection the polarizability can be approximated

$$\gamma = \gamma_0 + \left(\frac{\partial\gamma}{\partial q}\right)_0 q_0 + ... \tag{2.23}$$

with the equilibrium polarizability γ_0. Hence the polarization can be rewritten to

$$P = \underbrace{\gamma_0 F_0 \cos(2\pi\nu_0 t)}_{\text{Rayleigh}} + \frac{1}{2}\left(\frac{\partial\gamma}{\partial q}\right)_0 q_0 F_0 \left\{ \underbrace{\cos(2\pi[\nu_0 - \nu_\mathrm{m}])}_{\text{Stokes}} + \underbrace{\cos(2\pi[\nu_0 + \nu_\mathrm{m}]\,t)}_{\text{Anti-Stokes}} \right\} \tag{2.24}$$

The first term of the polarization describes the Rayleigh scattering, the second term and the third term reveal that by Raman scattering the frequency is shifted by $\pm\nu_\mathrm{m}$. A shift to lower frequency is called the Stokes shift and in analogy the Anti-Stokes shift describes the shift to higher frequency. In crystalline solids the whole lattice vibration is described by phonons. The transfer of energy to and from a phonon is schematically depicted in figure 2.1.8. Since the annihilation and creation of phonons underlie the boson statistic the intensity ratio between Stokes and Anti-stokes line is given by [62]

$$\frac{I(\nu - \nu_\Omega)}{I(\nu + \nu_\Omega)} = \exp\left(-\frac{h\nu_\Omega}{kT}\right) \tag{2.25}$$

That means, that the Stokes line is in intensity much more higher as compared to the Anti-Stokes shift. Thus, the measurement of the Stokes shift is experimentally preferred for the determination of phases in a solid by Raman spectroscopy. The detection of phases by the Raman effect is related to the structural properties of the crystal lattice. As already stated in equation 2.23, the polarizability needs to be changed while the lattice vibration, otherwise a certain phonon mode across the lattice is not Raman active. This leads to selection rules according to symmetry operations for the Bravais lattice [61].

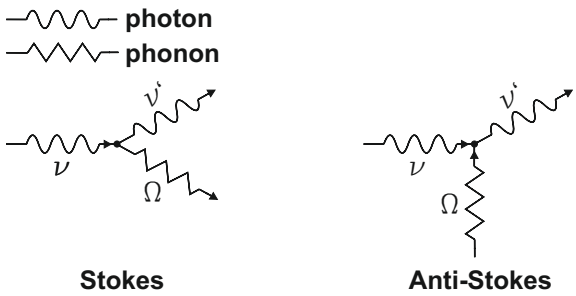

Figure 2.11: Principle of the Raman effect: The Stokes shift describes transfer of the energy to matter of an incident photon of the frequency ν. Their energy is split up into a portion exciting vibrational, a phonon for example and a portion of energy emitted into a secondary photon. While the Anti-Stokes shift, the re-emitted photon absorbs the vibrational energy of the matter.

2.1.9 Measurement of Optical Properties by Ellipsometry

For the determination of the optical dielectric properties of thin films ellipsometry can be utilized. The ellipsometry is based on the measurement of the polarization of a reflected or transmitted light in the UV-VIS regime. For the analysis of thin films on non-transparent substrates, the polarization of reflected linear or circular polarized light is measured. Polarized light can be described as superimposition of a parallel (p) and perpendicular (s) orientated electrical fields $\vec{F}$ to the plane of incidence. The phase shift between the parallel $\vec{F}_p$ and $\vec{F}_s$ component is arbitrary for elliptic polarized light, while the incident beam, for example circular polarized has got a fixed phase shift of 90 °. In ellipsometry the phase shift Δ of the reflected beam is measured by the complex reflectance ratio ρ [63]

$$\rho = \frac{r_\mathrm{p}}{r_\mathrm{s}} = \tan(\psi)\exp(\Delta) \tag{2.26}$$

where ψ is the amplitude component of the polarized light and r_s and r_p as schematically shown in figure 2.12.

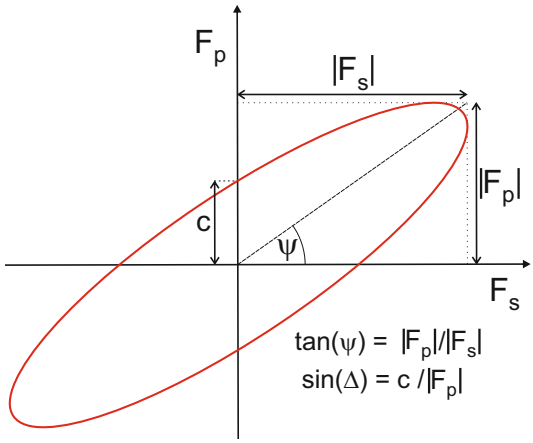

Figure 2.12: Phase shift and amplitude component as a measure of the elliptic wave vector components.

For layered and multi-layered systems quite complex model functions are needed to determine the refraction of a specific layer. The complex reflection components of the layer of interest are [49]

$$r_\mathrm{layer,p} = \frac{\tilde{n}_1\cos\tilde{\phi}_0 - \tilde{n}_0\cos\tilde{\phi}_1}{\tilde{n}_1\cos\tilde{\phi}_0 + \tilde{n}_0\cos\tilde{\phi}_1} \tag{2.27}$$

$$r_\mathrm{layer,s} = \frac{\tilde{n}_0\cos\tilde{\phi}_0 - \tilde{n}_1\cos\tilde{\phi}_1}{\tilde{n}_0\cos\tilde{\phi}_0 + \tilde{n}_1\cos\tilde{\phi}_1} \tag{2.28}$$

where $\tilde{n}_0$, $\tilde{n}_1$ are the refractive indices and $\tilde{\phi}_0$, $\tilde{\phi}_1$ are the corresponding refraction angles as depicted in figure 2.13.

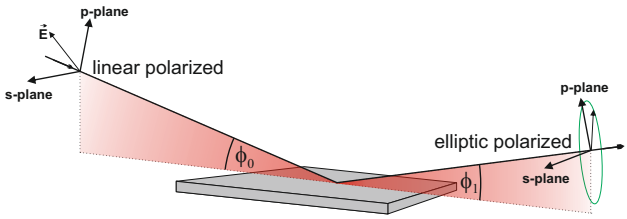

Figure 2.13: Reflection of linear polarized light on a surface. By reflection the light is elliptically polarized.

The relation between the refractive index

$$\tilde{n} = n + i\kappa \tag{2.29}$$

and the dielectric function

$$\tilde{\epsilon} = \epsilon_1 + i\epsilon_2 \tag{2.30}$$

is given by

$$\epsilon_1 = n^2 - \kappa^2 \tag{2.31}$$

$$\epsilon_2 = 2n\kappa \tag{2.32}$$

where ϵ_1 is the dielectric permittitivity and ϵ_2 its complex number. κ denotes the extinction coefficient. Ellipsometry can be carried as a function of the wavelength. By this, the dielectric permittivity can be determined as a function of the photon energy. If ionic crystals are considered, the real part of the dielectric permittivity does not only depend on an electronic excitation according to the Lorentz oscillator model, also the ionic contribution has to be taken into account. Therefore, the real part of the dielectric permittivity reads [64]

$$\epsilon_1(h\nu) = 1 + \chi_{\text{el.}}(h\nu) + \chi_{\text{ion.}}(h\nu) \tag{2.33}$$

where $\chi_{\text{el.}}$ and $\chi_{\text{ion.}}$ are the electronic and dielectric susceptibility, respectively. Ionic excitation is linked to phonons, which exhibit excitation by infrared light. Excitation by UV-VIS light causes a maximum of the dielectric permittivity widely above the energy range of infrared light. Thus, the electrostatic dielectric permittivity can be derived from the optical dielectric function for low excitation frequencies according to

$$\epsilon_{1,\text{stat.}} = \epsilon_{1,\text{opt.}} = \epsilon_1(0) = 1 + \chi_{\text{el.}}(0) + \chi_{\text{ion.}}(0) \tag{2.34}$$

for the limit $h\nu \to 0$. In addition to that, the absorption coefficient α can be extracted from the imaginary part of the refractive index.

$$\alpha = \frac{4\pi\kappa}{\lambda} \tag{2.35}$$

From the absorption coefficient the indirect as well as direct band gap can be extracted. According to Tauc empiric formula [63, 65]

$$(\alpha h\nu)^n \propto (h\nu - E_g) \tag{2.36}$$

a $(\alpha h\nu)^n$ vs $h\nu$ plot allows to determine the band gap E_g. Indirect band gaps and band gaps of amorphous semiconductors can be derived for $n = \frac{1}{2}$ if a clear visible slope can be observed as a function of the photon energy $h\nu$. The band gap can be extrapolated from the elongation of the slope to the abscissa. For crystalline semiconductors direct band gaps can be estimated in the same manner by $n = 2$.

2.2 Electrical Characterization

To reveal the resistive switching properties and the transport phenomena different kind of electrical measurements were carried out on nano-sized cross-point ReRAM devices. Nano-sized devices does generally exhibit higher resistances as compared to larger μ cross-point ReRAM or simple stacks with pads as top-contact. Hence, the requirements on the test equipment are high accuracies.

2.2.1 Automated IV-Characterization

Nano cross-point ReRAM is a passive device which do not has an extra integrated transistor to limit the current as compared to 1T1R memory. For the quasi-static resistive switching characterization active control of the switching current compliance and excellent constant timing are required. Otherwise very high current overshoots and strongly deviating switching voltages make reproducible IV characteristics impossible. Therefore, very precise sourcemeters or source-measurement-units were utilized in this work to ensure such high accuracies. Besides precise electrical measurement, statistical deviation by the fabrication process of nano devices has to be taken into account. As depicted in figure 2.14(a) several hundreds of devices exist on a single test die. Their resistive switching properties like initial resistance, the electroforming and SET voltage, the DC-nonlinearity and the RESET current need to be analyzed in mass. For that purpose, an automated probe station as shown in figure 2.14(b) can be utilized. Such a tool allows automatic stepping from to device to device on a die after pre-defined measurement routines as well as temperature dependent experiments above room temperature. The organization of sample sets, on maybe different device mask designs, and mass data analysis represent a tremendous expense in data processing. To handle that labor force, RSAS [4] was developed as graphical user interface to simply overload mass data as well as single measurements with a flexible click on mask graphical interface.

[4] ©RSAS = Resistive Switching Analysis Software, programmed by M.Reiners.

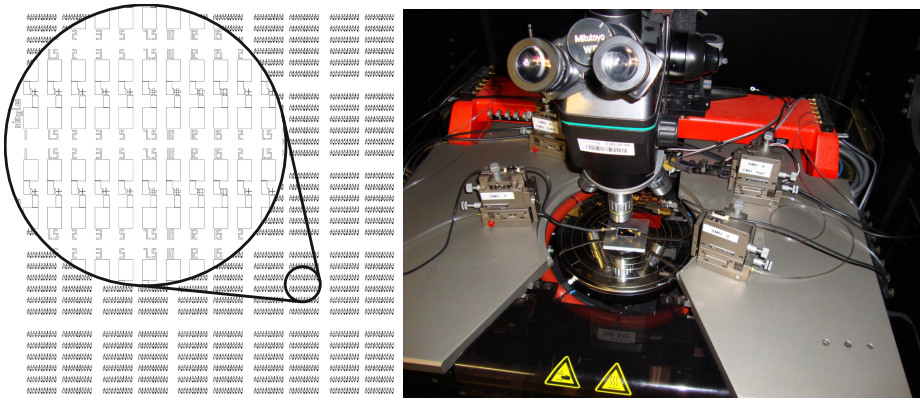

(a) (b)

Figure 2.14: (a) Mask design of single ReRAM devices arranged on a die. (b) Photography of a probestation for automated electrical characterization. The probe tips can be manually set by the manipulator arms to fixed positions, the die position can be changed by step motor actuation. Movement in Z-direction enables electrical contact to single devices on the die.

2.2.2 Low Temperature Conductivity Measurements

For the determination of the transport mechanism low temperature measurements are needed. In general, low temperature measurements represent large technical effort to ensure that a specimen can be carefully cooled down and warmed up. Ultra high vacuum (UHV) is required to isolate the cryostat and the cooling liquids from the outer hot surrounding. Usually, very small specimen chambers are cooled in a bath cryostat utilizing He as contact gas or He flow cryostats are used. Such configuration are not very flexible, since only a few devices can be hard-wired. To circumvent such problems cryogenic probe stations can be used. The setup of such a station is schematically depicted in figure 2.15(a). The probe station consists of an outer chamber, an inner radiation shield, and within the radiation shield a He cooling finger. To contact a specimen a sample stage is mounted onto the cooling finger. The devices on a die can be contacted by spring-mounted tips which compensate temperature expansion of the probe arms as depicted in figure 2.15(b). A disadvantage of this system is that the inner chamber is evacuated to UHV condition like the outer chamber. Hence, no He contact gas can be used to guarantee overall cooling of the specimen. Further the radiation shield emits IR radiation because it is not cooled by the back flowing He gas. Devices on a die are on the surface and therefore are immediately influenced by the radiation. For that reason, a reference sensor was additionally installed consisting of a piece of wafer and a resistor temperature sensor. The was fixed in the same manner like the specimen die. Slow cooling was achieved by an additional needle valve inserted into the He back flow line. By this, very low cooling rates below 0.01 K/min are possible and the heat exchange between sample and sample stage has time to take place.

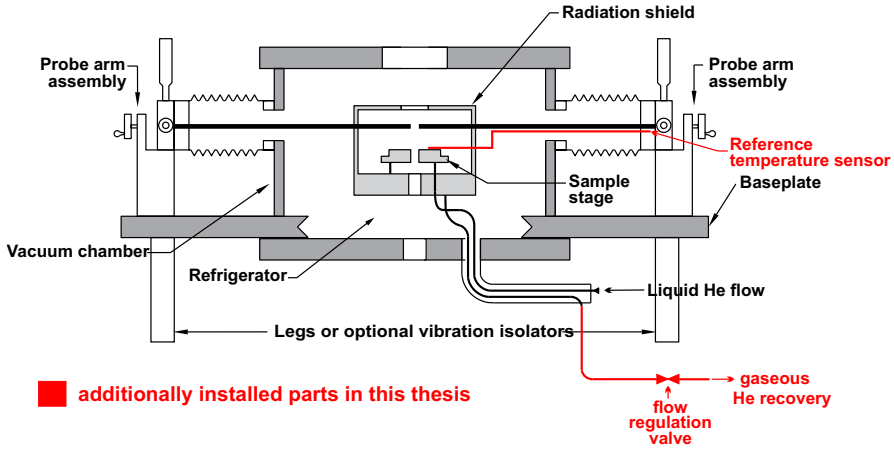

(a)

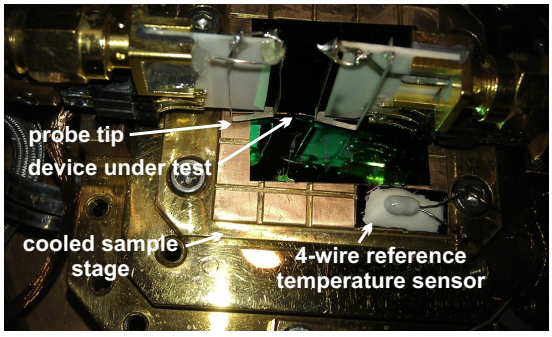

(b)

Figure 2.15: (a) Technical scheme of the used cryogenic sample stage for temperature dependent device mneasurements. Taken from [66] with permission from the author. (b) Photography of an installed sample and the reference sensor on the sample stage. The device under test is contacted by flexible probes.

CHAPTER

THREE

ATOMIC LAYER DEPOSITION OF TITANIUM OXIDE

This chapter is devoted to the development of different ALD processes for the growth of TiO_2 by Atomic Layer Deposition (ALD). A short introduction into the basic principles of ALD and liquid-injection ALD will be followed by the depositions of three different precursors for the growth of TiO_2. The evaluation of the processes highlights the control on the concurring crystallization into different phases of TiO_2 by the physical influence of time and temperature while the crystallization. Hereby, the study on the thermal ALD process revealed the modulation of the chemically driven growth process by physically driven crystallization. In addition, the morphological and structural properties of the grown films are elucidated with respect to the requirements on TiO_2 for the resistive switching application.

3.1 Introduction into Atomic Layer Deposition

A very first report on ALD was published under the term Molecular Epitaxy by Kol'tsov at the Leningrad Technological Institute [67, 68] and later on applied as Atomic Layer Epitaxy (ALE) for the commercialized production of large-area flat panels based on ZnS thin film electroluminescence (TFEL) devices [69]. The term ALE is no longer valid, since the main focus of ALD moved to the non-epitaxial growth of thin films like high-k dielectrics in semiconductor industry and many other applications where epitaxial thin films are not required [70]. However, the basic working principle of ALE remained.

3.1.1 Principle of ALD

All ALD method are classified to the chemical vapor deposition (CVD). Gaseous precursors are applied for the growth of thin films, but the ALD growth mode strongly differs from the classic CVD mode. In classic CVD one or more precursor gases are delivered into a gas chamber where

they decompose or react to each other in the very first boundary layer of a heated substrate to the desired thin film as depicted in figure 3.1(a). In the sense of the ideal ALD growth mode such reactions are generally forbidden. To prevent them, the two-precursor gas phase reaction

$$\mathrm{MeR_x} + 2x \cdot \mathrm{O} \longrightarrow \mathrm{MeO_x} + x \cdot \mathrm{O{-}R} \tag{3.1}$$

here exemplary written for oxides, has to be split up into two half reactions steps. This requires physical separation of the precursor gases as well as the active involvement of the substrate surface into the reaction as shown in figure 3.1(b). Thus, the ALD reaction steps become

$$\mathrm{surface} + \mathrm{MeR_x} \longrightarrow \mathrm{surface} - \mathrm{MeR_{x-y}} + y \cdot \mathrm{R} \tag{3.2}$$

$$\mathrm{surface} - \mathrm{MeR_{x-y}} + (z+v) \cdot \mathrm{O} \longrightarrow \mathrm{surface} - \mathrm{MeO_v} + [(x-y)\mathrm{R} + z\mathrm{O}] \tag{3.3}$$

The metal source precursor chemisorbs on a site on the surface as depicted from step A to step B in figure 3.1(b) by the exchange reaction 3.2. Hereafter, remaining physisorbed precursor and precursor in the gas phase needs to be purged away. The second half reaction 3.3 addresses the surface reaction of the chemisorbed species with the second reactant from the gas phase. By this, the final thin layer grows. In addition to this, new chemisorption sites are created on the new surface and recover the surface for the next ALD deposition cycle. The example elucidates that ALD relies on the chemisorption. Hence, ALD is a self-limited growth mechanism. This is of great importance, since all advantages of ALD over other deposition methods are attributed to the self-limited surface reactions. A fully saturated ALD growth cycle has got a stable self-defined growth rate, known as growth rate per cycle (GPC) which allows perfect control over the thin film thickness. The surface reactions do not need well-defined flux rates only saturation is needed for a stable GPC. Thus, uniformity over arbitrary large areas can be achieved in an idealized ALD growth mode. As long as the surface reactions are saturated conformality with unlimited aspect ratios are theoretically possible.

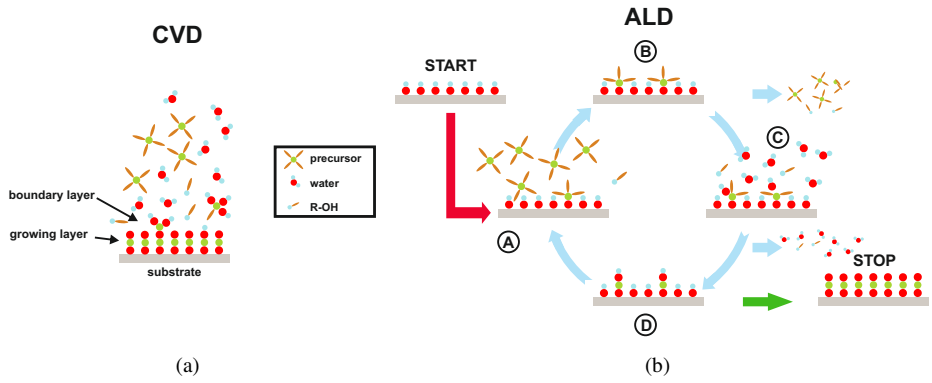

Figure 3.1: (a) Principle of two reactant CVD: Two species react to deposition material in the gas phase in the boundary layer of a substrate. (b) ALD principal: Subsequent self-limited reaction of two separately introduced precursors on the surface of a substrate. Repitively precursor delivery and purge steps from Ⓐ to Ⓓ controls the growth rate.

However, the surface reactions 3.2 and 3.3 only exemplary describe an idealized ALD process. The underlying processes is much more complicated and need further consideration to formulate the requirements on the surface chemistry for a nearly perfect ALD process. In figure 3.2(a) the GPC is modeled as a function of the precursor delivery time. Basically, the saturation is a time dependent process. Reasonably, the reactivity of the precursor is an important factor to settle to a stable GPC value. As a consequence, high reactivities decreases the saturation time. Besides the reactivity on the surface, the used precursors should not etch the grown film. This has been observed while the attempt to deposit ternary compounds by ALD [71]. Furthermore, the precursor should not decompose at given growth temperature. Otherwise, no clear saturation can be basically achieved and the GPC would be time dependent.
Besides saturation time dependencies, the GPC is influenced by the growth temperature. This can have several reasons as schematically depicted in figure 3.2(b). Slow reaction rates may lead to an activation of the chemisorption process and therefore to an increase of the GPC until all reaction sites contribute to the growth. A reciprocal behavior at low temperatures may arise from temperature dependent desorption from multi layered absorbed species or simply by condensation of a precursor. Higher temperatures can affect the thermal decomposition of the precursor on the substrate surface or cause its temperature programmed desorption. Tuomo Suntola suggested that a precursor should enable a wide temperature window where the GPC is stable and does not underly such phenomena [70]. This is called the ALD window or ALD process window. Within the ALD window, a precursor should fulfill a high reactivity on the surface sites to enable fast saturation and high growth rates, it should not thermally decompose on the surface within the window, and should not show any temperature dependence of the self-saturated growth mechanism. Of course, such a process stability cannot be reached over an arbitrary temperature window. Thus, precursor design and evaluation of the ALD process are hot topics in ALD research. Because the fact, that temperature dependencies may arise, not only precursor design is of importance, reasonably stable ALD reactors which are characterized by low temperature deviations over wide areas are needed. This is further of tremendous importance, since crystallization of ALD grown compounds tend to induce temperature dependent crystallization effects [72, 73].

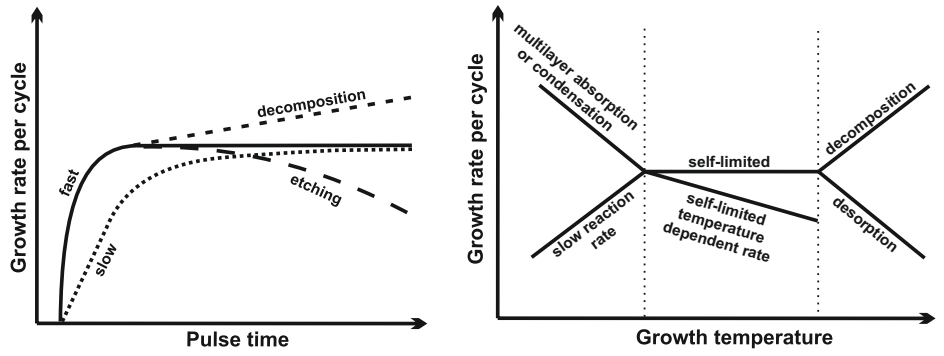

Figure 3.2: (a) Growth rate per cycle as a function of distinct surface reaction models. (b) Deviations from the idealized self-limited growth rate per cycle dependent on the growth temperature.

3.1.2 ALD Reactor Design

Basically, two types of ALD reactors exist. Their distinction is made by their pressure range and gas transport system. Ultra high vacuum (UHV) and high vacuum (HV) reactors are the simplest construction. UHV/HV reactors' working principle simply involves precursor gas inlet and re-evacuation sequences. Such a reactor design does allow easy evaporation of precursors but suffer from their long re-evacuation periods until a subsequent half-reaction step can be done [71]. Similarly, the dosing time of the precursor is high since only a few species hit the substrate surface. Thus, UHV/HV reactors are mainly applied in research reactors to allow in-situ investigations on precursor decomposition and reaction mechanism. While such experiments, an exact control of the substrate's temperature is difficult to handle. The heating of the substrates needs a well direct thermal contact to a sample stage. Otherwise, only heat radiation transfers energy to the substrate and the temperature of the substrate is compulsory always dramatically lower than the temperature of the heating stage. This makes fast sample exchange difficult because a sample has to be always glued by thermal-conducting materials onto the sample stage. Reasonably, on UHV reactors the evaluation of the ALD window might be difficult to conduct and the ALD window could be falsified. The second type of ALD reactor is based on continuous flowing inert process gases. Inert process gases allow fast purging and transport of the precursor gases. The pressure in flow-type ALD reactors ranges from around 1 hPa up to atmospheric pressure. Therefore, the temperature control by sample stages is well ensured by the process gases which act as thermally conducting medium. Like in CVD systems, the precursor vapor pressure needs to be in the range of the process pressure to guarantee fast saturation while the chemisorption on the substrate surface. Precursors with high vapor pressure can be kept in metal bottles directly connected to the reaction chamber by a valve. In case of precursors with low vapor pressure a

bubbler and maybe some moderate warming is needed to increase the transport of the precursor and its vapor pressure, respectively. Especially in industrial ALD reactors precursor bubblers are standard since a process gas flux of several slm is needed [71].

3.1.2.1 The Liquid Delivery - ALD reactor

In standard flow-type ALD reactors the saturation by the precursors is accomplished by bubblers which feed the precursor into the reactor chamber. As already presented in the foregoing sections 3.1.1 and 3.1.2 this may be time consuming if the precursor reactivity is low or the vapor pressure of the precursor is not sufficient enough to achieve precursor concentration that make saturation time scales negligible. This also addresses solid precursors which generally do not exhibit high vapor pressure as compared to liquid ones. The delivery of precursors of low reactivity and low concentrations can be technologically solved by the liquid injection technique where a liquid or solution of the precursor is injected into a vaporizer at a sufficient temperature. That means, in a very short time scale high concentrations of any kind of precursor can be achieved inside the vaporizer. The precursor gas mixture can be delivered into the reactor chamber. This technique enables faster saturation as compared to bubbler based delivery. In figure 3.3 the custom-built ALD reactor is schematically depicted which is used for the liquid-injection ALD (LI-ALD) in this thesis. The system comprises two main parts, a plug-flow type reactor (Aixtron FE 200) and a vaporizer unit (Jipelec). Liquid and dissolved precursors can be injected into the vaporizer and the precursor and purge gas flux is switched by high temperature valves between the exhaust and the reactor chamber. Within the reactor, a rectangular liner is installed to make the gas flow laminar over a susceptor designed as receiver for IR radiation. This enables contact free heating of the susceptor.

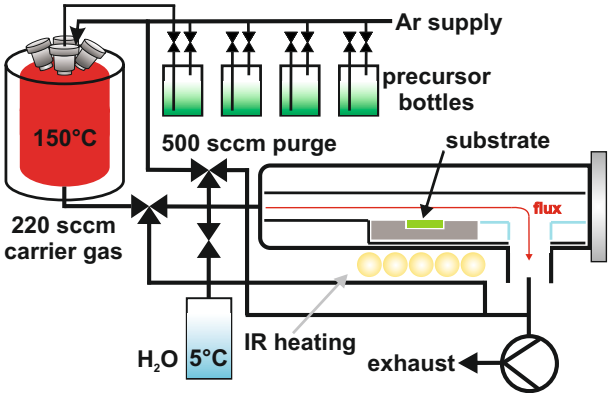

Figure 3.3: Illustration of the used Liquid-Injection-ALD reactor. Liquid and dissolved precursors can be injected into a vaporizer separated from the reactor. The generated precursor gas is fed to a plug-flow type reactor chamber.

The sample is rotated on a disk within the susceptor as shown in figure 3.4. For the precur-

sor delivery usually 0.1 mol/L solutions of precursors are prepared. The solutions are kept in reversely installed bubblers which are pressurized up to 2 bar by inert Ar gas. This ensures stable injection by Bosch injectors originally produced for automotive application. In comparison to standard ALD, the injection sequence can be done in two ways. By short injection pulses with fixed length of a few ms or by defined number of injections as depicted in figure 3.5. The injection sequence can be fully described by the injection frequency f, the opening time of the precursor injection and the number of injected pulses. The duration of the injection sequence is at minimum determined by the reciprocal frequency times the number injections, but is not allowed to be below ca. 1.7 s, otherwise machine timing problems cause process instabilities. For the growth of TiO_2 water was used as counter-reactant to oxidize the metal source precursors. Water has got a high vapor pressure and is therefore kept at 5 °C to minimize the purging time after oxidation.

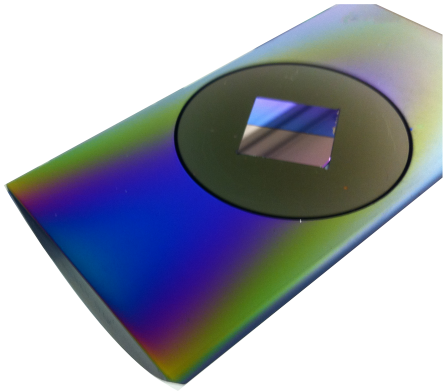

Figure 3.4: Photography of the susceptor installed in the FE 200 reactor showing the rotating disc with the 1" × 1" substrate recess.

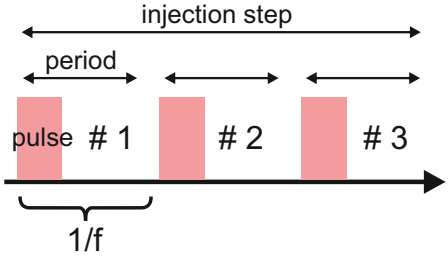

Figure 3.5: Injection sequence of the dissolved or liquid precursor. A specific number of short injection pulses can be repeated within a period $1/f$.

3.1.2.2 Reactor Dependent Flux Characteristics

In commercialized ALD systems the bubbling of precursor is usually mass-flow controlled. This ensures that the pressure in the systems does only weakly fluctuate. Liquid injection into a vaporizer opens up a new parameter tree since evaporation processes increase the pressure inside the vaporizer and in the ALD reactor at fixed pump capability. Reasonably, the mass flow, gas velocity, and remaining time of precursor staying within the reactor varies while injection. In addition to that, the carrier gas mass flow and the purge gas mass flow influence the precursor gas velocity within the reaction chamber. The purge is by-passed while the saturation feed step. Therefore, the gas velocity in the reactor decreases with increasing purge gas flow Q_{purge} and vice versa is proportional to the carrier gas flow Q_{carrier}.

$$v_{\mathrm{gas,reactor}} \propto Q_{\mathrm{carrier}} \tag{3.4}$$

$$v_{\mathrm{gas,reactor}} \propto \frac{1}{Q_{\mathrm{purge}}} \tag{3.5}$$

Once set, these two process parameters do not further affect the saturation behavior. But the vaporization much more influences the gas velocity by the injection frequency and the injector opening time. With increasing frequency and injector opening time the amount of precursor solution is increased at very short time scales and lead to an spontaneous decrease of the viscous gas flux. As a consequence, the gas velocity within the reactor chamber is decreased

$$v_{\mathrm{gas,reactor}} \propto \frac{1}{f_{\mathrm{injection}}} \tag{3.6}$$

$$v_{\mathrm{gas,reactor}} \propto \frac{1}{t_{\mathrm{opening}}} \tag{3.7}$$

Under the assumption, that the dissolved precursor vaporizes perfectly, the precursor concentration in the gas phase increases in the reactor while the gas velocity slows down. Compared to standard flow-type ALD, the saturation can be achieved within shorter time scales at high precursor surface reactivity. One drawback utilizing dissolved precursors may be lower vapor pressure of the precursor compared to the vapor pressure of the solvent. In this case, the solvent enriches in the vaporizer and is fed to the reactor chamber before the precursor concentration in the gas phase enters a level which allows saturation. This slows down saturation with time or, in worst case, the end of the injection sequence cuts off precursor saturation with injection sequence time. Therefore, no saturation of the GPC can be observed as a function of the injector opening time or number of injections. Extra long remaining time of the precursor within the vaporizer may cause its thermal decomposition and reasonably mass dependent deposition rate behavior will occur. This complicates the characterization of new precursors on LI-ALD reactors. In addition to that, it has to be taken into account that parts in the ALD system like the high temperature valves are bottlenecks for the gas flow and influence the precursor gas flow. The discussion points out that an excellent knowledge on the LI-ALD reactor is necessary. This can be done by gas flux simulation. But such a simulation does not allow the evaluation of the thermal decomposition and chemical reaction properties. Thus, the LI-ALD system itself

has to be pre-characterized by a full parameter tree set on precursors with known properties. In figure 3.6(a) and 3.6(b) the pre-characterization results for the growth of TiO_2 by tetrakis-dimethylamido-titanium and water are shown. For different number of injections the injection frequency was varied. To analyze the saturation of the process XRF was carried out on a Rigaku ZSX100e. The measurement of the Ti mass layer density clearly demonstrates that 3-4 injections at 4 Hz allows fast settling to the saturation level without any further dependence on the number of injections. Hence, these process conditions allow to characterize precursors with similar properties like TDMAT.

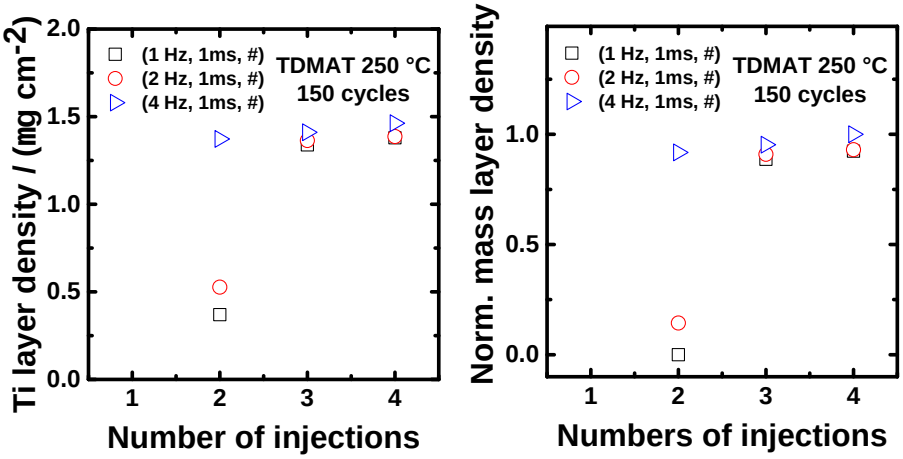

(a) (b)

Figure 3.6: (a) Ti mass layer density as a function of the number of injection pulses at fixed injection time and different frequencies. In (b) the corresponding plot normalized to the maximum layer density is depicted.

3.1.3 Precursors for the ALD growth of TiO_2

In section 3.1.1 the phenomenological influence of the precursor chemistry on the GPC is presented. Generally, high stability in the gas phase and on the surface as well as high reactivities are required for ideal ALD. Beside these requirements, also high volatility, less sensitivity to air and moisture, purity, and inexpensive synthesis routes are also desired. The by-product after half and full ALD cycle also need to be highly volatile and should be unreactive to prevent interaction with the growing film which may cause back etching or impurities. Also, aggressive by-products like halides, for example chlorine utilizing $TiCl_4$ for the growth of TiO_2 should not be used. Such aggressive by-products might damage metal parts within the ALD reactors. Reasonably, the trend in research moved away from such inorganic precursors to organic ones like β-diketonates for the growth of ternary group II oxides [74]. For the growth of group IV

oxides like HfO_2, ZrO_2, and TiO_2 alkoxides were thoroughly investigated [71, 72]. Among the alkoxide compounds small alkoxide rest molecules exhibit highest thermal stability, but tend to oligomerization which shifts evaporation temperatures. Only propoxides and higher alkoxides were reported as monomolecular skeletons. Under these, the Ti alkoxides show lowest thermal stability. Latest developments are cyclopentadienyls (CP). Bis-CPs were reported higher GPC as compared to Mono-CPs although high thermal stability was found [75]. Another class of precursors are dialkylamides which are generally known to be highly reactive while ALD [76]. This is known to be due to the link of N with a free electron pair in sp2-hybridization to the central Me atom. However, ALD with dialkylamides has to be conducted carefully since they are highly reactive to moisture and air and are unstable in solution. Thus, the latest trend in precursor design is the exchange of one or more of the alkylamide skeletons by bulkier ligands. This has been successfully demonstrated by replacing two of the alkylamides on tetrakis-diethylamide-titanium by isopropoxide [77]. Such mixed amide based precursors comprise the advantages of high reactivity from the amides and better thermal stability while the ALD growth. However, the replacement of alkylamides by alkoxide groups do leave an Me-C bond which may cause higher carbon content within the deposited film. With respect to this impurity incorporation, all nitrogen coordinated mixed-amide based precursors represent a solution. The growth of various oxides, giving Ta_2O_5 [78, 79, 80, 81, 82], HfO_2 [83, 84, 85, 86] and ZrO_2 [87, 88] as example was already carried out by utilizing mixed amide based precursors. Substitution of alkylamides by guanidinates was demonstrated to increase the thermal stability on ALD of several group(IV) oxides [76]. The enhancement of the thermal stability is based on the bidendate chelating leading to 5- and 6-fold N coordination to the central Me atom. Such precursors were also found to be less sensitive to moisture and oxygen as compared to alkylamides.

3.1.3.1 Thermodynamic Precursor Properties

In ALD research not only the capability of ALD reactor system has to be investigated. The thermal properties of the precursors in terms of high thermal stability in the gas phase and high decomposition temperature on the surface are of importance as already touched upon in section 3.1.1 and 3.1.3. Thermogravimetric analysis is applied to characterize the thermal stability and volatility of precursors. For that purpose, a small amount of several tenth mg of precursors is put into a microbalance as depicted in figure 3.7. Under continuous flow of an inert gas, the temperature is computer aided increased and by this the precursor vaporized while the mass is measured. This results in TG curves, which allow to qualify and compare precursors to each other [71].

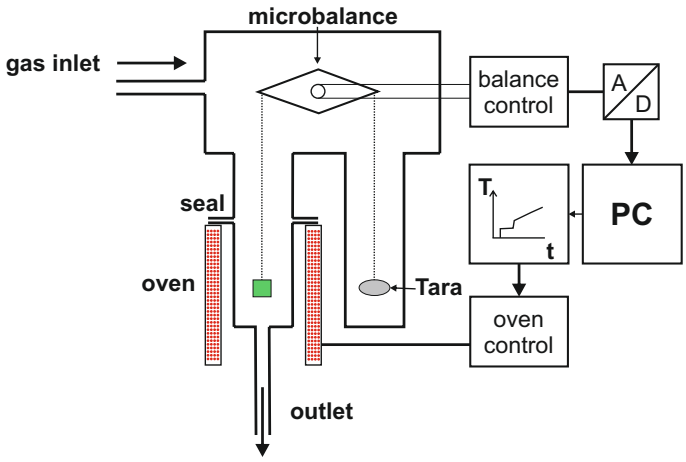

Figure 3.7: Schematical drawing of a microbalance for thermogravimetric analysis. Adopted from [89].

The TG profiles of the precursors, titanium-tetraisopropoxide {Ti(−$CH_2(CH_3)_2)_4$,TTIP}, tetrakis-dimethylamido-titanium {$(NMe_2)_4$−Ti, TDMAT}, and its derivative tris-(dimethylamido)-mono-(N,N'-diisopropyl-dimethyl-amido-guanidinato)-titanium {$[(N-iPr)_2NMe_2]Ti(NMe_2)_3$, TiA_3G_1 } used in this work are shown in figure 3.8(a). The TGA analysis was carried under inert nitrogen flow (300 mL/min, 99.9999%) utilizing a Seiko TG/DTA 6300S11. The heating rate was fixed at 5 K / min. Infered from the TG curves, all three precursors exhibit a clear single-step vaporization. Derived from the determination of the deflection points, the onsets of vaporization nearly overlap for TTIP and TDMAT with 99 °C and 103 °C, respectively. In case of TiA_3G_1 the onset was determined to 148 °C which matches the physical properties of the precursors states at room temperature: TiA_3G_1 is a solid, whereas TTIP as well as TDMAT are liquids at room temperature. However, all investigated precursors do not show any decomposition steps and exhibit a good volatility. The higher baselines of the TDMAT and TiA_3G_1 TG curves may result from partial oxidation of the amide based precursors to TiO_2 while transfer to the TG furnace.
Especially for the application in LI-ALD, the precursor should contribute to the vapor pressure, otherwise the observation of the saturation at low time scales can be difficult as discussed in section 3.1.2.1. In figure 3.8(b) the vapor pressure of the precursors and the used solvents is given as a function of the temperature. The vapor pressure curves allow to conclude that the precursors more contribute to the sum of total pressure by one order of magnitude at elevated vaporizer temperature. This demonstrates the importance of a high vapor pressure, even in the case of LI-ALD utilizing dissolved precursors. Alternatively, the vaporizer temperature can be adjusted to higher values which requires thermal stability of the ALD precursor.

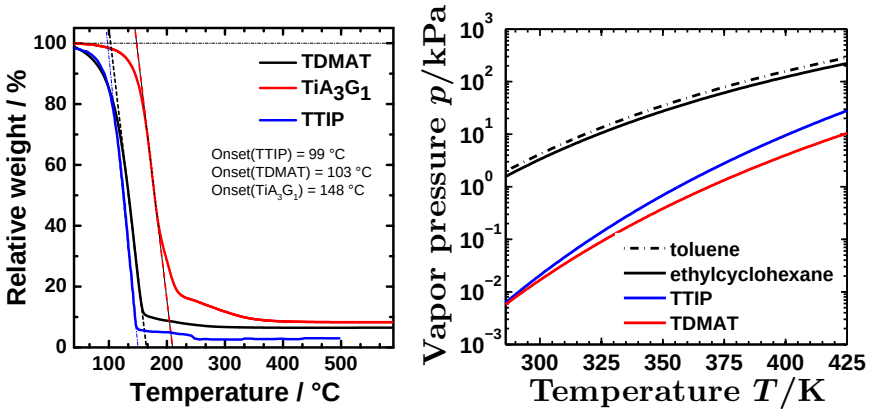

(a) (b)

Figure 3.8: (a) TG curves of TTIP, TDMAT and TiA_3G_1. The TG curve of TTIP is digitized from [76]. (b) Vapor pressure as a function of the temperature of the Ti precursors and the solvents for LI-ALD. The vapor pressure was calculated by taking the Antoine equation constants [90, 91, 92, 93].

3.2 Growth of TiO_2 by ALD

This section describes the process characterization of the different ALD processes. This is followed by the analysis of the crystallization process while ALD growth. It will be shown that this topic is highly important because vice versa this crystallization into distinct phases strongly influences the ALD growth behavior. The crystallization into different phases of TiO_2 will be explained by the crystallization kinetics. By this, a way will be presented how to enhance by the ALD process control: the amount of the rutile phase in the deposited films which is of significant importance for the resistive switching in TiO_2.

3.2.1 Process Characterization

As already mentioned, the ALD window strongly depends on the properties of the precursor system. The surface reaction processes are quite complicated and a variety of side reactions and products can form after each ALD half reaction. Therefore, predictions of the ALD behavior of a precursor are quite difficult and only trends can be assumed from precursor design to its final application while ALD growth. Thus, all precursors need to be finally characterized with respect to the reactor process parameter to allow the determination of the ALD window. Hereby, a nearly idealized ALD window is always the goal with only a weak temperature dependence of the GPC around the growth temperature and with acceptable (high) values of the GPC.

3.2.1.1 Growth of TiO_2 from TTIP and H_2O

The evaluation of the growth of TiO_2 by TTIP and H_2O will be first presented. TTIP was dissolved in ethylcyclohexane (0.1 mol/L) and for its characterization 4 injections at a frequency of only 0.5 Hz was chosen. The carrier gas and purge gas mass flow were set to 500 sccm Ar each. The full injection sequence was kept long at (X12-3.5-1.5-20.5) s [1] to ensure that all precursor was vaporized and fed to the reactor, and that a sufficient water purge was chosen. Thus, the saturation of the growth can be easily achieved as depicted in figure 3.9(a). At these conditions TiO_2 tends to crystallize above a certain thickness of around 8 nm [94] as plotted in figure 3.9(b). Below this thickness, TiO_2 grows in its amorphous phase with an GPC of 0.055 nm/cycle and an increase to approximately 0.13 nm/cycle was observed after crystallization at a temperature of 250 °C. Similarly to these findings, a transition of the GPC for ALD TiO_2 was also observed by other authors utilizing different Ti precursors and water. Aarik et al. report a GPC increase of about 1.4 growing TiO_2 by titanium-ethoxide and water [95], even GPC transitions by a factor from 3 - 4 were found for TTIP and water on Ru and Si, respectively [96]. In this current work, the growth rate dramatically increased with growth temperature

[1] In the corresponding publication the ALD sequence is denoted (X2-3-1-20.5). After publication a general timing error was found caused by the computer operation. The notation was corrected to the exact process step time constants. This is of importance for further discussion of the crystallization driven ALD growth effects of TiO_2.

from 250 °C to 275 °C above the critical thickness. Thermal decomposition of TTIP as straight forward explanation could be excluded because self-saturation of the precursor was observed even at high thicknesses as shown in figure 3.9(a).

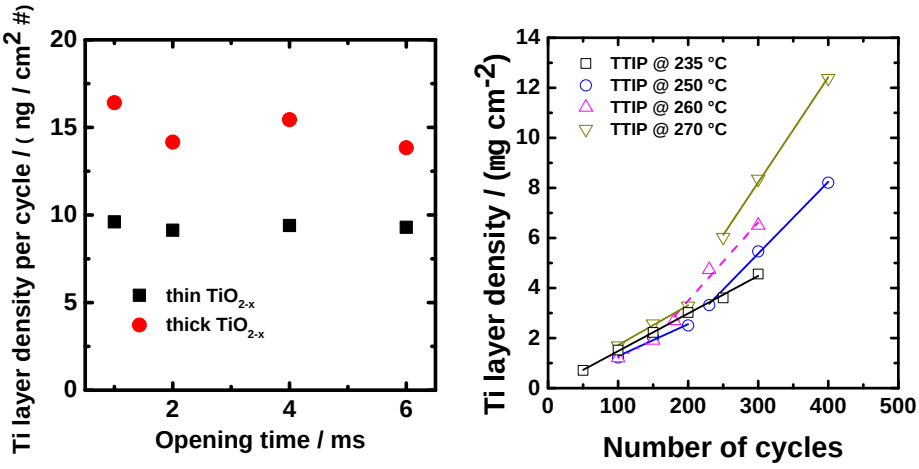

(a) (b)

Figure 3.9: (a) Saturation of the growth of TiO_2 by TTIP and water. (b) Ti mass layer density of TiO_2 films as a function of the cycle number at different growth temperatures.

3.2.1.2 TDMAT and H_2O

The former TTIP process required a long process time of around 38 s and the crystallization while the ALD growth mode depended on the thickness. To economically deposit TiO_2 by ALD an optimized process with respect to time is needed. In case of the TTIP process, the longest time is required for the feed and purge step of which endures around 20 s. It was already found by the LI-ALD reactor characterization in section 3.1.2.2 that injection frequencies of 4 Hz with only 3 injections lead to accurate saturated growth. From this starting point, the water supply and purging was further optimized for the TDMAT/H_2O process. In figure 3.10(a) the saturation of the TiO_2 growth by the Ti mass layer content is shown as a function of the water valve opening time at two distinct purge times. At 10.75 s water vapor purging, a clear mass dependency can be observed with increasing water opening time. For 20 s water purge time the Ti mass layer density is constant. From the comparison of the curves it can be concluded that the growth of TiO_2 by TDMAT and water is saturated at only 1 s water valve opening time. At 1 s the Ti mass layer value varied only by ~ 4 % for 10.75 s purge and 20 s. Therefore, water vapor can be sufficiently purged at only 10.75 s. Besides the oxidation of chemisorbed TDMAT by water, the ALD window needs to be examined as shown in figure 3.10(b). The Ti mass layer density does not depend on the injector opening time from 100 °C to 300 °C. This confirms saturation of the ALD growth of TiO_2 by TDMAT and water. The same experiment repeated

at 320 °C showed a CVD-like mass dependency on the injected amount of TDMAT solution as depicted in figure 3.10(c).

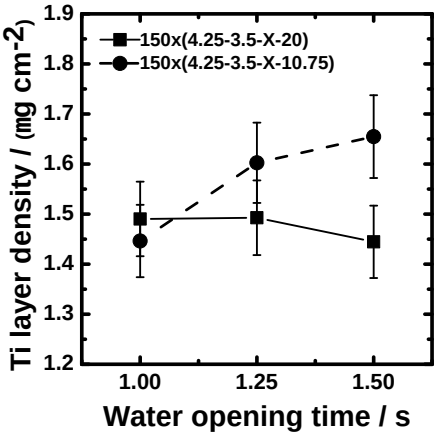

(a)

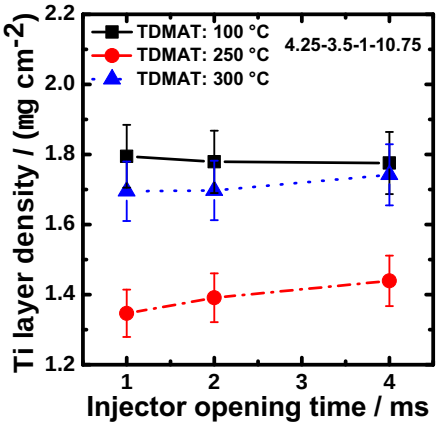

(b)

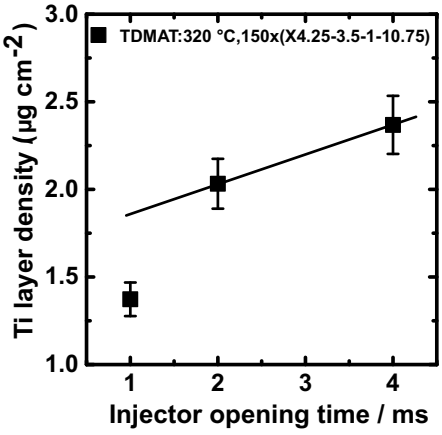

(c)

Figure 3.10: Ti layer density as a function of the precursor dose. In (a) the saturation by water supply is depicted for different subsequent purge times. In (b) the mass layer density is independent on the injector opening time from 100 °C to 300 °C, whereas mass dependency arises at 320 °C in (c).

From the slopes of the cycle-dependent experiments in figure 3.11 the GPC was exactly derived within the determined regime of saturated growth. The growth rate varies from 0.050 nm/cycle to 0.054 nm/cycle from 150 °C to 300 °C, respectively. In agreement with the mass layer density measurements in figure 3.10(b), the growth rate interestingly exhibits a minimum

between 200 °C and 250 °C. Other authors also report a decrease of the GPC with increasing temperatures [97, 98, 99, 100]. This can be caused by a condensation effect as mentioned in the introduction to ALD 3.1.1. Therefore, the purge time after precursor delivery was extended from 3.5 s to 10 s at 150 °C which resulted only in a deviation of about 1 %. From that, a temperature dependent desorption of TDMAT can be excluded as well as gas phase reactions of water and TDMAT at any temperature. Therefore, the increase of the GPC at 300 °C was adressed due to thermal decomposition of chemisorbed TDMAT. The thermal decomposition of TDMAT was thoroughly analyzed by Elam et al. [101]. This investigation on the growth of TiN from TDMAT and ammonia revealed that TDMAT already thermally decomposes at 180 °C for long time scales. However, the corresponding time dependent delivery and purge experiments demonstrate that the thermal decomposition of TDMAT has only to be considered at long time scales. In the current work, the injection time was varied at constant total delivery time of 4.25 s. Thus, time dependent thermal decomposition effects should not play a major role.

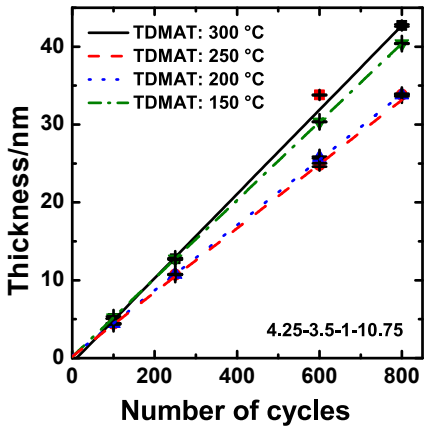

Figure 3.11: Thickness dependence of the TiO_2 films on the cycle number for different growth temperatures.

To finally qualify an ALD-type surface reaction with such a slight variation of the GPC, the conformal growth behavior was examined by the deposition of TiO_2 by TDMAT onto pin hole test structures. In figure 3.12, the SEM cross-sectional images of approximately 30 nm thick TiO_2 grown at 250 °C and 300 °C reveal an excellent step coverage over pinholes with an aspect ratio of about ~ 30. Thus, the decomposition rate at 300 °C is very slow in comparison to the oxidation rate of TDMAT for a full ALD cycle. At least, this confirms surface-controlled reaction in a limited manner [71]. Xie et al. found no increase of the growth rate in their experiments up to 350 °C for TDMAT. Unfortunately, their characterization were carried under UHV condition. As already discussed in section 3.1.2, missing heat exchange to the substrate surface under UHV condition can extremely increase the temperature difference between sample

holder and the substrate. Therefore, this results have to be carefully considered for comparative studies to flow-type reactor systems.

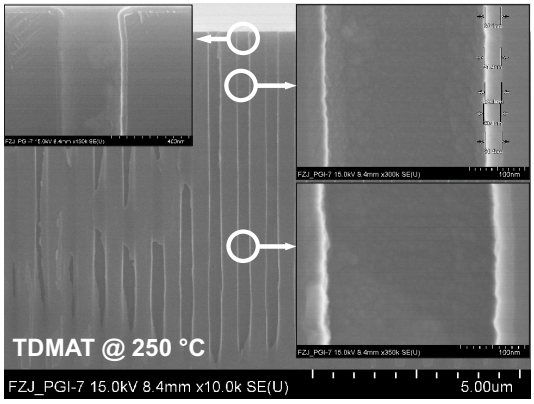

(a)

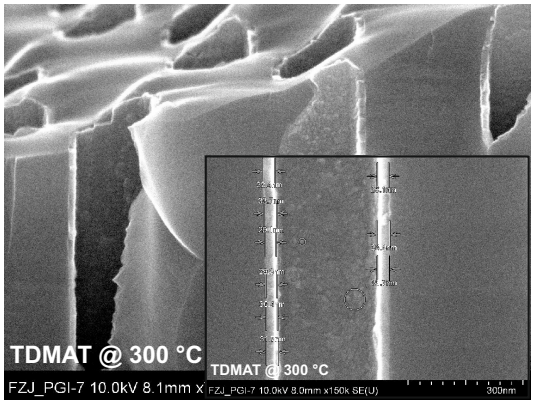

(b)

Figure 3.12: SEM profile image of 30 nm TiO_2 films deposited by ALD from TDMAT and water into pinholes of about 250 nm × 300 nm at 250 °C and 300 °C in (a) and (b), respectively.

3.2.1.3 TiA_3G_1 and H_2O

The characterization of TDMAT demonstrated that a nearly-ideal ALD window from 200 °C to 300 °C with excellent step coverage can be achieved. However, the major goal in ALD research, wide idealized ALD windows need a high upper temperature limit [102]. TiA_3G_1 was demonstrated as a potential precursor for the growth of TiO_2 by MOCVD [102] and the question arise if ALD can be carried with TiA_3G_1, too. In section 3.1.3.1 it was shown, that TiA_3G_1 starts to evaporate at ∼ 50 K higher temperatures as compared to TDMAT. Thus, the TiA_3G_1-solution (0.1 mol/L in toluene) may develop less TiA_3G_1 partial vapor as compared to

TDMAT. So, the number of injections was increased from 3 to 4 and the total precursor delivery time was extend to 6.5 s to ensure high concentrations of TiA_3G_1 in the ALD reactor chamber. The water vapor delivery and purging time were retained because the saturation by water and its purge efficiency does not change once established [71]. The saturation of the TiA_3G_1/H_2O process was carried from 250 °C to 350 °C. The data in figure 3.13 confirm saturated growth of TiO_2 from TiA_3G_1 and water from 250 °C to 330 °C. Above 350 °C, the process is strongly dependent on the amount of injected precursor solution. As already conducted for TDMAT, the GPC were extracted from cycle-dependent growth experiments at several temperatures shown in figure 3.14(a). Interestingly, the comparison of TiA_3G_1 and TDMAT in figure 3.14(b) reveals in both cases that the growth rate shows a minimum as a function of the temperature. The TiA_3G_1 /H_2O process is clearly advantageous over TDMAT since the variation in the GPC for temperatures from 200 °C to 300 °C is only at maximum ~ 6 %, whereas TDMAT exhibited an increase of ~ 30 % of the growth rate. This qualifies TiA_3G_1 a better ALD performance towards an ideal ALD window in this parameter range as compared to TDMAT.

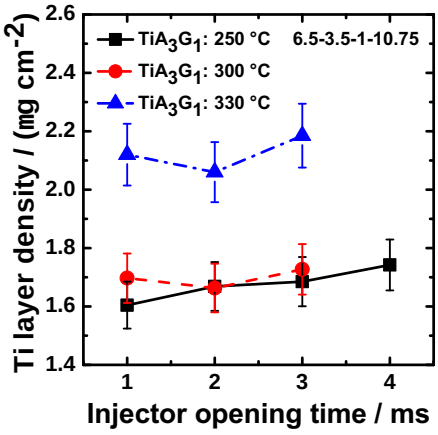

Figure 3.13: Ti mass layer density as a function of the injector opening time for different growth temperatures of TiO_2 grown by TiA_3G_1 and water.

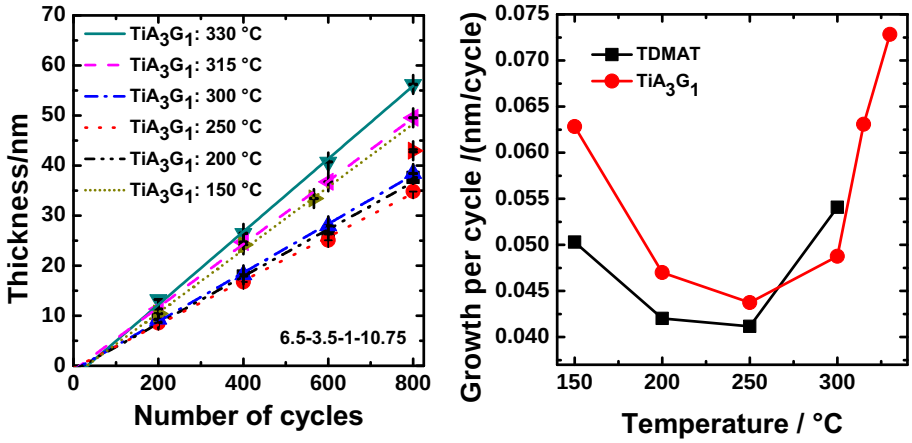

(a) (b)

Figure 3.14: (a) Relation between ALD cycle number and thickness of TiO_2 derived by TiA_3G_1 and water for different growth temperatures. For comparison, the GPC of TDMAT and TiA_3G_1 is plotted as a function of growth temperature in (b).

Nonetheless, the similar growth behavior of both precursors below their ALD window may be explained by the temperature-dependent desorption of water or dehydroxylation of hydroxylic groups on the surface. Egashira et al. analyzed the programmed temperature desorption of water molecules of the rutile as well as anatase phase of TiO_2. Desorption of physisorbed H_2O molecules was found on anatase from 69 °C to 127 °C and on rutile from 32 °C to 90 °C[103]. A second desorption peak is assigned to the chemisorption of hydrogen bond coordinated oxygen ions from 188 °C to 191 °C for both isomorphs. Only the rutile phase of TiO_2 shows desorption of directly oxygen bonded H_2O from 310 °C to 356 °C, which can be surface species of dissociated water on the rutile surface. On anatase TiO_2, synthesized by the pyrolysis of alkoxides, only a single desorption peak around 100 °C was detected, confirmed by infrared spectroscopy studies, while two desorption peaks of hydroxylic groups on rutile {110} planes were determined [104]. Recent studies clearly ascertain temperature-dependent desorption of H_2O from the rutile {110} surface, while the hydroxylic group density remains at constant level [105]. On anatase {100} and {110} crystal planes, simulation reveal similar desorption behavior in good agreement with spectroscopic observations [106]. To the best of this author knowledge, unfortunately no experimental data on the temperature-dependent desorption of water or its dissociates exists on amorphous TiO_2. Xie et al. proposed a model to explain the change in growth rate based on temperature-dependent desorption of the chemisorbed TDMAT on the surface sites [98]. But due to the lack of experimental mechanistic studies on the growth of TiO_2 by TDMAT with water and its surface dissociates, this model is not backuped and discussion is still left open to clarify the temperature-dependent increase of the GPC to lower deposition temperatures.

3.2.2 Material Properties of TiO_2

From industrial point of view, the application of TiO_2 thin films for resistive switches requires excellent material quality. High purity and excellent knowledge on the structural properties are desirable. Thus, chemical analysis are needed to ensure low impurity contents. The structural properties are linked to the physical nature of the crystallization. Thus, the morphology and the structure have to be carefully analyzed.

3.2.2.1 Chemical Properties of TiO_2

For ALD, all precursors are of high purity with respect to metal traces. However, modern ALD precursors consist of complex compounds with a variety of possible organic ligands. Reasonably, the building atoms of the ligands can be incorporated as impurities while the ALD growth due to incomplete ALD half reactions or simply thermal decomposition. In amide and mixed-amide based precursors such as TDMAT and TiA_3G_1 reasonably C and N may cause considerable impurities. The impurity content was analyzed by XPS on a XPS 5600 from Physical Electronics after 15 s Ar^+ sputtering time at 4 keV to exclude surface contaminants to be measured. In figure 3.15(a) and 3.15(b) the resulting atomic concentration of C and N are shown dependent on the deposition temperature, respectively. From 100 °C to 300 °C no more than 1 at% N and 3 at% C contamination was found in TiO_2 deposited by the TDMAT process. In TiO_2 grown by TiA_3G_1 and water, the impurity level does not exceed these values up to 330 °C growth temperature.

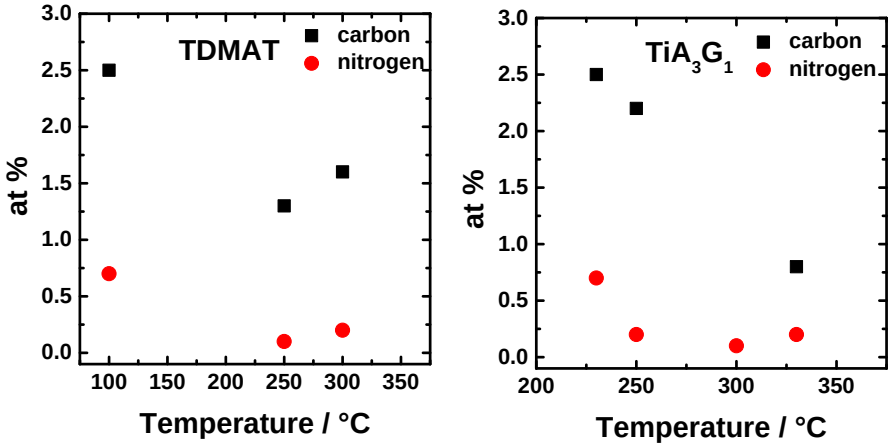

(a) (b)

Figure 3.15: Atomic impurity concentration as a function of the deposition temperature in TiO_2 thin films grown by (a) TDMAT and water and (b) TiA_3G_1 and water.

Especially for resistive switching application, the oxidation state of Ti in titanium oxide is essential. The oxidation state of Ti in the thin films has been also measured by XPS. Ar^+ bombardment sputters O and Ti with different rates. Thus, instead of XPS after sputtering, the measurements were carried out under different angles to ensure that the data qualify the bulk TiO_2 material and not only possible chemical surface states. In figure 3.16(a) a representative XPS spectrum of the Ti2p core levels in a 3 nm thin TiO_2 film grown at 300 °C is shown. Besides the Ti^{+4} binding peaks, an additional peak overlaps to the right shoulder of the $Ti2p^{3/2}$ core level peak. The peak in the shoulder originates from Ti in the Ti^{+3} binding state. This state is also present in TiO_2 thin films of different thickness and temperatures. The integral portion of the Ti^{+3} state on the total signal of the $Ti2p^{3/2}$ core level for all analyzed TiO_2 films was around 5 % as depicted in figure 3.16(b). This clearly proves that the water-based TDMAT process can provide TiO_{2-x} thin films with a certain degree of oxygen deficiency which is desired for ReRAM applications. In contradiction to that, ozone-based TiO_2 ALD processes inhibit oxygen vacancies while the ALD growth [107] which may result from the higher oxidation potential of ozone as compared to water. From this superiority of water-based ALD processes over ozone-based ones with respect to the desired oxygen deficiency in TiO_{2-x} films for ReRAM can be infered.

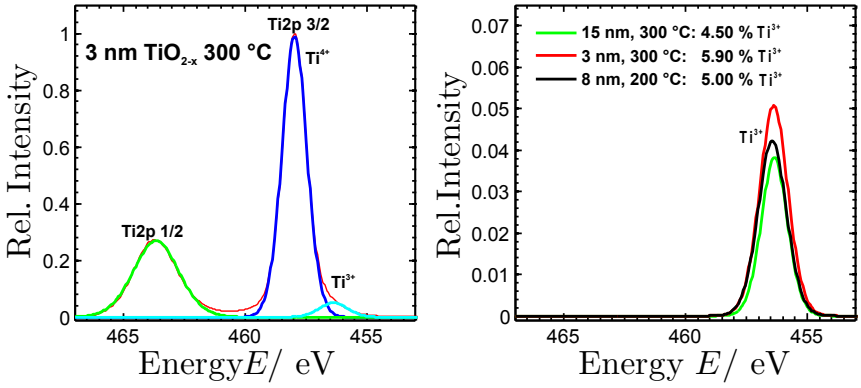

(a) (b)

Figure 3.16: (a) XPS spectra of the surface of a 3 nm thick TiO_{2-x} sample grown at 300 °C. The measurement angle was chosen to 45 ° at a pressure of $1 \cdot 10^{-9}$ Pa. (b) Ti^{3+} signal of TiO_{2-x} grown by TDMAT and water at different temperatures.

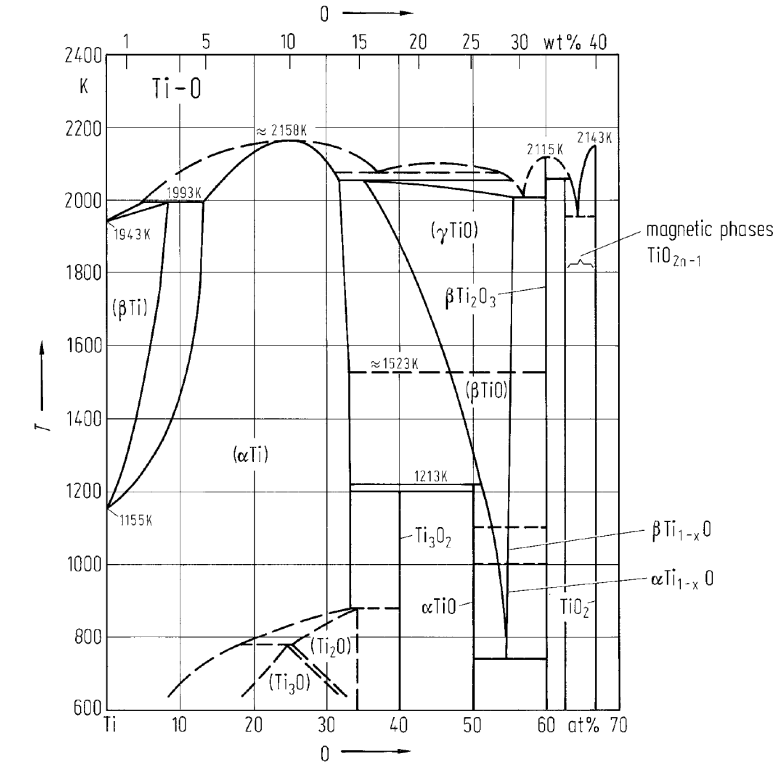

(a)

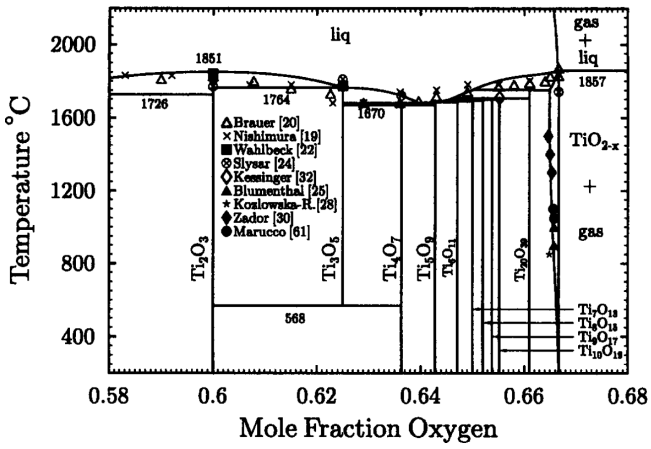

(b)

Figure 3.17: (a) Phase diagram of O-Ti from 0 wt% O to wt% 70 O. (b) Phase diagram as a function of the mole fraction of oxygen from 0.58 to 0.68. Taken from [108, 109] with permission of the authors.

3.2.2.2 Titanium Oxide Phases

The above described amide based precursors undergo oxidation by water while the thermal ALD process. Thus, stochiometric TiO_2 should be expected. Nevertheless, oxidation by water was demonstrated to creates oxygen deficient TiO_{2-x} thin films and the stochiometric Ti^{+4} phases on the right of the O-Ti phase diagram in figure 3.17(a) as well as their suboxides in figure 3.17(b) may arise while the crystallization of TiO_{2-x}. Three stochiometric phases of titanium(IV)-oxide are known under standard conditions. The rutile, the brookite, and the anatase phase as shown in figure 3.18(a) to figure 3.18(c). The rutile structure consists of a body-centered tetragonal unit cell containing 2 TiO_2 groups [110]. Within the rutile structure Ti is six-fold coordinated by O atoms in an octahedron and the oxygen atom are 3-fold trigonal coordinated in planes. These octahedra share two edges with other octahedra within the rutile phase. The unit cell of brookite is orthorhombic arranged and consists of 8 TiO_2 groups. TiO_2 crystallized into brookite phase is built up of distorted octahedra which share 3 edges with other octahedra. In contradiction to brookite, the anatase structure is built up of only 4 TiO_2 in an unit cell [111]. Its Ti atoms are also 6-fold coordinated in octrahedra. The number of 4 shared edges is the highest among the stochiometric titanium oxides. Because of the low number of shared edges the rutile phase is the most stable phase of all three polymorphs with respect to electrostatic repulsion [112]. The lowest stability is found for the anatase phase among all three polymorphs. This is consistent with the decrease of the Gibbs energy of formation from the anatase to the rutile phase [45].

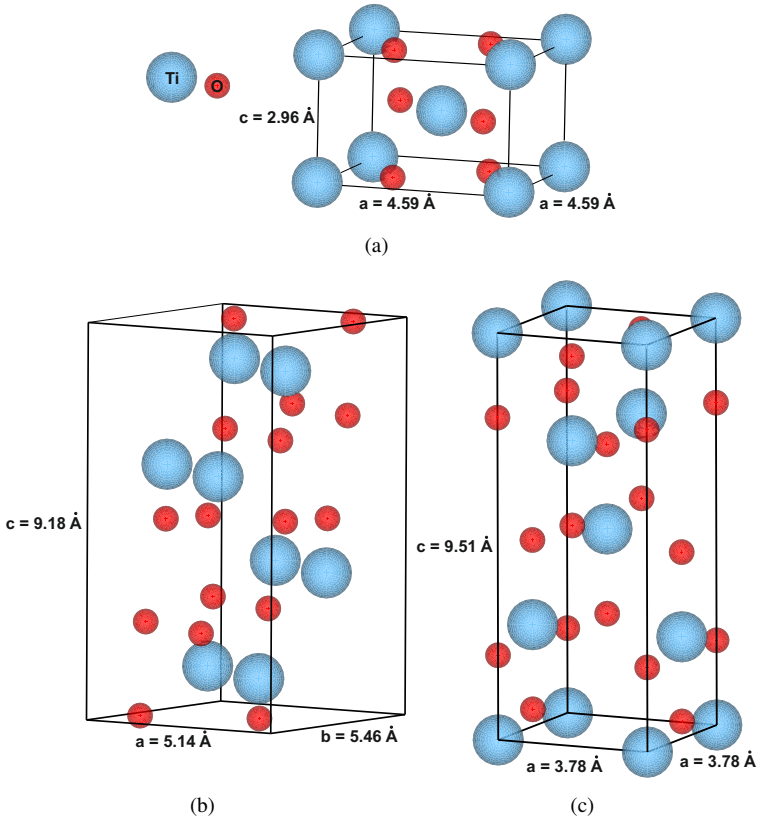

Figure 3.18: Unit cells of the polymorphs of stochiometric TiO_2: Rutile, brookite , and anatase in (a), (b), (c), respectively. Unit cells were drawn by VESTA ©Momma and Izumi using the ICSD database [113].

Stoichiometric titanium(IV)-oxides do practically not exist [109]. The material always contains point defects, Ti interstitials and oxygen vacancies or includes structural defects to accommodate the oxygen deficiency like for example, the Magnéli-phases in the rutile phase. While point defects are of Schottky-type or Frenkel-type disorder and their concentration can vary continuously, the Magnéli-phases follow the empirical formula Ti_nO_{2n-1}. In figure 3.19 the formation of the Magnéli-phase Ti_4O_7 from rutile is exemplary shown. Magnéli-phases are generated by the introduction of oxygen vacancies into the rutile phase. By this, the rutile octahedra (TiO_6) are rearranged into slabs along $(121)_r$ shear planes in case of $4 \leq n \leq 10$. From the hexagonal view of oxygen atoms surrounding the Ti atoms in rutile-type TiO_2 shown in figure 3.19(a), the removal of oxygen atoms results in a rearrangement which is shown in figure 3.19(b). The removal of oxygen forces the rearrangement of the lattice into slabs of Ti atoms in antiphase. The oxygen atoms remain in phase across the $(121)_r$ planes, except some oxygen defects according in number to the empirical formula Ti_4O_7 [114]. Higher numbers of $n \geq 11$

are still Magnéli-phases, but in such phases the orientation of th shear plane changes from [121] to [132] [45]. However, the structure of such Magnéli-phases with lower oxygen deficiency with respect to stoichiometric TiO_2 can be explained in the same manner.

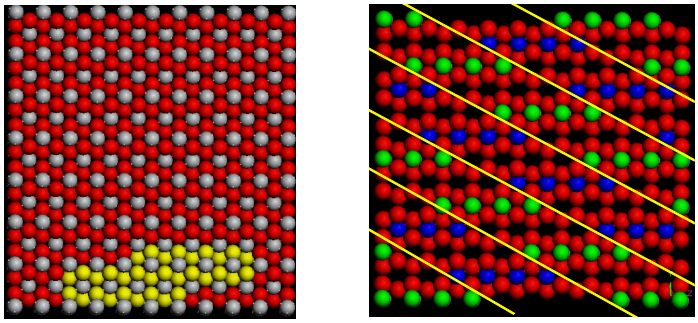

(a) (b)

Figure 3.19: (a) Hexagonal view of the oxygen atoms (yellow balls) in rutile TiO_2. The removal of oxygen atoms from the rutile TiO_2 lead to the Magnéli-phase Ti_4O_7 in (b). The green and blue marked Ti atoms demonstrate that Ti atoms are from slab to slab in antiphase along the $(121)_r$ planes in contradiction to oxygen atoms across the planes. Taken with permission from the authors [115].

The Magnéli-type phases exhibit some interesting properties. All Magnéli-phases as well as some lower suboxides of the formula Ti_nO_{2n-1} exhibit metal to semiconductor or semiconductor to semiconductor transitions at certain temperatures [45, 116, 117]. These transitions were thoroughly investigated by several authors for the range $4 \leq n \leq 9$ [118, 119]. Among these Magnéli-phases, Ti_4O_7 shows metallic conductivity at room temperature while Magnéli-phases with $5 \leq n \leq 9$ exhibit slightly semiconducting behavior. In Ti_4O_7, the transition was reported to be due to a rearrangement of the mixed Ti^{3+}/Ti^{4+} sites to alternating Ti-Ti pairs perpendicular to the shear planes. Tunneling as well as thermally excited transport was suggested to be responsible for the electronic conductivity [120]. But no unified transport model was found since the electrical conductance does not show any systematic behavior which corresponds to the structural properties of the respective Magnéli-phases.
However, with respect to the ALD growth further consideration of the thermal stability of such phases are desired. While ALD growth, the surface changes by crystallization from the amorphous state to crystalline facets. Therefore, crystallization may influence the growth kinetics on the surface and reasonably change the incorporation of oxygen vacancies. Moreover, inherent crystallization or phase transformation within already grown highly disordered TiO_{2-x} might give rise to a variety of possible scenarios for the creation of suboxides with different oxygen deficiency. This allows to infer that Magnéli-phases with certain oxygen deficiency could be deposited by ALD and might only coexist with oxygen vacancies in the rutile phase. The question arises, which aggregation such a system would thermodynamically prefer: the rutile phase with a continuous oxygen vacancy concentration or a defect rich rutile phase containing

Magnéli-phase crystallites. Liborio et al. calculated the stability of Magnéli-phases as well as point defects by first principle methods [114]. Their calculations revealed, that the formation energies of Magnéli-phases are lower than of oxygen vacancies for low chemical oxygen potential under the given stoichiometric rule Ti_nO_{2n-1}. A low chemical potential corresponds to high temperatures or low oxygen partial pressures. Reasonably, ALD growth under high temperature, utilizing low oxidation potential counter-reactants, and low oxygen partial pressure such as processing under reducing atmosphere should thermodynamically generate Magnéli-phases in the presence of a highly oxygen deficient rutile phase. Furthermore, the simulation by Liborio demonstrated, that different Magnéli-phases can coexist at intermediate oxygen deficiency, for example Ti_4O_7 and Ti_5O_9.
Along the homologous series Ti_nO_{2n-1} also lower suboxides exist. These are Ti_3O_5 which is of monoclinic structure [121, 122] and Ti_2O_3 which crystallizes into corundum structure [123] as shown in figure 3.20. Podshivalova and Karpov analysed the thermodynamic stability in the range from stoichiometric TiO_2 to Ti_2O_3. Their results clearly reveal that the stability continuously increases from Ti_2O_3 to TiO_2 in the presence of water. As a consequence, the probability that the suboxides Ti_2O_3 and Ti_3O_5 could be grown by water-based thermal ALD is much more lower as compared for the Magnéli-phases.

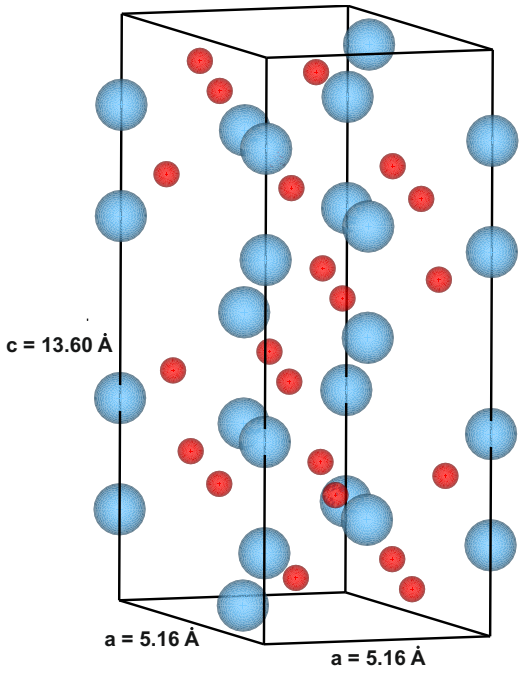

Figure 3.20: Unit cell of stable Ti_2O_3 of corundum structure.

3.2.2.3 Structure of TiO_2 grown by ALD

The TiO_{2-x} thin films grown by TTIP and water were analyzed by means of GIXRD on a X'Pert MRD from Panalytical as shown in figure 3.21. The XRD pattern reveal no crystalline phase up to temperatures of 240 °C at 300 deposition cycles. Above 240 °C, a XRD reflection at 25.4 ° appears which increases in intensity rapidly with increasing deposition temperature. No other peaks were observed within the range from 15 ° to 35 ° 2θ. Thus, purely deposition of amorphous TiO_{2-x} or anatase structured TiO_{2-x} can be concluded at given process condition and ALD cycle time, here to be denoted 37.5 s. The amount of TiO_{2-x} increases non-linear since the growth rate of the TTIP/H_2O process also increases with the temperature. This does not allow to further derive any conclusion about thickness dependent crystallization while the ALD growth of TiO_{2-x}. However, the number was kept above the critical cycle number where crystallization occurs [94].

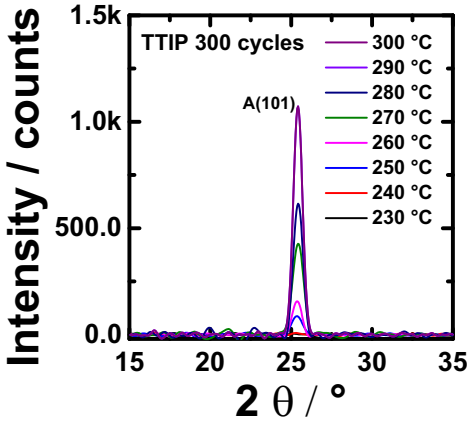

Figure 3.21: GIXRD spectra of TiO_{2-x} deposited by TTIP and water grown at a deposition temperature from 230 °C to 300 °C at 300 deposition cycles.

TiO_{2-x} thin films deposited by TDMAT as well as TiA_3G_1 were further thoroughly investigated with respect to the deposition temperature as well as the thin film thickness. GIXRD spectra in figure 3.22(a) reveal that no XRD reflections could be observed up to 200 °C deposition temperature from TiO_{2-x} films grown by TDMAT and water. Therefore, TiO_{2-x} thin films grown at ≤ 200 °C were considered as amorphous. At 250 °C, two peaks developed with increasing deposition cycle number. The first reflex can be observed at 25.4 °, the second at 30.8 ° with lower signal strength. The second peak identifies clearly the brookite B(121) reflection [124]. The first peak possibly matches the anatase or the brookite phase. From the diffraction data base file of brookite the relative intensity $I(30.8°)/I(25.4°) = 0.9$ can be calculated. But the experimentally derived intensity ratio is only ~ 0.1. This allows to infer that the reflection at 25.4 ° is mainly attributed to the anatase phase. TiO_{2-x} grown by TDMAT and water exhibit the

same onset temperature of crystallization into the anatase phase as compared to TTIP-derived TiO_{2-x}.

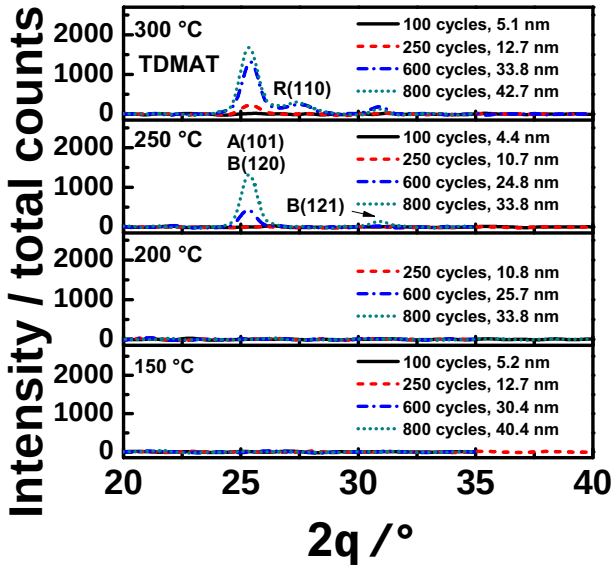

(a)

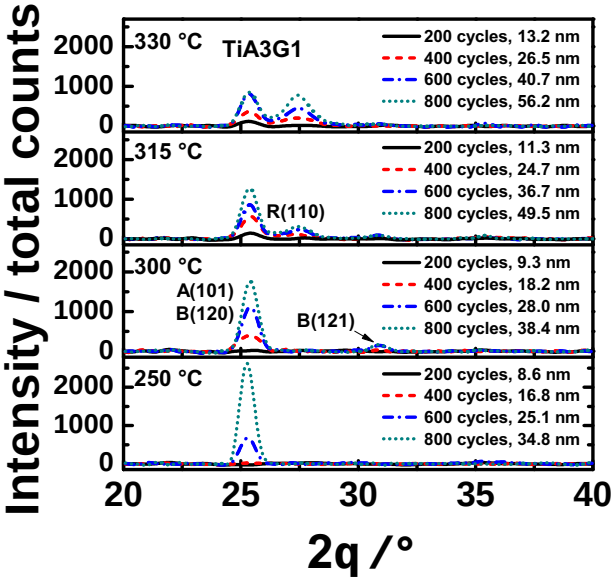

(b)

Figure 3.22: GIXRD spectra of TiO_{2-x} deposited by TDMAT and water in (a) and TiA_3G_1 and water in (b) as a function of the deposition thickness as well as the deposition temperature.

In literature, other reports on the same onset temperature [72, 96], but also lower onset temperatures for the crystallization into the anatase phase were found, between 180 °C up to 250 °C. Such far-flung deviations of the critical crystallization temperature could be caused by a shift of the critical crystallization thickness or by the impact of different type of substrates on the nucleation [125, 126]. Also, dust particles could act as nucleation sites. TiO_{2-x} deposited by TDMAT at 300 °C also contains the brookite phase, but the intensity ratio $I(30.8°)/I(25.4°)$ was decreased. From that, a domination of anatase grown crystallites in size or number over brookite crystallites could be inferred. Another explanation for this behavior can be derived from thermodynamical reasons: the brookite phase might be reduced in favor of the growth of rutile crystallites which could be detected at higher deposition cycle numbers at 300 °C growth temperature. Whatever causes the relative decrease in the intensity ratio, the growth of the brookite phase is limited to a very small temperature window above a certain thickness. However, the brookite phase is a rare form of stoichiometric TiO_2 and therefore a second analysis method was needed to confirm its presence. For that purpose Raman spectroscopy was utilized on a Renishaw inVia Raman microscope. In figure 3.23(a) the μ-Raman measurements on a 43 nm thick (800 cycles) TiO_{2-x} film on a Pt substrate exhibit anatase as well as brookite stokes shift lines. A small rutile peak can be also observed in the spectra. By the μ-Raman method brookite was also found in a 34 nm thick TiO_{2-x} sample deposited at 300 °C. This was not observed by GIXRD. However, the detection by x-rays is limited to ~ 5 nm crystallites in diameter. In contradiction to GIXRD, Raman spectroscopy is not based on diffraction. It enables detection of crystallites of any size because only enough material and high Laser intensities are needed.

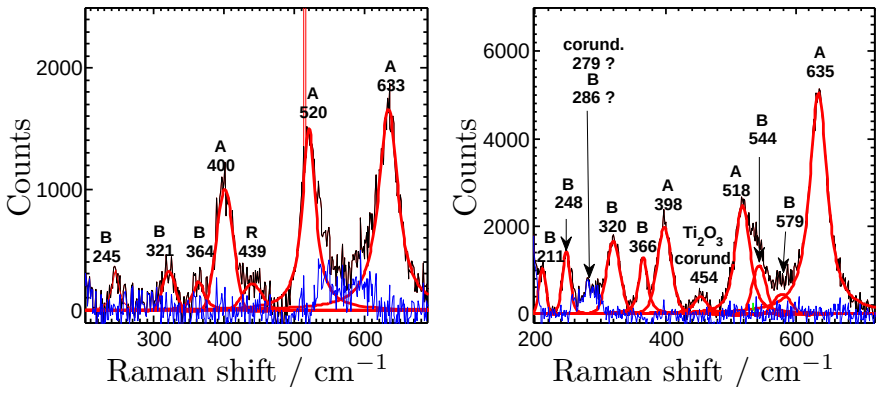

Figure 3.23: Raman spectra of TiO_{2-x} samples grown by TDMAT and water at a temperature of 250 °C and 300 °C in (a) and (b), respectively.

Most interestingly, Raman spectroscopy of TiO_{2-x} grown at 300 °C reveal the existence of a certain amount of Ti_2O_3 of corundum phase. As discussed before, such phases are thermodynamically less probable than phases of higher oxidation state [127]. In addition to that, the rutile phase was grown at this deposition temperature which can be be transformed into

Magnéli-phases. As already stated in section 3.2.2.2, the growth of the Magnéli-phases thermodynamically are more probable as compared to the growth of Ti_2O_3. Thus, the presence of Ti_2O_3 is an indirect proof of the existence of Magnéli-phases in thick TiO_{2-x} films grown by TDMAT and water. Ti_9O_{17} has been directly detected within TiO_{2-x} grown by TiI_4 and H_2O_2 within a deposition temperature range a little above 300 °C [128]. This gives further evidence, that TiO_{2-x} films can be grown by water-based thermal ALD since the water oxidation potential is lower than of H_2O_2. Unfortunately, Magnéli-phases are well-conducting suboxides of TiO_2 and reasonably cannot be directly measured by Raman spectroscopy at room temperature [129]. From the view of ALD, the rutile phase on non-structural matching substrates at only 300 °C deposition temperature is remarkable. The nucleation of the rutile crystallites of TiO_2 can be initiated by the choice of substrate with rutile structure [130]. Others report on the deposition of the rutile phase on Si(100) at a deposition temperature of 350 °C [126].
Since TiO_{2-x} grown by TDMAT and water at 200 °C does not exhibit any detectable crystallites, the structural analysis by GIXRD on TiA_3G_1-derived TiO_{2-x} was carried out from 250 °C to 330 °C as depicted in figure 3.22(b). At 250 °C growth temperature, only the anatase phase could be observed. Interestingly, the XRD reflexes at 25.4 ° exhibit a much higher intensity as compared to TiO_{2-x} films derived by the TDMAT/H_2O process. Higher deposition temperatures lead to a decrease of the intensity of the anatase A(101) reflection and the brookite phase starts to develop at 300 °C and nearly vanishes at 330 °C. In addition to that, rutile crystallites with the orientation R(110) could be found at 315 °C. The development of rutile crystallites in TiO_{2-x} grown by TiA_3G_1 and water seems to be somehow retarded as compared to the TDMAT process with regard to the deposition temperature. Finally, the GIXRD spectra at 330 °C reveal that the rutile reflection peak nearly reaches the level of the anatase reflections at higher deposition thicknesses.

3.2.2.4 Morphology of TiO_2 grown by ALD

The structural investigation by GIXRD and μ-Raman spectroscopy revealed that different deposition parameters like temperature, thickness and process time have an impact on the composition and the crystalline structure. Thus, the surface morphology was scanned by non-contact AFM for all LI-ALD grown TiO_{2-x} films grown on smooth SiO_2|Si(100) substrates.
In figure 3.24 the topographic evolution of TiO_{2-x} crystallites grown by TTIP and water are shown. Crystallites of quadratic pyramid-like shape of anatase phase [73] were found from beginning of the crystallization at 240 °C. These objects grow laterally and in height as a function of the deposition temperature from 250 °C to 290 °C depicted in figure 3.24(b) to 3.24(f). Reasonably, the RMS roughness rapidly increases to ~ 8 nm in figure 3.24(g). In nanotechnology crystallization into such large objects has to be generally avoided and disqualifies the TTIP/H_2O process for the integration of TiO_2 into ReRAM at such high growth temperatures.
The topography of TiO_{2-x} thin films grown by TDMAT and water shown in figure 3.25 generally exhibit much more smaller surface objects as compared to the TTIP process. At 250 °C, crystallization into medium sized objects can be observed with increasing thickness, see figure 3.25(a) to 3.25(c). The grown crystallites within the amorphous matrix appear as pyramid-shaped ob-

jects overlayed by other objects as compared to purely anatase grown crystallites by the TTIP process. This may result from concurring growth between crystallites of anatase and brookite structure. An increase of the growth temperature to 300 °C as depicted from figure 3.25(d) to 3.25(f) forces the growth of small crystallites at already low deposition cycle numbers. This is in good agreement with the found anatase phase at early stages of ALD growth.
The AFM images of the samples prepared by TiA_3G_1 from 250 °C to 330 °C are arranged in figure 3.26 in the same manner like the images of the TDMAT-derived samples. The 250 °C series reveal the evolution of crystallites similar to the respective TDMAT series, but they are larger in size and correspond in shape better to the purely anatase structured TiO_{2-x} films grown by the TTIP process. This is also backuped by the structural information in the previous section. However, the AFM images reveal smaller grains which superimpose the large crystallites, but no other phase was found in the corresponding GIXRD spectra. This may results from the detection limit of GIXRD. In the case of the TiA_3G_1 process, higher deposition temperatures lead again to the refinement of the topography similar to TiO_{2-x} thin films grown by TDMAT. At 330 °C even much more smaller grains can be achieved as shown from figure 3.26(f) to 3.26(g). TiO_{2-x} grown by TTIP demonstrated enormous roughening by largely grown anatase-type crystallites. For TiO_{2-x} grown by TDMAT and TiA_3G_1 the topography is improved due to smaller grains. Smaller grains are generally expected to contribute less to thin films roughening demonstrated by TTIP-derived TiO_{2-x} thin films. Reasonably, lower RMS roughness was estimated for TiO_{2-x} thin films deposited by TDMAT and TiA_3G_1 as shown in figure 3.27. Due to the structural refinement, samples with small crystallites exhibit linear dependence of the RMS roughness on the ALD cycle number (thickness). Amorphous grown TiO_{2-x} does only reproduce the surface of the substrate due to the self-limited growth mode. Therefore, the RMS roughness does not increase with thickness. In the intermediate temperature regime the crystallization from an amorphous host material occurs. Thus, the RMS roughness increases only at high cycle numbers. However, the statistical analysis of the topography clearly demonstrates that the roughnesses does not exceed 3.5 nm for the TDMAT and TiA_3G_1 process. This ensures high quality TiO_{2-x} thin films for resistive switching applications.
The GIXRD spectra and the AFM topography demonstrated, that TiO_{2-x} films crystallize at a certain thickness. Nevertheless, very small crystallites cannot be detected either by XRD at given x-ray wavelength nor may not show any considerable topographic information by AFM. HRTEM enables to take a look onto more details in very thin layers. Figure 3.28 shows HRTEM images of TiO_{2-x} films deposited by TDMAT and water at different temperatures and thicknesses cut into lamellae. 3 nm thin TiO_{2-x} films grown at 200 °C and 300 °C were obviously grown in the amorphous state since no regular pattern could be observed. In 8 nm thick TiO_{2-x}, 300 °C deposition temperature already leads to closed polycrystalline TiO_{2-x} thin films with crystallites in size below 10 nm. This agrees well the found dot-like topographic features by AFM at similar thickness on SiO_2. The critical thickness at which crystallization of TiO_2 occurs were reported to appear at different thicknesses dependent on the temperature. HRTEM investigation on TiO_2 grown by TTIP and water reveal a critical thickness ranging around 12 nm at 250 °C deposition temperature [96], while at 365 °C deposition temperature TiO_2 grown by $Ti(O{-}i{-}Pr)_2(DPM)_2$ and water already cause a crystallization at only 5 nm thickness [131]. At such high deposition

temperatures the very low RMS roughness is also attributed to the crystallization at initial stages of growth. However, the ALD growth experiments in this work demonstrated the complexity of crystallization while utilizing different ALD processes on the same ALD reactor system.

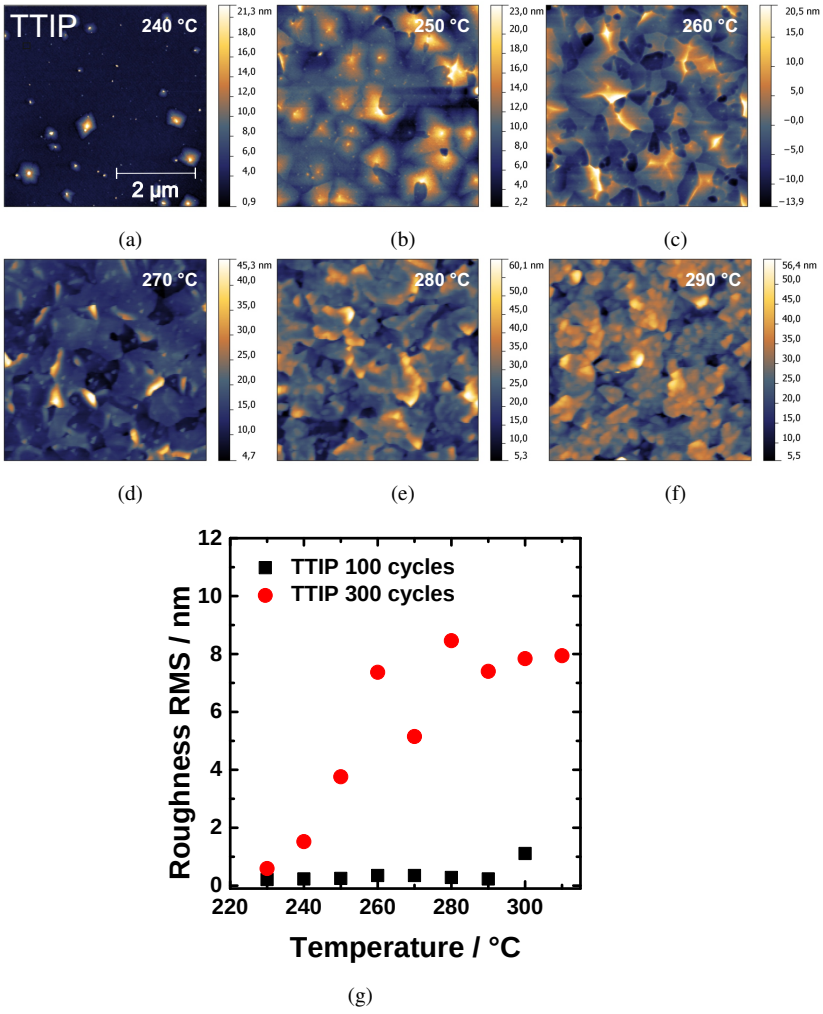

(a) (b) (c)

(d) (e) (f)

(g)

Figure 3.24: AFM images of TiO_{2-x} on SiO_2 grown by TTIP and water. Figures (a) to (f) show the evolution of the growth of crystalline objects with increasing deposition temperature until the crystalline surface is fully closed. The deposition cycle number was fixed to 300 in this experimental series. In (g) the influence of the temperature on the RMS roughness is depicted for two distinct deposition cycle numbers.

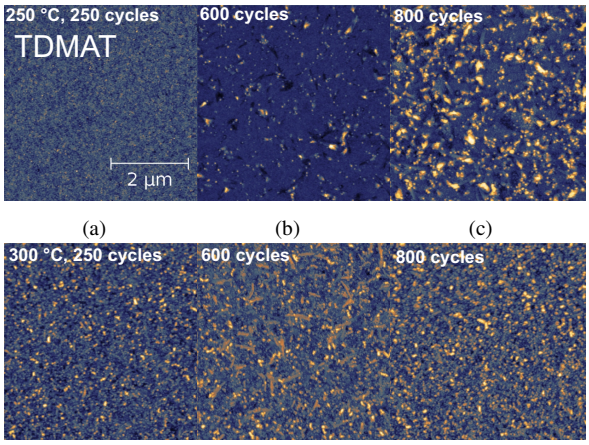

Figure 3.25: AFM images of TiO_{2-x} on SiO_2 grown by TDMAT and water. Figures 3.25(a) to 3.25(c) show the increase in the density of surface objects on TiO_{2-x} films grown at 250 °C as a function of the ALD cycle number. Figures 3.25(d) to 3.25(f) show the corresponding AFM images for 300 °C revealing smaller objects.

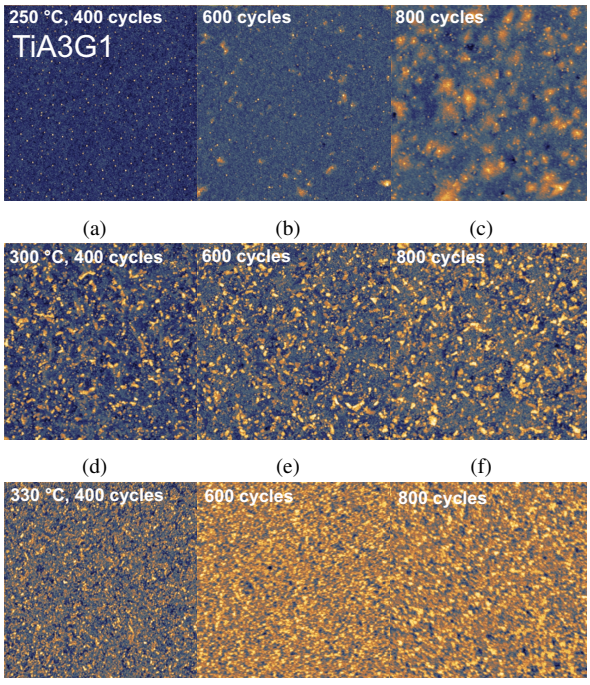

Figure 3.26: AFM images of TiO_{2-x} grown by TiA_3G_1 and water at various ALD cycles from left to right and deposition temperatures from top to bottom. SiO_2|Si was used as substrate material. For 250 °C in figures 3.26(a) to 3.26(c) the development of rectangular grains was observed with increasing cycle number. From figures 3.26(d) to 3.26(g) the surface morphology was refined to small grains with increasing temperature.

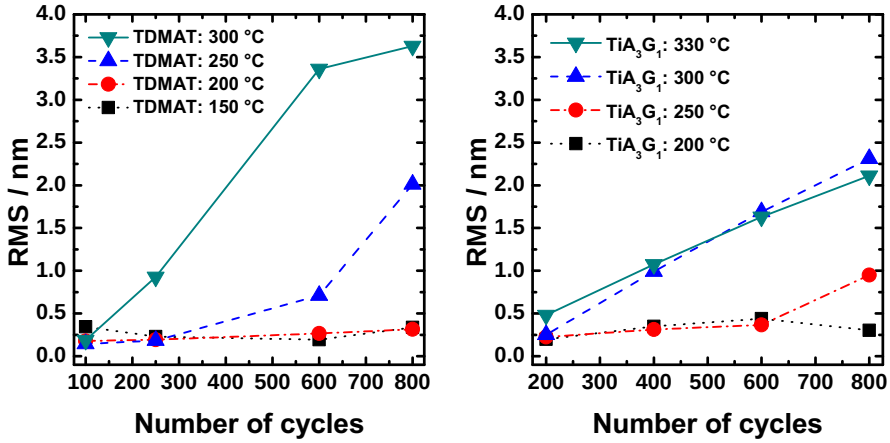

(a) (b)

Figure 3.27: RMS roughness of TiO_{2-x} thin films by TDMAT and H_2O in (a) and by TiA_3G_1 and H_2O (b)

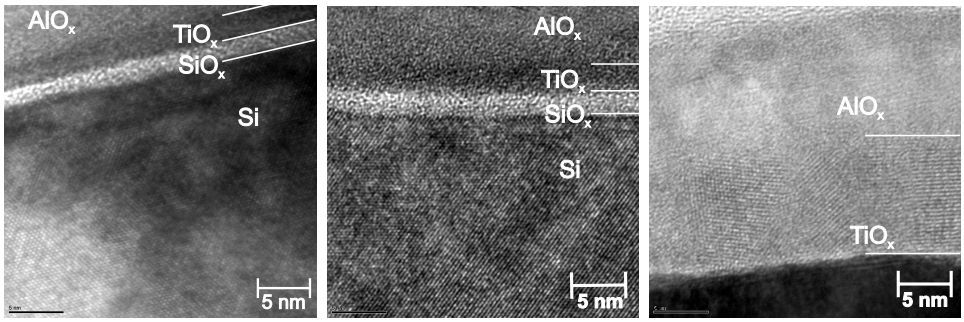

(a) (b) (c)

Figure 3.28: HRTEM images of 3 nm thin amorphous TiO_{2-x} films on Si(100) substrate grown at 200 °C and 300 °C in (a) and (b), respectively. In (c) a 8 nm thick TiO_{2-x} grown at 300 °C on Pt is already crystallized.

3.2.2.5 Crystallization Behavior

In this thesis, the ALD growth experiments demonstrated that crystallization does not only depend on thickness and temperature. Thin films grown by TTIP lead to crystallization at early stages of growth while the time optimized TDMAT as well as TiA_3G_1 processes changes the situation. From this point of view the most apparent difference of all processes is the ALD cycle time. The TTIP/H_2O process takes ~ 37.5 s, the TiA_3G_1 /H_2O process 21.75 s, and the

TDMAT/H_2O process only 19.5 s. At 250 °C, all processes show the development of the anatase phase, clearly indicated by the development of the A(101) reflection in the GIXRD spectra and the pyramid-like crystallites growing in the amorphous TiO_2 matrix. To explain this behavior the crystallization kinetic has to be considered. Under isothermal condition, the crystallization is generally described by the Johnson-Mehl-Avrami-Kolmogorov equation [132, 133]. In this equation, the fraction of material which undergoes a phase transition is proportional to the time. Reasonably, the crystallization condition changes with ALD cycle time. Exemplary switching from the TDMAT to the TiA_3G_1 process, an ALD cycle time difference of only 2.25 s causes a total difference in time of 30 min at 800 ALD cycles. As a consequence, the growth of large crystallites is favored for the TiA_3G_1 process. This is mostly apparent from the comparison from thin films grown by TTIP and TiA_3G_1 at 250 °C . 20 nm TiO_{2-x} thin films derived by the TTIP process already exhibit a surface which is close by large crystallites. In contradiction to that, the TiA_3G_1 crystallites of the same shape in ~ 34 nm thick TiO_{2-x} are much more smaller. From all TiO_2 phases, the anatase phase is preferably grown at large time scales. This is because enough time is given to laterally grow large anatase crystallites from the amorphous surrounding or other competitively developing crystallites of different phase are faster swallowed up by the anatase crystallites under such thermodynamical boundary conditions. Crystallization also depends on the Avrami rate. It describes how fast a crystallite grows from an initial nuclei depending on the free energy of transformation of the undercooled liquid [134], here the amorphous TiO_{2-x}, to a crystalline phase. The free energy has to be different for the rearrangement from the amorphous state to each crystalline structure since each phase represents its own thermodynamical state at given boundary conditions, for example temperature. By this, the preferential growth of the rutile and brookite phases at given temperature and process time can be explained, additionally.

3.2.2.6 Influence of the Crystallinity on the Growth

Both fast processes, TiA_3G_1 /H_2O and TDMAT/H_2O do not exhibit any cycle-dependent transition to higher growth rates at a certain thickness as compared to the slow TTIP/H_2O process. As mentioned before, the TTIP process favored the growth of large anatase crystallites with clearly visible facets and exhibited the growth rate transition assigned to an enhanced hydroxylic density on the anatase crystallites [94]. As a consequence, any ALD process condition which decreases the amount of large crystallites and their size, or decrease the total fraction of TiO_2 crystallized into the anatase phase, will suppress the growth transition [73]. Hence, this model allows to conclude, that by changing the ALD process time the growth transition can be inhibited. Vice versa, extending the process time of the TiA_3G_1 or TDMAT process to the time scale of the TTIP process should enable the observation of a cycle-dependent growth transition. To prevent any influence on the chemisorption of the precursor or its thermal decomposition on the surface while the growth, this can be simply done by extending the water purge time. In figure 3.29(a) the results of the corresponding cycle-dependent experiment on the TDMAT process for two distinct ALD cycle times at 260 °C deposition temperature is depicted. At 19.5 s process time, the slope of the Ti mass layer density vs cycle number does not show any change, but the extension of the ALD cycle time to 37.5 s caused a kink of the slope as pre-

dicted. Finally, to verify that the anatase phase causes the transition, selected samples from both experimental series were analyzed by means of GIXRD shown in figure 3.29(b). At long process time, the spectra clearly confirm that only the anatase phase developed and the enormously increased signal strength of the A(101) peak reveal large crystallites are grown as compared to short process time according to the Scherrer equation [135]. In this experiment, the growth rate was increased by a factor of 1.4 while the TTIP process lead to an increase of the growth rate of about a factor 2. In literature, different transition factors were reported for the growth of TiO_2 on different types of substrates [96] and for other precursor systems with water as counter-reactant [136]. Especially the difference in the factor by distinct precursor systems is of importance. This evidences the modulation of the surface chemistry by the structural properties in case of TiO_2 growth utilizing water as oxygen source. In which order the ALD chemistry might additionally attribute to the crystallization of an amorphous film or might induce phase to phase transformations is questionable because usually reaction energies range around 1 eV and takes only place on the surface in the ALD limited manner. Hence, the exothermic reaction energy of maximum one surface layer has to be high enough to initiate nucleation from the amorphous state throughout the whole film.

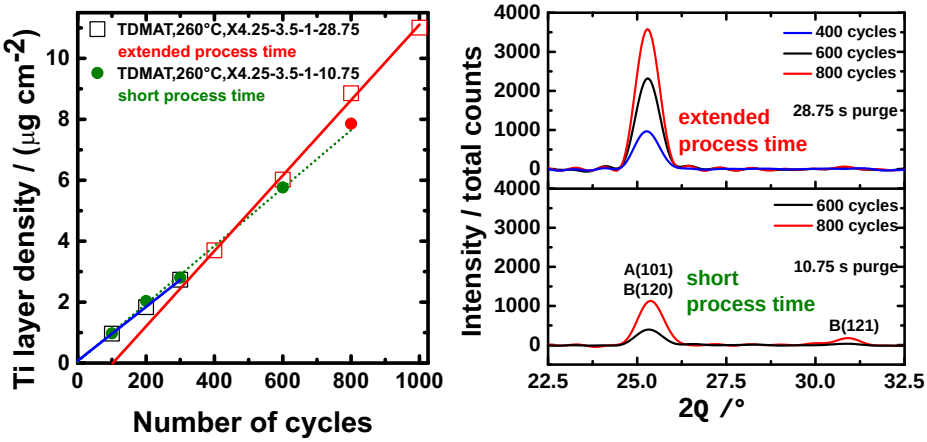

(a) (b)

Figure 3.29: (a) Growth of TiO_{2-x} by TDMAT and water at short standard process time and extended process time. (b) Corresponding GIXRD spectra to the experiment of selected TiO_{2-x} samples grown on SiO_2.

3.2.2.7 Dielectric Properties of TiO_{2-x}

Besides the structural properties, also optical properties of the derived TiO_{2-x} thin films are of interest. The integration of TiO_{2-x} in asymmetric ReRAM with regard to the electrodes' may cause a Schottky barrier. Therefore, the static dielectric permittivity of TiO_{2-x} thin films integrated into ReRAM is of major interest. The optical properties of amorphous and nano-crystalline TiO_{2-x} films grown by TDMAT and water were analyzed by means of ellipsometry. In figure 3.30(a) the derived real part of the dielectric permittivity is shown as a function of the photon energy. Amorphous TiO_{2-x} exhibits at its resonance energy (frequency) a dielectric permittivity of around 12.5 whereas the maximum permittivity of nano-crystalline TiO_{2-x} is a little higher about 15. In both cases, the static dielectric permittivity can be extrapolated to around 5 . Vos and Krusemeyer report the maximum dielectric permittivity of about 15 and 22.5 for single crystal rutile orientated perpendicular and parallel to its c-axis, respectively [137]. Although their measurements were not carried out down to 1 eV, the value of the dielectric permittivity $\sim 8\perp$ c-axis at 3 eV is in agreement with the present work results. Moreover, the determined absorption coefficient allows to estimate the band gaps for the different material. According to Tauc's empiric law $(\alpha h\nu)^{1/2} \propto (E_g - h\nu)$ the band gap of the amorphous TiO_{2-x} can be extrapolated to 3.35 ± 0.01 eV by the slope in figure 3.30(b) extrapolated to zero. A very close value of 3.33 eV was found for amorphous TiO_2 by Aarik et al. [138]. For crystalline materials, indirect and direct band gaps may occur. The Tauc plot for nano-crystalline TiO_{2-x} in figure 3.30(b) reveal a large slope which corresponds to an indirect band gap of 3.33 ± 0.02 eV, a second smaller slope results in a band gap of 2.72 ± 0.03 eV. For the anatase phase band gaps from 3.20 eV to 3.26 eV were determined in TiO_2 grown by a variety of thin film deposition methods [139, 138, 140]. To the authors best knowledge, only one publication in literature exists which reports on an indirect band gap of 2.8 eV in rutile TiO_2. Other studies claim indirect band gaps from 2.95 eV to 3.05 eV by ab-initio methods as well as by optical measurements [139, 141]. Interestingly, the smaller band gap of only 2.8 eV was found in mixture of anatase and rutile nano-crystallites. The AFM scans in section 3.2.2.4 also reveal nano-sized crystallites which may exist in the rutile phase beside crystallites of anatase phase. Hence, the two determined band gaps are reasonable for the grown nano-crystalline TiO_{2-x} films. In figure 3.30(c) the $(\alpha h\nu)^2$ vs $h\nu$ plot clearly shows a direct band gap of 3.86 ± 0.02 eV. This value matches well the two photon absorption process in rutile TiO_2 reported by Waff et. al [142]. The two photon absorption process allows to infer a direct band gap of 3.75 ± 0.08 eV linked to the existence of an exciton. Hardman et al. [143] investigated single rutile crystals by angle resolved photoemission spectroscopy utilizing a synchrotron source. Their measurements show an band gap of around 4 eV which supports the existence of the exciton. In a recent DFT study, the band gap of such quasiparticles was calculated to 3.73 eV [144].

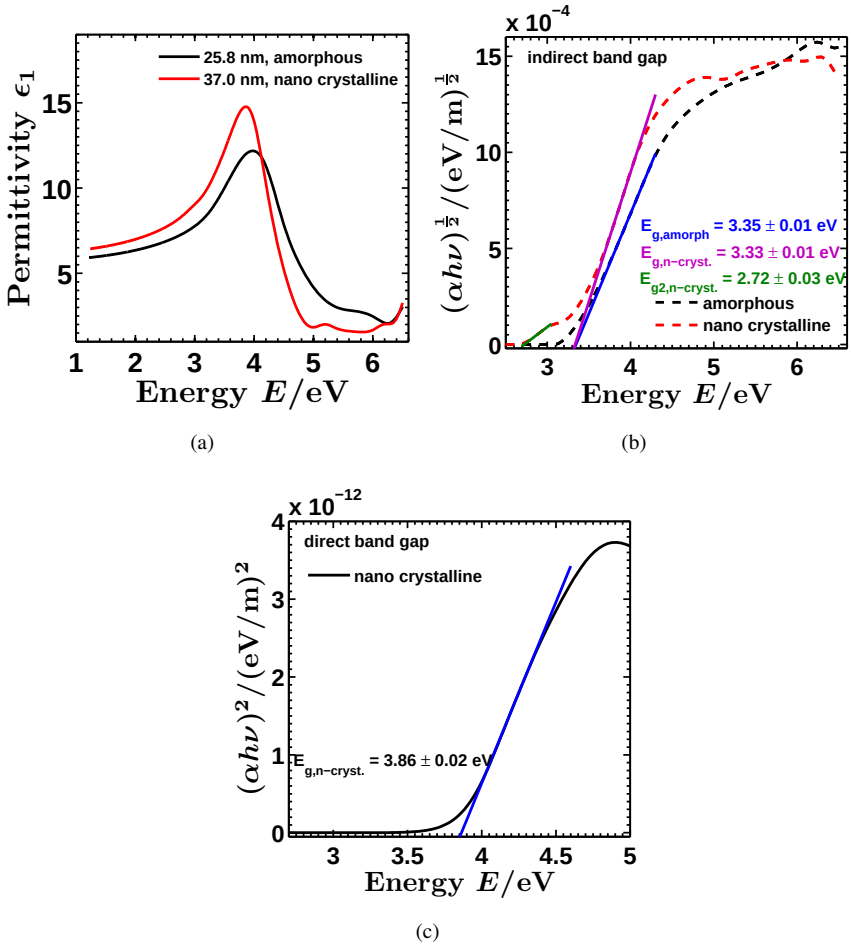

Figure 3.30: (a) Measurement of the dielectric permittivity as a function of the excitation energy. (b) Tauc plot for the determination of the indirect band gap in crystalline TiO_{2-x} and the band gap of amorphous TiO_{2-x}. (c) Determination of the direct band gap in nano crystalline TiO_{2-x}.

CHAPTER

FOUR

FABRICATION OF CROSS-POINT RERAM

This chapter addresses the fabrication of nano cross-point ReRAM. In the first part the utilized wafer structuring and electrode deposition methods will be depicted. The second part is dedicated to the full device process flow of standard nano cross-point devices as well as the changed device preparation route for forming-free devices. Afterward, the chapter closes with an overview over the produced sample series are given with respect to the experimental goals.

4.1 Lithography

In contradiction to simple shadow mask prepared MIM structures, the fabrication of nano cross-point devices need complex patterning methods to create nano-dimensioned lines and electrical contact-pads. For that purpose different kind of appropriate lithography methods are needed.

4.1.1 UV Light Lithography

UV light lithography (UVL) is the most prominent method for transferring patterns onto planar wafers. Its success mirrors the simplicity and repetition of micro- and nano patterning by exposure of UV light through a pattern mask onto the resist layer. The critical dimension (CD) and quality of pattern transfer is mainly determined by the wavelength λ of the used light source, the applied resist (k-factor), and the numeric aperture NA.

$$CD = k \cdot \frac{\lambda}{NA}$$

Of course, the semiconductor industry strives to achieve resolution as high as possible. Reasonably, the next generation UV light sources will have 13.5 nm wavelength [3]. Nevertheless, higher wavelength such as 365 nm of the Hg i-line enable a minimum feature size of around 1 μm which are sufficiently small enough to prepare for example opening windows. In re-

search, such low resolution systems are usually operated in contact or proximity mode for small batches as shown in figure 4.1(a). But these are not employed in mass production because of low throughput and mask damage by direct contact.
The basic principle of UVL is the change of the chemical properties of a resist. Such a resist consists of a polymer or resin with additional photo active substances dissolved in a neutral organic liquid. The resists show different UV light sensitive properties. Polymers usually are cracked by energy-rich UV light and can be used for photo-positive patterning. This corresponds the scheme in figure 4.1(b) from (1) to (2). Negative patterning is achieved by resists which behaves oppositely with respect to the photo-reaction or by reverse processing. After initial exposure, reverse UVL processes are initiated by reversal baking and subsequent flood exposure as shown in figure 4.1(b) from (3) to (4). By this, the prior exposed area is not soluable but the complementary area can be faster developed.

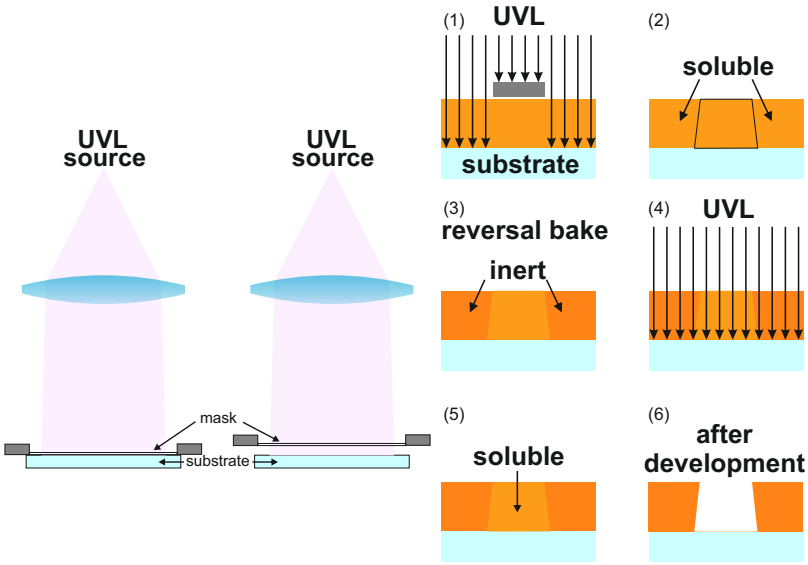

Figure 4.1: (a) Illustration of different contact modes in UVL. (b) Full scheme of reverse UVL process. (1) to (2) equals positive UVL process. From (3) to (6) reversal process steps.

4.1.2 E-beam Lithography

A direct method to transfer patterns onto a substrate is the electron beam Lithography (EBL). Instead of transfering patterns from a mask to the substrate a focused electron beam is used to actively write patterns into a polymer resist. The setup of an e-beam writing machine is depicted in figure 4.2. Similarily to a scanning electron microscop the EBL uses electron optics consist-

ing of an e-beam source, a condensor, and a aperture lens to generate a focused electron beam with corrected astigmatism. Within this electron optics a beam blanker is deployed to attenuate the electron beam from bright to zero incidence. A second additional part is a deflector which is crucial to control the scan direction over the substrate by the electron beam.
The resolution of this method is practically not limited by the wavelength due to the wave-particle duality. Electrons accelerated in a vacuum chamber have a very small corresponding wavelength of a few pm if acceleration voltages in the kV regime are applied. But the resolution of EBL is limited by other factors. The most striking factor is caused by the electrons themselves. If electrons cross matter, they undergo forward and backward scattering. All electrons which scatter forward widen the focused electron beam within the resist, and as a consequence, the resolution decreases. Scattering in backward direction may raise exposure of the whole substrate. As a consequence, the resist as well as the substrate beneath have an impact on the resolution. Structuring resist by electrons need a high writing dose which makes EBL time consuming if very small structures are desired. Typically, such a tool is not useful for commercial applications, but in research test nanostructures do not require to cover the whole wafer. So blank areas do not have to be written.

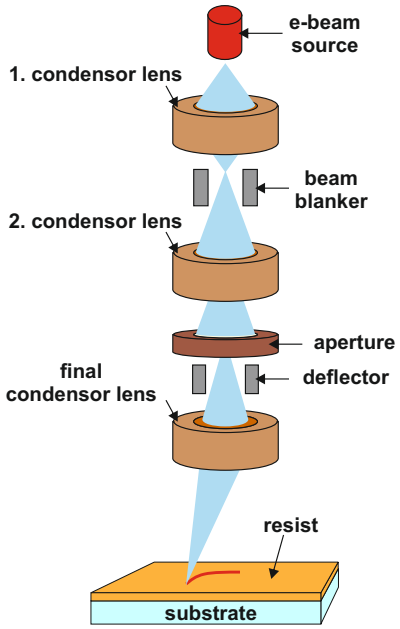

Figure 4.2: Schematically drawing of an e-beam writer.

4.1.3 Nano Imprint Lithography

Since EBL is too time-consuming and expensive for mass production, and the aboriginal cost for complex extreme UVL hinder the deployment in small batch production, nano imprint lithography (NIL) represents a method to bridge the gap between EBL and UVL to achieve sub-10 nm nanostructures [145]. Basically, utilizing NIL comprises the simple idea that a mold pressed into a thin polymer resist transfers an negative image of the mold's topography. By this, the resist starts to flow away from high patterns of the mold and fills the gaps in between. Principally, two different methods exist to accomplish NIL dependent on the used resist. The first method deploys resist which has to be molten up above the glass transition temperature at which the resist starts to flow into all gaps as depicted in figure 4.3(a). After cooling down below the glass transistion temperature and releasing the pressure the polymer keeps the imprinted pattern. Afterwards the mold and the imprinted wafer have to be separated. The second method utilizes polymer resist with low molecular weight. Such a resist flows easily and fills up all gaps in between substrate and a UV light transparent stamp. Afterward, the polymer has to be cross-linked by UV light exposure as shown in figure 4.3(b). NIL requires uniform deviation of pressure and does not allow air inclusion between stamp and substrate. In addition, the aligment by NIL needs high accuracy mechanical precision. Otherwise the substrate may shift away while a mechanical force is applied to the aligned stamp and wafer. To prevent such effects, the air cushion technique can be used. In figure 4.4 the air cushion of a wafer and a stamp between two transparent foils is illustrated. The air within this configuration can be easily evacuated and no air inclusions are possible and perfect contact between substrate and stamp is guaranteed. NIL was demonstrated to enable structuring down to already 6 nm with reasonable effort. [145]

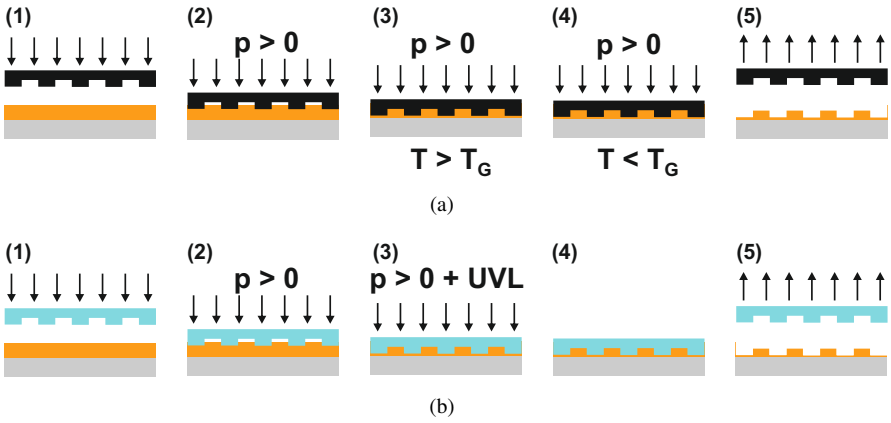

Figure 4.3: Basic principles of Nano Imprint Lithography: A stamp is pressed into resist to transfer nanostructures. (a) Flow of resist under pressure controlled by temperature. (b) Imprint of soft resist under UV light. The resist is cross-linked and nanopatterns remain after separation.

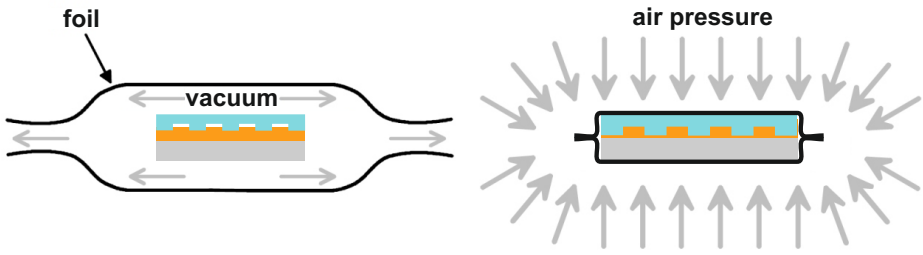

Figure 4.4: Air cushion principles. After aligment, stamp and wafer are evacuated between foils and by air pressure NIL is initiated. Reprinted with permission from the author [146].

4.2 Electrode Deposition

4.2.1 Sputter Deposition

Sputter deposition is attributed to physical ejection of atoms from a target by means of heavy ions, for example Ar^+. The ejected atoms condense on a substrate which is usually oppositely installed to the target. Different kind of sputter deposition methods, such DC sputtering, magnetron sputtering, RF-sputtering, and reactive sputtering exist. All have in common that heavy ions under at least fine vacuum condition are needed to built up a sufficient plasma. The method itself determines, how the ions impact on the target. DC sputtering is elecrically driven, that means the target acts as a cathode. A modification of DC sputtering represents magnetron sputtering. By magnetron sputtering the ions are forced to accelerate on a radially symmetric trajectory before hitting the target. This got the advantage that the plasma is trapped by the magnetic field and high plasma densities are feasible. This increases the efficiency of the sputter process. DC- and magnetron sputtering need a electrically conducting target. Insulating materials can be sputtered deploying RF sputtering. RF sputtering transfers energy into the plasma by transmitting high power radio signals above the target. To achieve different stochiometries of a material, reactive sputtering can be used. By this, the target material reacts with an additional gas introduced into the sputter chamber. This is possible with a mixture or a pure reactive gas source.

4.2.2 E-beam Evaporation

Evaporation allows to deposit material without impinging the substrates' surface with high energetic particles. Evaporation is usually done under UHV condition, because solid materials exhibit low vapor pressure. To sublime the material, energy can be introduced to the system by thermal heating or by accelerated electrons. Electron beam evaporation is preferentially used,

because the inciding electrons allow locally higher temperatures in comparison to pure thermal evaporation, where all material has to be heated up to its melting point. A schematic view of an electron beam evaporator is depicted in figure 4.5. Under UHV condition, typically 10^{-6} hPa and below, electrons are accelerated by an electron gun or another electron emitter and focussed to a material target. The target can be an ingot, a rod, or as shown a crucible with material. The energy of the incident electron beam is transfered to the material, which locally melts or directly sublimates. Usually, the material is cooled by water, otherwise the material may uncontrolledly evaporate and no stable deposition rate would be possible. The substrate is fixed on a sample stage in opposite direction of the electron beam. This prevents unintentionally heating of the wafer. The stage itself may be cooled or heated depending on the deposition material/substrate combination to achieve adhesion. Because electron beam evaporation belongs to the physical vapor deposition methods deposited material shows shadowing on edges. This property allows to utilize e-beam evaporation for lift-off processes.

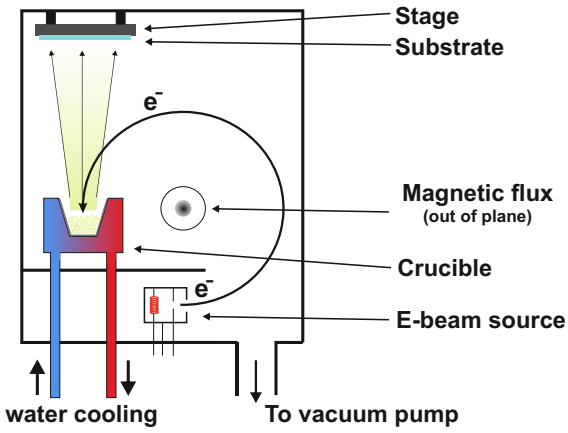

Figure 4.5: Schematical setup of an electron beam evaporator. A material is evaporated by an electron beam and the vapor is deposited on a sample opposite to the material containing crucible.

4.3 Device Process Flow

Nano cross-point devices were fabricated to conduct electrical characterization. Cross-point devices which were taken for characterization with respect to the material properties of TiO_{2-x} achieved by ALD are hereinafter refered as standard devices. Afterwards, a second process flow is described for the preparation of forming-free ReRAM.

4.3.1 Standard ReRAM devices

The fabrication process was started with a 4 inch (100 mm) in diameter silicon wafer. This wafer was oxidized with water vapor resulting in 430 nm thick SiO_2 layer and later coated by 5 nm Ti and 30 nm Pt subsequently by sputtering. Hereafter, the NIL lithography process was utilized to transfer the structure of the bottom electrodes (BE) with a linewidth of 100 nm. In detail, UV-NIL was used in combination with the air cushion method on a nano imprinter. Details on the exact process development and parameter can be found elsewhere [146, 147]. After the imprint process, reactive ion beam etching (RIBE) with oxygen plasma was deployed to carefully open the imprinted areas. The uncovered Ti|Pt layer was etched with Ar^+ ions by an incident beam of 0 ° . Pt protected by resist etched by ions tends to built up fences. Thus, for the fence removal an reactive etching by CF_4 was conducted. After, the wafer was cut into 1 inch by 1 inch dies. The remainder polymer resist on the dies was removed by an ultrasonic cleaning in acetone and 2-propanol followed by oxygen plasma treatment. The deposition of TiO_2 was carried out by the TDMAT process described in the preceding chapter 3. After the TiO_2 ALD process, the top electrodes were patterned by lift-off. For that purpose, the EBL was used to write the structure into a polymer resist and after this the exposed resist was developed. The development was stopped in 2-propanol and cleaned in a ultrasonic bath. The top electrode material, 10 nm Ti as an adhesion layer and 25 nm Pt were deposited by e-beam evaporation. E-beam evaporation was used because very thin layers of TiO_2 should not get damaged by ions like it could happen while sputter deposition. The removal of the sacrificial inverse pattern followed by solvation in boiling acetone and by subsequent ultrasonic treatment lift-off. By that, the target material remained as a TE and all other metallic parts were flushed by a subsequent ultrasonic treatment in 2-propanol. For electrical testing the contact pads of the BE structures have to be freed from the TiO_{2-x} layer as depicted in figure 4.6. To structure the 50 μm by 50 μm large pads, UVL was deployed, since its resolution is sufficient. This was done by a reverse UVL process as described above. The opened windows were used to etch down to the Pt top material by RIBE utilizing CF_4. After, the resin had to be removed. Dry etching of this resin cause cross-linking which needs a thoroughly removal. This was done by EKC 270 dissolved in boiling acetone for 10 minutes and ultrasonic cleaning in acetone and 2-propanol subsequently.

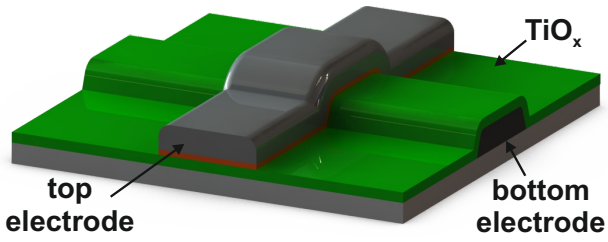

Figure 4.6: Illustration of standard nano cross-point devices. The bottom electrode line is fully covered with TiO_{2-x}.

4.3.2 Forming-free ReRAM devices

The fabrication of forming-free ReRAM devices required nano cross-point structures which differed from the standard ones. In figure 4.7 the scheme of the desired device configuration is shown. Within this configuration the TiO_{2-x} is only between the crossing electrode stripes. Basically, this was achieved by a top-down approach (negative process) to structure the TE material and the TiO_{2-x} thin film in one step down to the BE. This is done be transfering a positive pattern by EBL and dry etching after deposition of the TE of the material stack. Etching down 25 nm of Pt and 10 nm of Ti by Ar^+ ions cause redeposition of Pt and consequently may cause short-circuited devices. Therefore, it is reasonable to alter the material stack. For that purpose TiN was RF sputtered from a stochiometric TiN target. TiN could be easily be etched by RIBE with CF_4. A 5 nm Pt layer was sputter deposited in-situ after TiN to ensure, that switching does not take place in the very first TiO_2 layer on top of hydrolysed TiN. The oxide film was also removed by CF_4, but under an angle of 45 °C. This ensured complete removal from the sidewall of all oxide. The resist was stripped by in N555 at 120 °C for 1 h. Subsequently, the die was cleaned by acetone and isopropanol in a ultrasonic bath.

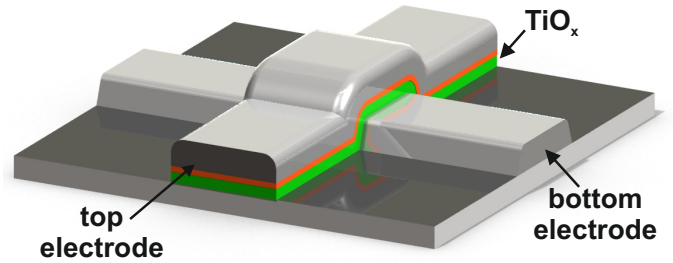

Figure 4.7: Illustration of the prepared forming-free cross-point devices. The TiO_{2-x} is only between botom and top electrode.

4.4 Overview over Fabricated Devices

The standard device process was applied to integrate TiO_{2-x} with different properties, Within the test series, different TiO_{2-x} thicknesses and deposition temperatures were chosen which have been demonstrated to alter the structure and morphology of TiO_{2-x}. For readers convenience, all prepared samples are listed in table 4.1 to allow an overview on the utilized deposition parameters and the TiO_{2-x} properties. Each sample is a symbol assigned for fast indentification in the following chapters.

Table 4.1: Overview over fabricated devices. The devices are distinguished by their thickness and deposition temperature. Each device is represented by its own symbol. a = amorphous, lc = large crystallites, and nc = nano-crystalline

device	thickness / nm	deposition temperature / °C	crystallinity	type
200°C 3 nm	3	200	a	standard
200°C 5 nm	5	200	a	standard
200°C 15 nm	15	200	a	standard
250°C 3 nm	3	250	a	standard
250°C 5 nm	5	250	a	standard
250°C 8 nm	8	250	a	standard
250°C 15 nm	15	250	lc	standard
250°C 25 nm	25	250	lc	standard
300°C 3 nm	3	300	a	standard
300°C 5 nm	5	300	a	standard
300°C 8 nm	8	300	nc	standard
300°C 15 nm	15	300	nc	standard
300°C 25 nm	25	300	nc	standard
FREE 300°C 25 nm	25	300	nc	forming-free

CHAPTER

FIVE

TRANSPORT INVESTIGATIONS ON PRISTINE TIO_{2-X} RERAM

This chapter focuses on the investigation of the electrical transport mechanism of the pristine state in as-fabricated devices before electroforming takes place. The current-voltage (IV)-characteristics are discussed as well as the activation of the electrical transport derived from deep temperature measurements. Different possible transport models and their comparison to the observations are presented to clarify the influence of the thickness, the crystallinity, and the morphology on the conduction process in the TiO_{2-x} based cross-point cells.

5.1 Initial Device State Statistics

First, the pristine device resistance of the standard devices was analyzed. To qualify the influence of the morphology and the structure of the different TiO_{2-x} films (see chapter 3) IV sweeps were performed on 150 devices each sample. The IV-sweeps were carefully carried out between ±150 meV to prevent any irreversible change in the device state which can be induced by higher voltages or longer voltage stress [16]. The dependence of the read current at 100 mV on the TiO_{2-x} thickness is depicted in figure 5.1(a) for TiO_{2-x} films deposited at different temperatures. Generally, the read current increased with increasing thickness and with increasing TiO_{2-x} deposition temperature. It was not possible to detect any reliable current signal on 3 nm thick TiO_{2-x} devices grown at 200 °C and 250 °C. Increasing the read voltage up to 800 mV yielded a measurable current, smaller for TiO_{2-x} grown at 200 °C as compared to TiO_{2-x} deposited at 250 °C. Nevertheless the calculated resistances were in the TΩ regime. Thus, ultra thin amorphous TiO_{2-x} layers seem to be perfectly insulating. But a perfect insulator should not allow more than six orders of magnitude higher currents when the thickness of the film is increased by about a factor of 8. This may indicate the presence of defects within the bulk volume of the TiO_{2-x} thin films. The increase of the peak current with increasing thickness was significantly faster in crystalline TiO_{2-x} films grown from 250 to 300 °C as compared to amorphous TiO_{2-x} films grown

at 200 °C. In chapter 3 the strong influence of the deposition temperature on the crystallization was demonstrated. Thus, the morphology seems to affect the device current significantly and the pristine resistance state changes over several orders of magnitude. The resistance derived from the leakage measurements is shown in figure 5.1(b). The initial resistance of pristine devices mostly scattered for thick, crystalline TiO_{2-x} grown at 250 °C. The determined distribution is Poisson-like, exemplary shown in figure 5.1(c).

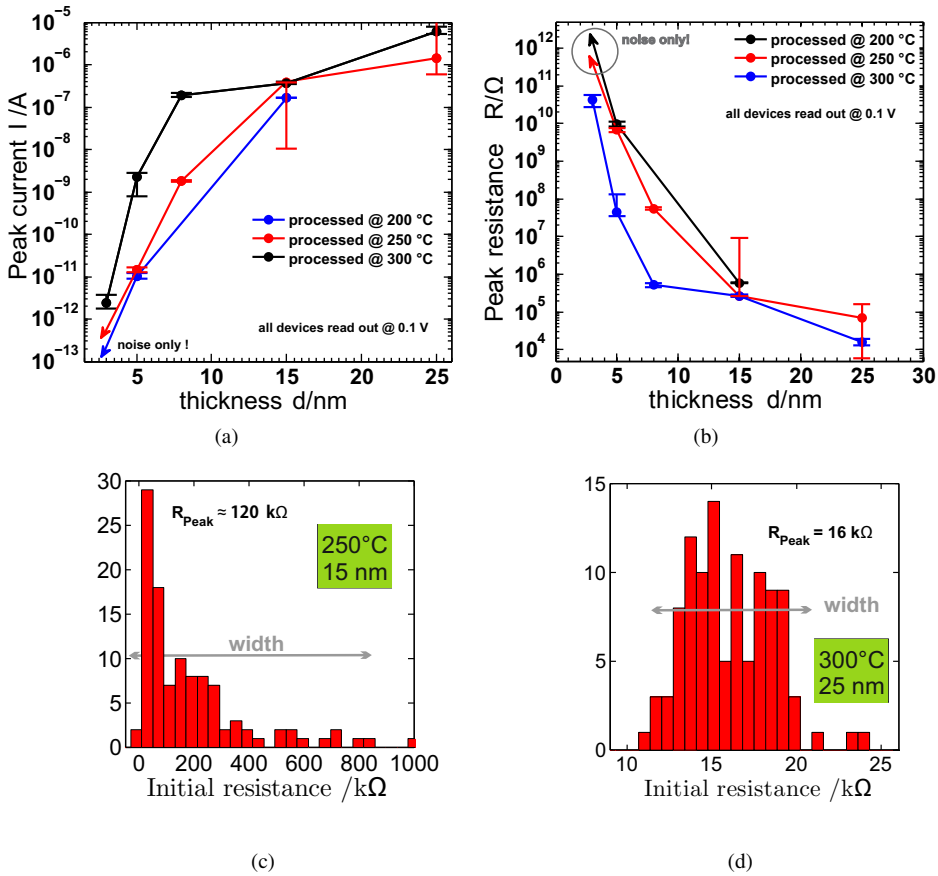

Figure 5.1: Measurement of the pristine state of $Si|SiO_2|Ti|Pt|TiO_{2-x}|Ti|Pt$ devices dependent on thickness and deposition temperature of TiO_{2-x}. (a) Initial current at a read voltage of 0.1 V. (b) Derived resistances. In both graphs arrows on the curves mark non-detectable current values and, respectively, infinite resistance values at given measurement condition. In (c) and (d) the statistical distribution of the resistance values of pristine devices is plotted. (c) Poisson-like statistic is observed for TiO_{2-x} thin films grown at 250 °C while in (d) Gaussian shape distribution of the resistance values is found for films deposited at 300 °C.

Amorphous and crystalline thin films deposited at 200 °C and 300 °C, respectively, exhibit a Gaussian-like distribution as depicted in figure 5.1(d). This agrees well the morphological study in chapter 3. Large crystallites in the films correlate to a highly non-uniform pristine device resistance distribution, whereas small crystallites, or amorphous films exhibit a uniform distribution of the device resistance. Therefore, only amorphous and nano-crystalline samples were further considered.

5.2 Conduction Mechanism

Different thickness and crystallinity of the thin films correlate to different initial device resistances ranging from perfectly insulating TiO_{2-x} thin films to semiconducting films with low resistances of several tenth kΩ. From this large change of the resistance different conduction mechanism might have to be considered for films of different thicknesses. In general, conduction mechanisms can be divided into two main groups, one is controlled by interface-related effects, for example the Schottky effect, and the other comprises bulk limited mechanisms, for example the Poole-Frenkel effect.

5.2.1 Interface-related Conduction Mechanisms

Interface-related effects basically describe the electronic transport by passing the metal-semiconductor interface or tunneling through an insulator. As a consequence, the description of the conduction process involves electronic properties of the electrodes such as the Fermi level and the work function.

5.2.1.1 Tunneling Effects

Basically, tunneling mechanism can be distinguished by the manner how an electron overcomes the tunneling barrier. In figure 5.2 three different types of tunneling over the insulator are depicted: Tunneling can take place through a triangular potential wall, or a rectangular potential wall, or electrons can tunnel via traps within the insulator. These models are called Fowler-Nordheim tunneling, direct tunneling, and trap-assisted-tunneling (TAT), respectively.

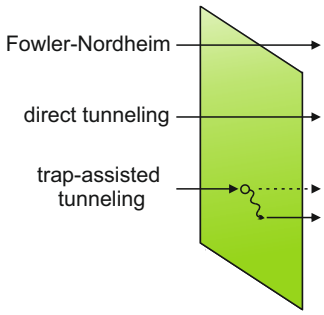

Figure 5.2: Schematic drawing of models for the tunneling models through an insulating barrier.

By all models the supply of electrons and the quantum-mechanically transmission through the insulator needs to be described. This is considered by the Tsu-Esaki expression [148] for the current flow through an insulator:

$$j = \frac{4\pi m_{\text{eff}}}{h^3} \int T(E_x) dE_x \int_0^\infty (f_1(E) - f_2(E)) dE \tag{5.1}$$

m_{eff} is the effective mass of the electrons in the electrode, T is the transmission coefficient perpendicular to the electrode-insulator interface, and the Fermi-Dirac distributions f_i represent the supply function of the electrons from the electrodes. The transmission is approximated by the Wentzel-Kramer-Brillouin (WKB) method

$$T(x) = -\frac{2}{\hbar} \exp\left(\int_0^{\tilde{x}} \sqrt{2m_{\text{DE}}(E_{\text{CB}} - E_x)} \right) dx \tag{5.2}$$

E_{CB} is the conduction band edge, m_{DE} the effective mass of an electron in the insulator, and $\tilde{x}$ is the turning point of the wave function through the barrier. The turning point has to be defined either for Fowler-Nordheim tunneling or direct tunneling. Fowler-Nordheim tunneling assumes a triangular shape of the conduction band edge through the tunneling barrier neglecting the work function difference of the electrodes. Thus, the current density for the case of Fowler-Nordheim tunneling can be expressed as [149]

$$\boxed{j_{\text{FN}} = \frac{q^3 m_{\text{eff}}}{8\pi m_{\text{DE}} h\varphi} F_{\text{DE}}^2 \exp\left(-\frac{4\sqrt{2m_{\text{DE}}(q\varphi)^3}}{3\hbar} \frac{1}{F_{\text{DE}}} \right)} \tag{5.3}$$

where F is the dielectric field over the insulating dielectric, m_{eff} is the effective mass in the dielectric, and φ is the maximum barrier height measured from the Fermi level of the metal from where electrons tunnel from.
Similarly, the tunneling transmission is approximated in the case of direct tunneling. Under the same assumptions, the second insulator-electrode interface $\tilde{x} = d$ is taken as turning point [150]. This yields

$$\boxed{\begin{aligned} j_{\text{DT}} = {} & \frac{q^3 m_{\text{eff}}}{8\pi h m_{\text{DE}} ((q\varphi)^{1/2} - (q\varphi_1 - qF_{\text{DE}})^{1/2})^2} F_{\text{DE}}^2 \\ & \times \exp\left(-\frac{4\sqrt{2m_{\text{DE}}(q\varphi)^3}}{3\hbar} \left((q\varphi)^{3/2} - (q\varphi - qF_{\text{DE}})^{3/2} \right) \right) \end{aligned}} \tag{5.4}$$

Trap-assisted tunneling differs from that forms. Different theoretical approaches were made to analytically solve the transmission coefficient, but they do not cover the experimentally observable current flow [149]. Nevertheless, experimental results are in agreement with following empirical relationship between the current density and the electric field [151, 152]

$$\boxed{j_{\text{TAT}} = CF \exp\left(-\frac{4\sqrt{m_{\text{eff}}\varphi^3}}{3h} \frac{1}{F} \right)} \tag{5.5}$$

Here C is an empirical constant.

As a conclusion, the tunneling mechanism can be identified by electric field dependent plots of the current density. In case of Fowler-Nordheim tunneling, a $\log\left(\frac{j}{F^2}\right)$ vs F plot should show a slope from which the barrier height can be determined at given effective mass of the electrons in the dielectric. Similarly, a $\log\left(\frac{j}{F}\right)$ vs F plot yields the barrier height if trap-assisted tunneling occurs. Direct tunneling needs much more complex fitting of the current density as a function of electric field and the barrier height.

5.2.1.2 Schottky Effect

If a semiconducting material is in contact with a metal, electrons may exchanged at the interface. By this, thermodynamic equilibration leads to the exchange of electrons in the boundary layer. The steady state of the exchange of the electrons is schematically illustrated in figure 5.3 for a n-type semiconductor. Electrons from the semiconductor preferably tend to be excited into the conduction band of the metal, leaving a depletion region in the semiconductor [153]. This results in the formation of the Schottky barrier measured from the Fermi level E_F. The conduction process which involves a Schottky barrier is polarity dependent. Forward bias describes the Schottky contact under negative polarity, backward bias describes conduction under positively applied voltage. In forward direction, electrons are injected into the barrier from the semiconductor. Thus, electrons are allowed to flow across the Schottky barrier. This is described by thermionic emission [154]:

$$j = A^\star T^2 \exp\left(-q\frac{\varphi_{B,eff}}{kT}\right)\left[\exp\left(\frac{qU}{kT}\right) - 1\right] \tag{5.6}$$

$$A^\star = \frac{4\pi q k^2 m_{eff}}{\hbar^3} = 120\frac{m_{eff}}{m}\frac{A}{cm^2K^2} \tag{5.7}$$

$\varphi_{B,eff}$ is the effective Schottky barrier, $A^\star$ the Richardson constant, m and m_{eff} the electron mass and the effective electron mass, respectively, and U the applied voltage.
In backward direction, the Schottky barrier has to be overcome by thermionic emission [155]. By applying negative voltage $|-qU| >> kT$, the voltage dependency in equation 5.6 can be neglected

$$j = A^\star T^2 \exp\left(-q\frac{\varphi_{B,eff}}{kT}\right) \tag{5.8}$$

Polarity inversion lowers the Schottky barrier by creating images forces [156]. By this, a potential drop can be calculated which depends on the dielectric permittivity and the applied electric field:

$$\boxed{\Delta\varphi = \left(\frac{qF}{4\pi\epsilon\epsilon_r}\right)^{\frac{1}{2}}} \tag{5.9}$$

Hence, equation 5.8 reads

$$\boxed{j_{Schottky} = A^\star T^2 \exp\left(-q\frac{\varphi_{B,eff} - \Delta\varphi}{kT}\right)} \tag{5.10}$$

If asymmetric electrodes cause a Schottky barrier, a $\log\left(\frac{j}{T^2}\right)$ vs $(F^{\frac{1}{2}})$ plot allows to extract the dielectric permittivity and the Richardson constant from the resulting slope.

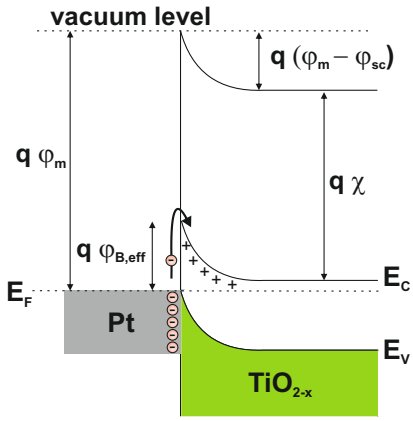

Figure 5.3: Interface between a metal (Pt) and n-type semiconductor (TiO_{2-x}). Thermal equilibration leads to a Schottky barrier at the semiconductor interface. Electrons can be thermally excited over the Schottky barrier under backward bias.

5.2.2 Bulk-limited Conduction Mechanisms

Bulk-limited conduction mechanisms are predominantly linked to intrinsic properties of the semiconductor. Hence, the different material properties such as crystallinity and defects may play an important role to correctly describe the conduction processes in thick films, or in films with high defect concentrations with respect to their thickness.

5.2.2.1 Space-Charge-Limited Current

A variety of materials, for example amorphous solids exhibit low charge carrier mobilities. Reasonably, the mobility is the limiting factor for the bulk transport. In that case the forced injection of charge carriers plays an important role. Forced injection needs an ohmic contact in the sense that charge carriers are supplied from the electrode or the electrode provides a reservoir of charge carriers to enter the bulk [157]. Besides the electrode material, the trap density within the semiconductor is important for the correct characterization of the conduction mechanism. Traps can capture injected charge carriers and reasonably influence strongly the conduction. This is described by the space-charge-limited-current (SCLC) mechanism. SCLC is classified by the trap density distribution. The simplest case is the SCLC through a trap-free insulator. That means, the Poisson equation needs to be only solved for injected charge carriers.

$$\frac{dF(x)}{dx} = \frac{q}{\epsilon_0 \epsilon_r} n_f \tag{5.11}$$

where n_f denotes the density of charge carriers freely involved in transport. By inserting the current density $j = q\mu F(x)n_f$ into the Poisson equation

$$\frac{dF(x)}{dx} = \frac{j}{\epsilon_0 \epsilon_r \mu F(x)} \tag{5.12}$$

the expression can be analytically solved and the current density is given by:

$$\boxed{j_{\mathrm{SCLC,trap-free}} = \frac{9}{8}\,\mu\,\epsilon_0 \epsilon_r \frac{U^2}{d^3}} \tag{5.13}$$

This equation is known as Child's law [158] as well as Mott-Gurney law [159].
In the presence of traps, the injected charge is strongly influenced. Reasonably, the Fermi level alters to keep the thermodynamically equilibrium. Therefore, the portion of the injected charge which is freely available for the transport will be modulated [157]

$$n_f = N_{\mathrm{CB}} \exp\left(-\frac{E_{\mathrm{CB}} - E_F}{kT}\right) \exp\left(\frac{\Delta E}{kT}\right) \tag{5.14}$$

In this context, N_{CB} is the number of states within a slice kT in the conduction band and the difference $E_{\mathrm{CB}} - E_F$ measures the depth of traps from the conduction band edge. ΔE is the shift of the Fermi level. The shift depends on the injected charge which correlates with the trap density and the voltage. For uniform trap distribution over the half band gap of the semiconductor the current density depends exponentially on the voltage

$$j \propto \exp(\alpha U) \tag{5.15}$$

The exponential factor $\alpha = \alpha(n_t)$ depends on the trap density. Uniform trap distribution in energy does not represent a physical solution. According to this, Rose [157] ,and Mark et al. [158] suggested that the steepness of the distribution is described by $\exp\left(-\frac{E_{\mathrm{CB}}-E_F}{kT_C}\right)$. Here, the characteristic temperature T_C is greater than the bulk temperature T. Thus, the current was derived as a function of the voltage

$$\boxed{j_{\mathrm{SCLC,trap}} \propto U^{\left(\frac{T_C}{T}+1\right)}} \tag{5.16}$$

with a temperature dependent exponential factor which can be determined by a $\log(j)$ vs $\log(U)$ plot. The exponential factor has to be always greater than 2 if traps are involved in transport, otherwise the current density is given by Child's law.

5.2.2.2 Classical Poole-Frenkel Model

Conduction in a bulk may not be only caused by trap modulated charge injection. The thermal ionization of charge carriers from the bulk can result in carrier concentrations high enough to lead to bulk-controlled conduction. The free motion of thermally ionized electrons in a neutral medium under an electric field were described by Frenkel [160]. In comparison to vacuum ionization, the electric field of the ionization site is screened by the surrounding medium while

the ionization process. Therefore, a potential drop from the surrounding potential is reasonable. While ionization, the presence of the electric field has to be additionally taken into account as depicted in figure 5.4. The effective difference of the potential is the superposition of both, the field of the ionic site and the electric field. This results in the lowering of the ionization energy E_i by

$$\Delta E = 2\left(\frac{q^3 F}{\epsilon_0 \epsilon_r}\right)^{\frac{1}{2}} = 2\beta F^{1/2} \tag{5.17}$$

with $\beta = \left(\frac{q^3}{\epsilon_0 \epsilon_r}\right)^{\frac{1}{2}}$. Thus, the conductivity reads

$$\sigma = \sigma_0 \exp\left(-\frac{E_i - \Delta E}{2kT}\right) \tag{5.18}$$

where σ_0 is the ground conductivity, not further discussed. Using Ohm's law and expression 5.17 the current density can be written as

$$j = \sigma_0 F \exp\left(-\frac{E_i}{2kT}\right)\exp\left(\frac{\beta}{kT}F^{\frac{1}{2}}\right) \tag{5.19}$$

This is the case for intrinsic thermionic emission of electrons or holes. If extrinsic donators or traps are present in the material equation 5.19 has to be corrected to

$$\boxed{j_{CPF} = \sigma_0 F \exp\left(-\frac{E_i}{kT}\right)\exp\left(\frac{\beta}{kT}F^{\frac{1}{2}}\right)} \tag{5.20}$$

due to the mass law action [161].

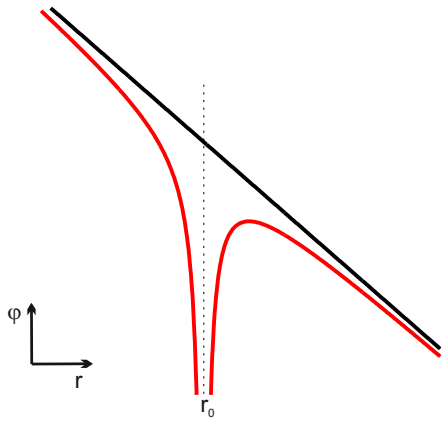

Figure 5.4: Schematical function trace of the effective potential in the classical Poole-Frenkel model. The field of the ionization center and the applied electric field are superimposed.

5.2.2.3 Poole-Frenkel in Weak Electric Fields

Frenkel's derivation is based on pure empirical assumptions. A semi-classical approach which considers the supply function N_{E} as well as the emission probability of the ionization centers

$$j = q \int D(E) \cdot N(E) dE \tag{5.21}$$

was developed by Hill [162]. This model differs significantly from the classic Poole-Frenkel model. The supply function in one dimension is given by

$$N(E) = \int \frac{\partial N_{\mathrm{a}}}{\partial E} f \partial E \tag{5.22}$$

The variable f is the Fermi function of the source and the expression $\frac{\partial N_{\mathrm{a}}}{\partial E}$ is the derivative of the DOS of defects in the material, whether it is of crystalline or amorphous nature. To derive an analytical solution, $\frac{\partial N_{\mathrm{a}}}{\partial E}$ is assumed to be constant in energy and is further called N_{i} in units of $(\mathrm{m}^{-3} \cdot \mathrm{eV}^{-2})$. Integration gives the supply function

$$N(E) = N_{\mathrm{i}} kT \ln\left(1 + \exp\left(\frac{E_{\mathrm{F}} - E_{\mathrm{x}}}{kT}\right)\right) \tag{5.23}$$

E_{F} denotes the Fermi level. Introduction into equation 5.21 and utilizing the WKB approximation yields

$$\tilde{j} = q N_{\mathrm{i}} kT \int \ln\left(1 + \exp\left(\frac{E_{\mathrm{F}} - E_{\mathrm{x}}}{kT}\right)\right) \cdot D(E) \cdot \frac{\partial \mathrm{v}_{\mathrm{x}}}{\partial E} dE \tag{5.24}$$

The current density is differently noted taking into account the derivative of the DOS of defects was assumed to be constant for integration. At this point a clear distinction has to be made between semicrystalline host material and a purely amorphous system. The velocity factors in WKB approximation can be read as

$$\frac{\partial \mathrm{v}_{\mathrm{x}}}{\partial E} dE = \mu_1 F \tag{5.25}$$

for semicrystalline host and

$$\frac{\partial \mathrm{v}_{\mathrm{x}}}{\partial E} \partial E = \mu_2 F^{\frac{1}{2}} \tag{5.26}$$

for amorphous material. μ_1, μ_2 are the mobilities for semicrystalline and amorphous material, respectively [162]. Reasonably, equation 5.24 has to be further considered in different ways:

$$\tilde{j} = q N_{\mathrm{i}} kT \mu_1 F \int_{E_{\mathrm{i}} - \beta F^{\frac{1}{2}}}^{\infty} \ln\left(1 + \exp\left(\frac{E_{\mathrm{F}} - E_{\mathrm{x}}}{kT}\right)\right) dE \tag{5.27}$$

$$\tilde{j} = q N_{\mathrm{i}} (kT)^2 \mu_1 F \exp\left(-\frac{E_{\mathrm{i}} - \beta F^{\frac{1}{2}}}{kT}\right) \tag{5.28}$$

and

$$\tilde{j} = qN_i kT\mu_2 F^{\frac{1}{2}} \int_{E_i-\beta F^{\frac{1}{2}}}^{\infty} \ln\left(1+\exp\left(\frac{E_F-E_x}{kT}\right)\right)dE \tag{5.29}$$

$$\tilde{j} = qN_i(kT)^2\mu_2 F^{\frac{1}{2}} \exp\left(-\frac{E_i-\beta F^{\frac{1}{2}}}{kT}\right) \tag{5.30}$$

To finally calculate the current flux, the emission probabilities for the semicrystalline case (simple field-directed emission)

$$P_{\text{semicryst}} \propto \exp(-\alpha) \tag{5.31}$$

and hemispherical emission into amorphous host [163] have to be inserted

$$P_{\text{amorphous}} \propto \alpha^{-2}(1+(\alpha-1)\exp(\alpha)) + \frac{1}{2} \tag{5.32}$$

where α is given by

$$\alpha = \frac{\beta F^{\frac{1}{2}}}{kT} \tag{5.33}$$

A charge carrier can be emitted in direction or opposite direction to the electric field. According to this, the probabilities have to be replaced by the respective sum in forward and backward direction

$$P_{\text{semicryst},\pm} \propto \exp\left(-\frac{E_i}{kT}\right) 2\sinh\alpha \tag{5.34}$$

$$P_{\text{amorphous},\pm} \propto \exp\left(-\frac{E_i}{kT}\right) 2\alpha^{-2}(\alpha\cosh\alpha-\sinh\alpha) \tag{5.35}$$

Thus, the current density in 5.28, 5.30 can be rewritten to

$$\tilde{j} = 2qN_i(kT)^4\beta^{-2}\mu_1 \cdot \exp\left(-\frac{E_i}{kT}\right)\cdot\alpha^2\sinh\alpha \tag{5.36}$$

$$\tilde{j} = 2qN_i(kT)^3\beta^{-1}\mu_2 \cdot \exp\left(-\frac{E_i}{kT}\right)\cdot\alpha^{-1}(\alpha\cosh\alpha-\sinh\alpha) \tag{5.37}$$

The assumption of the constant derivative of the defect DOS has to be corrected by replacing N_i by $N_a(kT)^{-2}$. With this, the current density in a semicrystalline host at weak electric fields becomes

$$\boxed{j_{\text{SCPF,sc}} = 2qN_a\mu_1 F \exp\left(-\frac{E_i}{kT}\right)\sinh\left(\frac{\beta}{kT}F^{1/2}\right)} \tag{5.38}$$

which matches the classical Poole-Frenkel equation for higher electric fields. The current density of purely amorphous host emission does not obviously lead to any physical solution and is left out.

Poole-Frenkel emission, whether in the classical model or semi-classical approach, assumes only a single site defect surrounded by the average potential. But a single defect is no longer

valid, if the defect concentration increases and the defect to defect distance is very close. Thus, both models will fail at a certain critical defect density. The critical defect concentration

$$N_{\mathrm{a,critical}} \approx (q\beta^{-1}F^{\frac{1}{2}})^3 \tag{5.39}$$

is plotted as a function of the electric field for different dielectric permittivity values in figure 5.5.

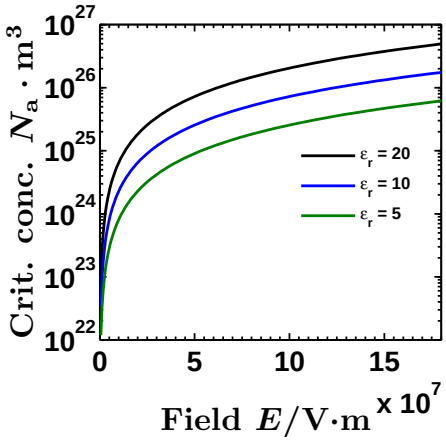

Figure 5.5: Calculated critical defect density of the classical Poole-Frenkel model as a function of the electric field.

5.2.2.4 Multi Center Poole-Frenkel Model

To describe the Poole-Frenkel emission in the range of the critical defect concentration and above, a two center case can be considered where two potential wells superimpose as shown in figure 5.6. As a consequence, only the emission over the middle energy barrier has to be taken into account for low electric fields. It is of importance to mention that this consideration implies the interaction of localized conduction paths which form a conduction network.
In the following only the results are discussed. For the integration over the potential barrier the energy has to be rewritten to $E_\mathrm{i} = E_\mathrm{a} - \frac{1}{2} F s$ where E_a is the experimentally observable activation energy for thermal emission. s is the inter-center spacing from site to site. As a consequence of the hopping-like emission the 'attempt to escape frequency' ν has to be inserted into the emission probability

$$P_{\mathrm{semicryst},\pm} \propto \nu \exp\left(-\frac{E_\mathrm{a}}{kT}\right) 2 \sinh \alpha' \tag{5.40}$$

$$P_{\mathrm{amorphous},\pm} \propto \nu \exp\left(-\frac{E_\mathrm{a}}{kT}\right) 2\alpha'^{-2} \left(\alpha \cosh \alpha' - \sinh \alpha'\right) \tag{5.41}$$

where

$$\alpha' = \frac{qFs}{2kT} \tag{5.42}$$

The current density is derived in the same way as compared to single center emission.

$$\tilde{j} = 2qN_\mathrm{i}(kT)^2 \cdot s\nu \cdot \exp\left(-\frac{E_\mathrm{a}}{kT}\right) \cdot \sinh \alpha' \tag{5.43}$$

$$\tilde{j} = 2qN_\mathrm{i}(kT)^2 \cdot s\nu \cdot \exp\left(-\frac{E_\mathrm{a}}{kT}\right) \cdot \alpha'^{-1} \left(\alpha' \cosh \alpha' - \sinh \alpha'\right) \tag{5.44}$$

Taking again into account, that N_i has to be replaced by $N_\mathrm{a}(kT)^{-2}$, the current density is finally given

$$\boxed{j_\mathrm{MCPF,sc} = 2qN_\mathrm{a} \cdot s\nu \cdot \exp\left(-\frac{E_\mathrm{a}}{kT}\right) \cdot \sinh \alpha'} \tag{5.45}$$

$$\boxed{j_\mathrm{MCPF,a} = 2qN_\mathrm{a} \cdot s\nu \cdot \exp\left(-\frac{E_\mathrm{a}}{kT}\right) \cdot \alpha'^{-1} \left(\alpha' \cosh \alpha' - \sinh \alpha'\right)} \tag{5.46}$$

for Multi-center Poole-Frenkel emission into semicrystalline host and purely hemispherically emitted charge carriers into purely amorphous material, respectively. From a two parameter fit of $s \cdot f\left(\alpha'(s)\right)$ and the expression $2qN_\mathrm{a}\nu \exp\left(-\frac{E_\mathrm{a}}{kT}\right)$ the hopping distance and the defect density can be extracted from a IV sweep at given attempt to escape frequency ν.

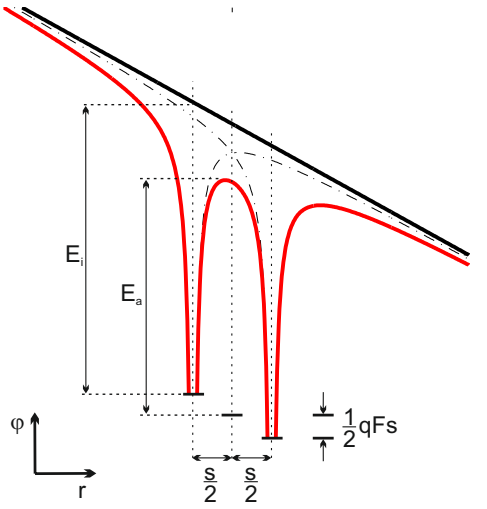

Figure 5.6: The function trace of the effective potential of two neighbouring intrinsic defect sites under a electric field. The propinquinty of the sites causes a lower activation energy E_a of emission into a solid as compared to the activation energy E_i of a single site.

5.2.2.5 Adiabatic Small Polaron Hopping

In crystalline host material drifting electrons can locally polarize the lattice by attraction of positively charged ions and/or repulsion of negatively charged ions. This may happen in ionic as well as covalent bonded materials. The attraction causes a deformation of the lattice which follows the electron. Thus, the polarization field follows the electron and this entity is considered as a quasi-particle, the polaron. A polaron represents a distortion of the lattice dynamics and therefore electron-phonon coupling appears. To describe such a system quantum-mechanically Fröhlich [164, 165] proposed a Hamiltonian

$$H = H_{\mathrm{ph}} + H_{\mathrm{e-ph}} + H_{\mathrm{e}} \tag{5.47}$$

which describes the energy of the lattice vibration (phonon), the electron-phonon coupling, and the electron. An excellent theoretically treatment of polaron transport can be found in [166]. In the framework of the present study, the derivation of the adiabatic conduction by small polarons is treated in parts. The interested reader is referred to [167, 166]. The solution over the Hamiltonian 5.47 of a higher number ions is quite complex and cannot be expressed analytically, but some simplification enables to reveal the motion of small polarons in a lattice. For this purpose, the electronic wave-function is approximated to be of nearest neighbor as representatives for the whole lattice only two ion sites are taken into account with an optical phonon frequency ω_{op}^2 [166]. With this, the Hamiltonian in equation 5.47 is derived as

$$H = \frac{M}{2}(v_1^2 + v_2^2) + \frac{M}{2}\omega_{\mathrm{op}}^2(x_1^2 + x_2^2) + A(x_1 - x_2)(a_1^\dagger a_1 - a_2^\dagger a_2) + J(a_1^\dagger a_2 + a_2^\dagger a_1) \tag{5.48}$$

M is the mass of the host ion, x_i the displacement coordinate, and its velocity v_i. The variable A describes the coupling between the phonon and electron, $a_i^\dagger$, a_i the creation and annihilation operators of the electronic states. J is the resonance integral over two neighboring sites (electronic states). Introducing reduced coordinates $x := x_1 - x_2$ and $X := \frac{x_1+x_2}{2}$ simplifies the Hamiltonian. The absolute motion of the system by X and its velocity V can be neglected to solve the problem

$$H = \frac{M}{2}v^2 + \frac{M}{4}\omega_\mathrm{op}^2 x^2 + Ax(a_1^\dagger a_1 - a_2^\dagger a_2) + J(a_1^\dagger a_2 + a_2^\dagger a_1) \tag{5.49}$$

and two solutions occur

$$E_\pm = \frac{\omega_\mathrm{op}^2 M}{4}x^2 \pm \sqrt{A^2x^2 + J^2} \tag{5.50}$$

The energy levels are qualitatively depicted in figure 5.7(a). At low energies a polaron oscillates around x_0 or $-x_0$ within a minimum potential energy

$$E_a = \frac{A^2}{\omega_\mathrm{op}^2}\frac{1}{M} \tag{5.51}$$

Within such a minimum, the polaron (system) oscillates with small amplitude. Fluctuations let the polaron non-adiabatically pass over to E_+ or let it cross over adiabatically to the next well from x_0 to $-x_0$, or vice versa. In the presence of an electric field the expression

$$q\underline{F}\underline{R}_1 a_1^\dagger a_1 - q\underline{F}\underline{R}_2 a_2 a_2^\dagger = \frac{1}{2}q\underline{F}\left[\left(\underline{R}_1 + \underline{R}_2\right)\left(a_1^\dagger a_1 + a_2 a_2^\dagger\right) + \left(\underline{R}_1 - \underline{R}_2\right)\left(a_1^\dagger a_1 - a_2 a_2^\dagger\right)\right] \tag{5.52}$$

has to be added to the Fröhlich Hamiltonian in 5.49. $\underline{R}$ denotes the site of the electron wave function under consideration. The solution of the modified Hamiltonian is given by:

$$E_\pm = \frac{\omega_\mathrm{op}^2 M}{4}x^2 \pm \sqrt{\left(Ax + \frac{qFs}{2}\right)^2 + J^2} \tag{5.53}$$

Qualitatively, the potential wells in figure 5.7(a) have to be shifted in energy by $\mp\frac{1}{2}qFa$ at the sites $-x_0$, x_0. By this, the chainlike hopping from well to $-x_\mathrm{i}$, $x_{\mathrm{i}+1}$ is given by

$$P = \exp\left(E_\mathrm{a} - \frac{1}{2}qFs + \frac{qFs}{16E_\mathrm{a}}\right) \tag{5.54}$$

The current density can be calculated using

$$j = -qN_\mathrm{sp}\mathrm{v} \tag{5.55}$$

where N_sp is the small polaron density. The small polaron velocity v is a result from hopping events from the left to the right and vice versa caused by the applied electric field. Consequently the velocity reads:

$$\mathrm{v} = s\frac{\omega_\mathrm{op}}{\pi}\left(P_\mathrm{left} - P_\mathrm{right}\right) \tag{5.56}$$

$$P_\mathrm{left} - P_\mathrm{right} = \exp\left(-\frac{E_\mathrm{a}}{kT}\right)\left[\exp\left(-\frac{qFs}{2kT}\right) - \exp\left(\frac{qFs}{2kT}\right)\right]\exp\left(\frac{(qFs)^2}{16E_\mathrm{a}}\right) \tag{5.57}$$

The attempt frequency for a hopping polaron is $\frac{\omega_{op}}{\pi}$. Assuming $(eFs)^2 << 16E_a$ the current density can be rewritten to

$$j_{SPH} = qN_{sp}\frac{\omega_{op}}{\pi}s\exp\left(-\frac{E_a}{kT}\right)\sinh\left(\frac{eFs}{2kT}\right) \tag{5.58}$$

$$\boxed{j_{SPH} = 2qN_{sp}\nu s\exp\left(-\frac{E_a}{kT}\right)\sinh\left(\frac{eFs}{2kT}\right)} \tag{5.59}$$

which interestingly matches equation 5.45, except the defect density N_a. Thus, both conduction mechanism can be fitted by the same equation.
The transport by adiabatic small polarons is valid as long as the relation $qFa < 4E_a$, otherwise the polaron dissociates. Above, with $qFa \geq 4E_a$ the two site small polaron model fails, and the current is expected to decrease with the electric field.

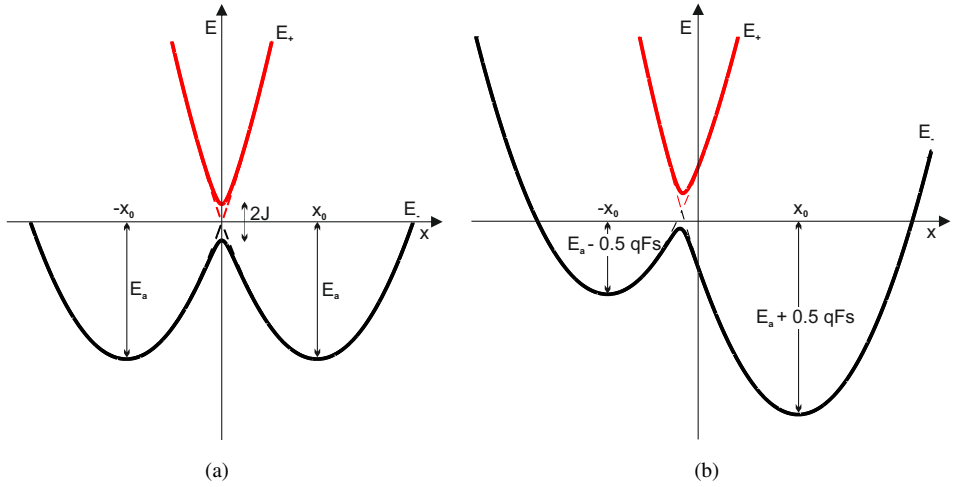

Figure 5.7: Energy levels of a small polaron in the two site model: In (a) without external electrical field. A polaron can move through the lattice adiabatically between two minimum of the lower state, or can non-adibatically cross over to the higher state. In (b) a electric field elevates and decreases the ground states of the small polaron.

5.3 Characterization of the Pristine TiO_{2-x} Devices

5.3.1 Activation Energy of Conduction

In this study, it was already demonstrated that the conductivity of TiO_{2-x} devices depends on the thickness as well as crystallinity. Higher conductivity with increasing thickness may result from the presence of defects, or second phases which behave like extended defects. In order to discuss possible types of defects, the activation energy of conduction was determined from temperature dependent experiments between 220 K to 300 K for a set of devices. The experimental conditions were carefully chosen to ensure that device states were not changed by too high voltages and that the sample temperature matched the cryostat. Thus, the sample was slowly, stepwise cooled down and the IV-characteristic recorded. After temperature stabilization, a single voltage sweep between ± 100 mV was applied to measure the current each ≈ 5-10 K. The activation energy was derived from the slope of the normalized conductance vs the reciprocal temperature shown in figure 5.8(a). Different activation energies were determined dependent on the thickness and the crystallinity of the TiO_{2-x} thin films. Generally, thin TiO_{2-x} of amorphous nature exhibit activation energies around 300 meV. The activation energy decreased with increasing thickness and was even lower for crystalline samples. For comparison, the conductances of the 15 nm thick amorphous and crystalline TiO_{2-x} films were characterized by a thermal activation energy of about 137 ± 5 meV and 112 meV, respectively. As can be seen from table 5.1 the activation energy of crystalline TiO_{2-x} decreases to only 42 meV at a thickness of 25 nm. In contrast to this work, activation energies from 200 to 500 meV were reported on 35 nm thick sputtered pristine TiO_2 [168]. The question arises, how does the crystallinity influence the device state and which conduction mechanism is connected to the found activation energy.
In literature several works report on conduction mechanisms and respective activation energies in bulk as well as thin film TiO_2. Deskins et al. calculated by the DFT-U method the polaron motion in anatase as well as rutile TiO_2 [169]. Non-adiabatic polarons show activation energies of around 0.3 eV, whereas the activation energy of thermally assisted hopping by adiabatic transfer along the c-axis is determined to 0.2 eV. Furthermore, the oxygen deficiency of the grown TiO_{2-x} thin films has to be addressed. Ghosh et al. demonstrated by thermoluminescence and conduction experiments that eight different types of shallow traps can exist in a reduced rutile crystal [170]. The depth of the shallow traps were estimated between 0.27 eV up to 0.87 eV measured from the conduction band. Breckenridge and Hosler investigated reduced rutile TiO_2 single crystals and found activation activation energies between 10 meV and 94 meV in the referred temperature range under different reducing conditions [171]. Similar activation energies were found for bulk Magnéli-phases. For comparison, conductivity vs temperature curves of bulk Magnéli-phases Ti_nO_{2n-1} were digitized from Inglis et al. [119] and the extracted activation energies are plotted in figure 5.8(b) as a function of the oxygen deficiency with respect to stoichiometric TiO_2. From this graph it can be clearly seen that the activation energy decreases with increasing oxygen deficiency of the TiO_{2-x} phase. The energy values match well the experimen-

tal results of the crystalline TiO_{2-x} device series. Interestingly, similar activation energies from 38 meV up to 88 meV were found in TiO_2 ReRAM devices in the ON state [168, 172]. From this point of view, crystalline thin films with an amount of reduced rutile phase are quite interesting since Magnéli-phases were found to be important for resistive switching. This may give a second hint that Magnéli-phases are already present in the ALD grown TiO_{2-x} thin films besides the fact that also the signal of much more oxygen deficient Ti_2O_3 with respect to stoichiometric TiO_2 was found by Raman spectroscopy.

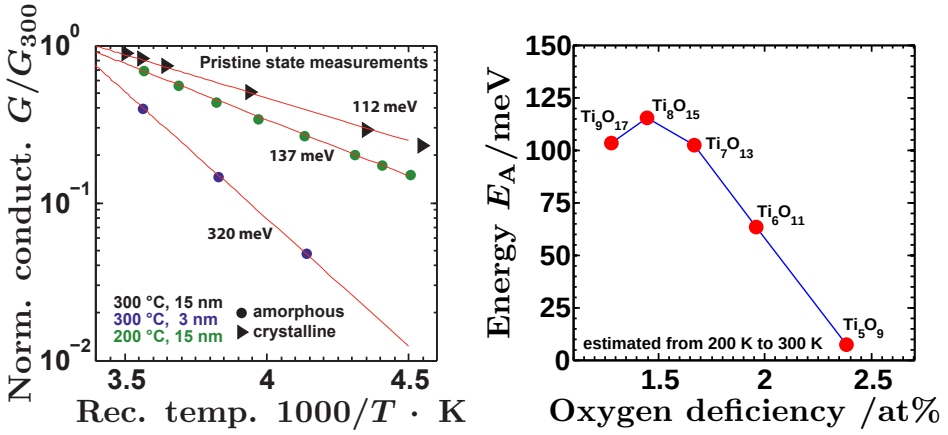

(a) (b)

Figure 5.8: (a) Logarithmic plot of the normalized conductivity vs the reciprocal temperature of ultrathin and thick TiO_{2-x} devices of different crystallinity. (b) Activation energy of the conduction of Magnéli-phases dependent on the their stochiometry in the range from room temperature down to 200 °C. Activation energies were determined by digitization of the original graphs in [119].

5.3.1.1 Thin Film TiO_{2-x} ReRAM at Low Electric Fields

On the one hand the low values of the activation energy indicate the presence well-conducting phases in crystalline TiO_{2-x} and shallow defects in amorphous TiO_{2-x}. On the other hand, electric field dependent effects have to be elucidated to identify the transport mechanism before electroforming takes place. Generally, the conduction behavior was found to be field dependent. In the following it has to be distinguished between low electric fields up to around $1.5 \cdot 10^8$ V/m and higher electric fields above. In the low field range, several conduction mechanism discussed in section 5.2 can be ruled out. Beyond these are the Fowler-Nordheim tunneling, trap-assisted tunneling, classic Poole-Frenkel effect, and SCLC. The dependencies 5.3, 5.5 which addresses the tunneling effects does not occur. SCLC can be fully ignored at low fields due to a lack of a the minimum required exponential factor in the log(j)-log(U) plot as listed in table 5.2. The calculated dielectric permittivity derived from classical Poole-Frenkel plot was by an order of

5 unreasonably higher as compared to the values found in chapter 3. However, for all fabricated TiO_{2-x} devices, except the highly insulating 3 nm thin TiO_{2-x} grown at 200 °C, the current density is a hyperbolic function of the electric field as depicted in figure 5.9.

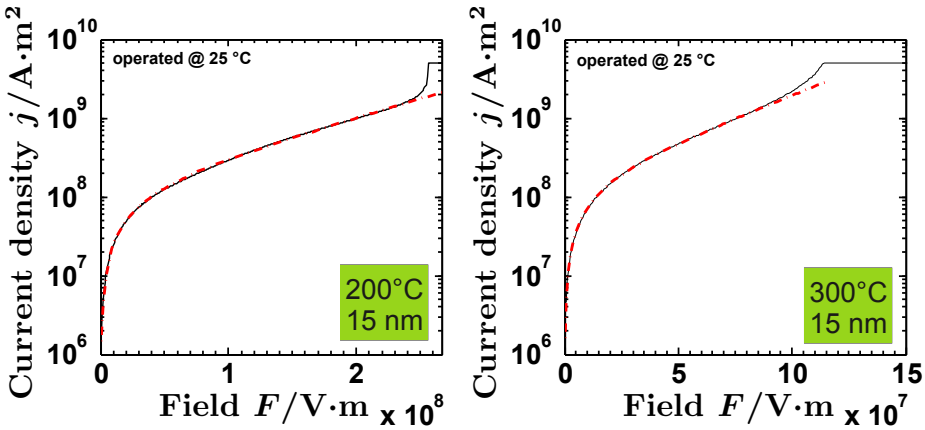

(a) (b)

Figure 5.9: Logarithmic plot of the current as a function of the electric field for an amorphous device in (a) and crystalline device in (b). In both cases the current follows a hyperbolian sinus function dependent on the electric field.

From equations 5.45, 5.59 it seems to be reasonable, that either Multi Center Poole-Frenkel or the two site small polaron hopping conduction are dominant at low electric fields. Multi Center Poole-Frenkel mechanism for semicrystalline host 5.45 may explain both, transport in the crystalline as well as in the amorphous MIM devices. The existence of polarons is linked to the presence of a crystalline lattice. Thus, the conduction in crystalline TiO_{2-x} devices may originate from small polarons as well. The hopping distance can be directly determined from the IV sweeps using equations 5.45, 5.59, exemplary shown in figure 5.9. Table 5.1 gives an overview over the obtained values for the parameter s. It can be clearly distinguished between the hopping distance in amorphous TiO_{2-x} and in crystalline TiO_{2-x}, with values about 0.7 nm and 1.5 nm, respectively. This is reasonably, because highly, locally disordered TiO_{2-x}-complexes in the amorphous state are reconfigured to the regular crystalline long-range order. Thus, the inter-distance from defect to defect in TiO_{2-x} is influenced by the structure of the amorphous state. In the crystalline host material the inter-distance is higher whether the transport is described by the Multi Center Poole Frenkel model, or by localized electrons in the small polaron model. Equations 5.45, 5.59 contain more information than only the hopping parameter. The defect density or possible small polaron density can be calculated from the attempt to escape frequency or small polaron hopping frequency ν, in addition. In case of the small polaron model, this number is directly accessible by the Debye temperature [167, 173]. The Debye temperature of rutile TiO_2 was estimated between 530 K to 780 K [174, 175, 176]. Thus, the hopping frequency is

approximately $1 \cdot 10^{13}$ Hz. The attempt frequency in the Multi Center Poole-Frenkel model is given indirectly by 5.45. The attempt frequency times the site to site hopping distance equals the charge carrier velocity. From that, the attempt frequency $\nu = F/s \cdot \mu$ can be determined from the charge carrier mobility at a given electric field of $7.5 \cdot 10^7$ V/m in case of weak fields. The electron mobility of oxygen deficient TiO_{2-x} thin films was determined as 0.57 $cm^2/(Vs)$ by measurements on transistor channels, and similarly, thin films grown in the anatase phase exhibit a value of 1.02 $cm^2/(Vs)$ [177]. In single anatase crystals the mobility was found to be approximately 1 $cm^2/(Vs)$ [178]. Terahertz-time domain spectroscopy on single crystalline rutile TiO_2 revealed mobilities of 0.2 to 0.6 $cm^2/(Vs)$ dependent on the crystals' orientation [179, 180, 181]. Breckenridge and Hosler thoroughly investigated the conduction of reduced rutile crystals for which the mobility varied between around 0.01 - 0.1 $cm^2/(Vs)$ [171]. In summary, a wide range of mobilities from 0.01 up to 1 $cm^2/(Vs)$ is reported. From that, the attempt frequency for hopping from site to site can be derived between $1 \cdot 10^{11}$ s^{-1} (small mobility) to $1 \cdot 10^{13}$ s^{-1} (high mobility) for the assumed electric field of $7.5 \cdot 10^7$ V/m. For simplicity and comparison, a frequency of $1 \cdot 10^{13}$ s^{-1} was chosen as in the small polaron hopping model. The calculated defect density N_a and the activation energy from deep temperature measurements are given in table 5.1. In amorphous TiO_{2-x} devices the defect density tends to increase from approximately $1 \cdot 10^{24}$ m^{-3} by about one order of magnitude with increasing TiO_{2-x} thickness. The higher defect density might be attributed to a change of the heterogeneous growth interface while the layer by layer growth mode, which changes from Pt to amorphous material. The validity of multiple site to site conduction can be qualified by calculating the critical defect density. As input in equation 5.39, the average electric field ($7.5 \cdot 10^7$ V/m) and the optical dielectric permittivity is needed. The static dielectric permittivity was shown to tend to 5 in chapter 3.Thus, the critical defect density in figure 5.5 is approximately $2 \cdot 10^{25}$ m^{-3} which matches the experimentally derived defect density of about $2.5 \cdot 10^{25}$ m^{-3} well. Inserting a mobility of 0.57 $cm^2/(Vs)$ for reduced amorphous TiO_{2-x} thin films [177] for the attempt frequency ($5 \cdot 10^{12}$ Hz) leads to a defect density of $5.0 \cdot 10^{25}$ m^{-3} which is higher than the critical calculated critical defect density. Therefore the Multi Center Poole-Frenkel model for hopping transport by shallow traps in the amorphous matrix is validated.

To infer which model better matches the conduction process in oxygen deficient crystalline TiO_{2-x} is much more complex. The derived defect density of crystalline samples is about a factor 3 smaller than for amorphous thin films at the assumed attempt frequency of $1 \cdot 10^{13}$ Hz. Breckenridge's results on a gently reduced rutile TiO_{2-x} crystal yielded values for the mobility of 0.094 $cm^2/(Vs)$ and a defect density of $5.0 \cdot 10^{24}$ m^{-3} [171]. Such low mobility results in a lower attempt frequency and consequently a higher calculated defect density for crystalline TiO_{2-x}. In numbers the average calculated density of $6.0 \cdot 10^{24}$ m^{-3} ($1 \cdot 10^{13}$ s^{-1}) increases to $6.0 \cdot 10^{25}$ m^{-3} ($1 \cdot 10^{12}$ s^{-1}) which matches the defect density reported in Breckenridge's work. From this comparison, the Multi Center Poole-Frenkel mechanism for field-directed emission into a semicrystalline host material can also explain the found field dependent conduction in crystalline TiO_{2-x}.

Nevertheless, the polaron related model has to be elucidated, too. The most crucial issue in the polaron model is the critical field strength at which the small polaron will dissociate. The

critical field strength can be computed from the measured activation energies. The activation energies of 42 and 112 meV at a given hopping distance of about 1.5 nm allow to compute the critical field strength, i.e. $1.1 \cdot 10^8$ V/m (25 nm thick TiO_{2-x}) and $3.0 \cdot 10^8$ V/m (15 nm thick TiO_{2-x}), respectively. In case of 25 nm thick TiO_{2-x} a decrease of the current density would be theoretically expected, but at such a critical field strength the samples already underwent electroforming in practice. From this no information about the validity of the adiabatic small polaron hopping model could be concluded. The most striking concern is that such low activation energies were never reported for polarons in the measured temperature regime in TiO_{2-x}. The lower limit reported for TiO_2 is 0.2 eV [169], so far.
In summary, the transport in the amorphous TiO_{2-x} can be addressed to Poole-Frenkel conduction at high defect densities, most probably by shallow traps due to the oxygen deficiency consistent with the low activation energy of around 0.13 eV to 0.3 eV. On which phenomena the electrical transport in reduced crystalline ALD TiO_{2-x} thin films relies is difficult to answer. Magnéli-phases may act as dominant host for defect-like transport channels which are cross-linked to each other. Here hopping in the sense of the Multi Center Poole Frenkel model or small polaron motion are discussed to describe the conduction process.

Table 5.1: Overview over site to site hopping distance s and defect density N_a determined from the fitting of the IV-curves of the respective devices using equation 5.45 and 5.59. The activation energies E_a used for determination of N_a were taken as determined from temperature dependent measurements (sec. 5.3.1).

TiO_{2-x} device properties			T meas.	s	N_a	E_a
thickness	growth temp.	structure				
nm	°C	-	°C	nm	m^{-3}	meV
3	300	a	85	0.47 ± 0.07	$1.0 \cdot 10^{24}$	320
5	200	a	25	0.65 ± 0.03	$7.3 \cdot 10^{23}$	316
5	200	a	85	0.83 ± 0.04	$5.1 \cdot 10^{23}$	316
15	200	a	25	0.57 ± 0.02	$2.5 \cdot 10^{25}$	137
15	200	a	85	0.89 ± 0.02	$1.2 \cdot 10^{25}$	137
15	300	c	25	1.30 ± 0.10	$7.1 \cdot 10^{24}$	112
15	300	c	85	1.55 ± 0.30	$4.7 \cdot 10^{24}$	112
25	300	c	25	1.56 ± 0.20	$6.1 \cdot 10^{24}$	42
25	300	c	85	1.73 ± 0.22	$6.2 \cdot 10^{24}$	42

5.3.1.2 Thin Film TiO_{2-x} ReRAM at High Electric Fields

Thick TiO_{2-x} devices show up to the onset of electroforming no change in the conduction behavior which follows a $j \sim \exp(-\frac{E_a}{kT})\sinh(const. \times F)$ dependence for every thickness. Thin amorphous devices exhibit lower defect densities and higher activation energies. Therefore, the current density is consequently lower. From a characteristic IV graph in figure 5.10 it can be seen that the conduction in thin TiO_{2-x} films is controlled by two mechanism before the onset of electroforming. With increasing field strength the dominating mechanism changes from Multi Center Poole-Frenkel mechanism to a stronger linear field dependent process. All tunneling mechanism were testified, but neither a log(j/F^2) vs log(1/F) plot indicated Fowler-Nordheim tunneling, nor trap-assisted tunneling was found which would be most reasonable for defect-rich TiO_{2-x}. In table 5.2 the slopes from the log(j)-log(U) are tabulated for a 3 nm thin TiO_{2-x} device. Two distinct ambient temperature dependent exponents greater than two were estimated, which could address trap-assisted SCLC, but the temperature dependence was inverse to the expected. The exponents are determined like 6.4 and 11.2 at 25 °C and 85 °C, respectively. According to equation 5.20 the dielectric permittivity can derived from a log(j/F)-$F^{1/2}$ plot. By this, a dielectric permittivity of 29 was found, but that would mean an additional Poole-Frenkel effect coexist. A coexistence would be possible if a clearly distinct second type of trap state exists in the TiO_{2-x}. But the corresponding slope in figure 5.8(a) of the deep temperature measurement is not superimposed by a second slope which would give a hint for a higher activation energy. In addition to that, the optical measurement in chapter 3 revealed a lower dielectric constant. Thus, a second parallel Poole-Frenkel effect does not explain the IV characteristic at high electric fields. From exclusion of all other effects only the assumption of thermal excitation over the Schottky barrier remains.

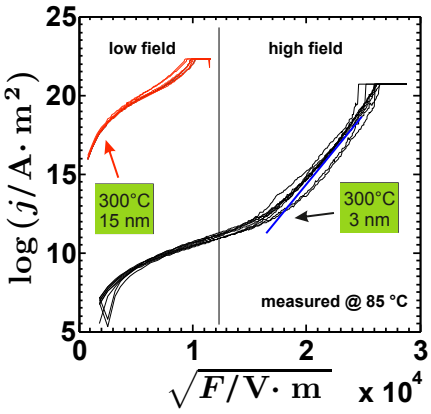

Figure 5.10: Logarithmic I-$\sqrt{F}$ plot of a 3 nm and 15 thick thin film deposited at 300 °C. Above a certain field strength the conduction mechanism differs from the functional hyperbolian description.

Schottky-like behavior was reported for pristine as well as formed TiO_2 ReRAM [16, 182]. In this study, the 3 nm at 300 °C deposited TiO_{2-x} ReRAM reveals a dielectric permittivity of 5.1 ± 0.4 at 25 °C which perfectly matches the optically estimated value of ∼ 5. The derived value of the Richardson constant is only about one order of magnitude underestimated. Such a deviation is regularly observed for different semiconductor materials [183]. The values for the dielectric permittivity as well the Richardson constant decrease significantly for the 85 °C IV curves. This might result from the high ground defect density which is activated with only 320 meV. Increasing the temperature from 25 °C to 85 °C causes a nearly one order of magnitude higher charge carrier density involved in electric transport. Based on theoretical calculations on the influence of the defect density on the Schottky barrier [182], the Schottky type interface may be turned into a more ohmic conducting interface by increasing the electron concentration contributing to the electric transport.

Table 5.2: The results of all possible fitting applied to the different types of TiO_{2-x} thin films are presented. NS: no linear fitting applicable.

mechanism	3 nm amorph, 300 °C		15 nm amorph, 200 °C	15 nm crystalline, 300 °C	temperature / °C
	low field	high field	low field	low field	
Fowler-Nordheim	NS	NS	NS	NS	25/85
trap-assisted tunneling	NS	NS	NS	NS	25/85
reverse Schottky					
ϵ_r	-	**5.1 ± 0.4**	-	-	25
$A^\star$ / $\frac{A}{cm^2K^2}$	-	**12.7 ± 14.2**	-	-	
ϵ_r	-	**1.7 ± 0.2**	-	-	85
$A^\star$ / $\frac{A}{cm^2K^2}$	-	**0.03 ± 0.02**	-	-	
classic Poole-Frenkel					
ϵ_r	-	28.5 ± 2.4	-	$(1.39 \pm 0.07) \cdot 10^6$	25
ϵ_r	-	7.8 ± 0.4	-	-	85
MCPF/SPH					
s / nm	-	-	**0.57 ± 0.02**	**1.30 ± 0.10**	25
$N_A \cdot m^3$	-	-	$\mathbf{2.5 \cdot 10^{25}}$	$\mathbf{7.1 \cdot 10^{24}}$	
s / nm	**0.47 ± 0.07**	-	**0.89 ± 0.02**	**1.55 ± 0.30**	85
$N_A \cdot m^3$	$\mathbf{1.0 \cdot 10^{24}}$	-	$\mathbf{1.2 \cdot 10^{25}}$	$\mathbf{4.7 \cdot 10^{24}}$	
SCLC					
$\frac{T_C}{T} + 1$	1.25 ± 0.30	6.44 ± 0.43	1.04 ± 0.03	1.00 ± 0.00	25
$\frac{T_C}{T} + 1$	1.08 ± 0.06	11.17 ± 0.68	1.02 ± 0.02	1.00 ± 0.00	85

5.3.2 Area Dependence of the Initial State

Thick TiO_{2-x} devices generally showed a higher conductance than thinner TiO_{2-x} films. For devices in the unformed state, one should expect linear increase with increasing device area. In figure 5.11(a) the current is plotted against the logarithm of the device area with different linewidth. The current varied very slowly by about 50 % although the area changed by approximately 2 orders of magnitude. This surprising finding might be addressed to parasitic lateral conduction through the bulk TiO_{2-x} between crossing device lines may cause this slight variation of the current as schematically depicted in figure 5.11(b).

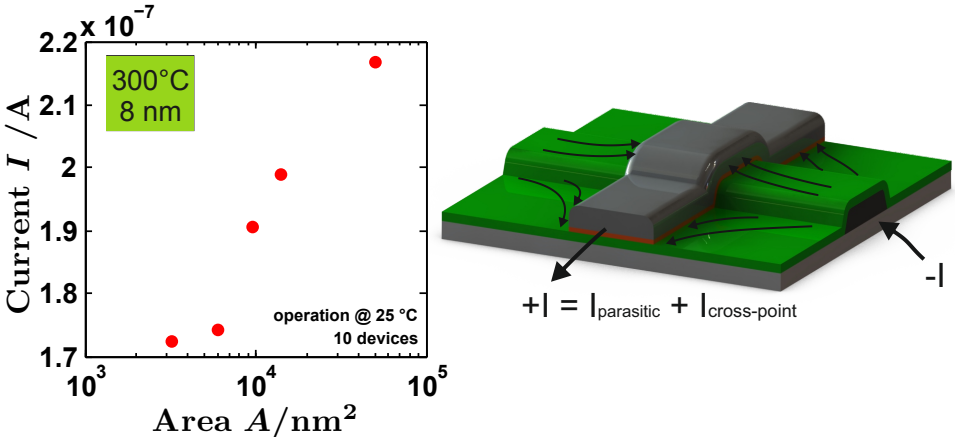

(a) (b)

Figure 5.11: (a) Current vs MIM device area of a 8 nm thick TiO_{2-x} film grown at 300 °C. (b) Model drawing of parasic current flowing laterally through TiO_{2-x} bulk between two crossing electrode lines.

LC-AFM measurements were conducted to demonstrate bulk conduction over the entire bulk of as-deposited films. For that purpose 25 nm thick TiO_{2-x} was deposited at 300 °C on a well-conducting platinized substrate and on insulating SiO_2. The counter electrode of the experiment was connected either to the Pt electrode or was contacted on top of the TiO_{2-x} thin film. Figure 5.12(a) and 5.12(b) show the pseudo color image from both local current measurements. The current was in magnitude of the same order on both samples confirming that lateral conduction in the films is possible.

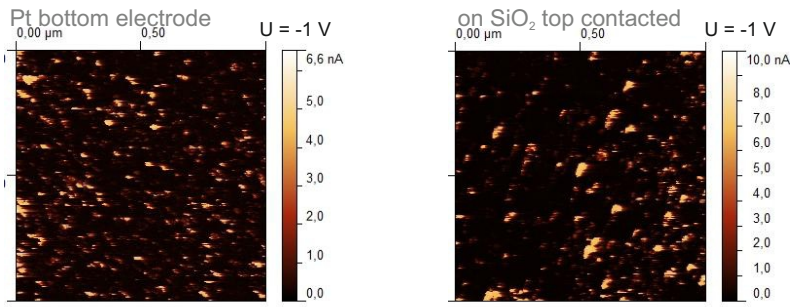

(a) (b)

Figure 5.12: LC-AFM images of 25 nm nano-crystalline TiO_{2-x} deposited on (a) Pt and on (b) SiO_2.

The area dependence and the LC-AFM experiments on crystalline TiO_{2-x} match the theory that well-conducting oxygen deficient TiO_{2-x} phases might be responsible for the increased conductance in the grown crystalline TiO_{2-x} thin films found by the electrical transport investigations. In addition to that, the LC-AFM measurements elucidate that such well-conducting phases may built up a conducting matrix within the grown crystalline TiO_{2-x} which result in parasitic paths which might affect the resistive switching properties.

CHAPTER

SIX

STANDARD NANO CROSS-POINT RERAM

This chapter elucidates the correlation between crystallinity and electroforming and resistive switching on TiO_{2-x} standard cross-point devices. The characterization of the electroforming is presented in the first part. The second part deals with the resistive switching properties of differently grown TiO_{2-x} thin films. This especially addresses the SET voltage to the LRS with respect to the electroforming.

6.1 Electroforming

Foregoing investigations have shown that the electroforming is time consuming or need high voltages which exceeds CMOS compatibility [16, 27, 37, 42]. Since the electroforming is an undesirable extra step in final ReRAM application, the electroforming effort has to be reduced or fully avoided. Thus, a two step electroforming as suggested for Pt|TiO_2|Pt [42] represents no solution in any case. This was successfully reduced to a single step forming process by engineering a Schottky barrier into the device [27]. In devices with Schottky barrier, electroforming of different polarity on TiO_2 leads to the ON or OFF formed states, depending whether a Schottky barrier is positively biased or not, respectively. It has been demonstrated that soft OFF forming of TiO_2 may lead to the coexistence of two resistance modes [184]. One mode is of electronic nature in 8-wise operation, the other incorporates oxygen vacancy drift in counter-8-wise operation. However, the electronically based resistive switching exhibits a significantly lower retention of the OFF state as compared to filamentary-type switching. Reasonably, filamentary-type switching should be favored. The influence of current-driven as well as voltage driven forming on counter-8-wise, filamentary resistive switching of TiO_2 devices was investigated by Nauenheim et. al [27]. Positively biased current driven electroforming with respect to the Schottky barrier was found to be most soft, but this got some drawbacks in final application of TiO_2 ReRAM. On the one hand, the virgin device state cannot be electroformed to a higher resistance state which would correspond 8-wise operation. As a consequence, the switching to the ON

state would be of opposite polarity. On the other hand, the current driven mode has to be implemented on the chip. Therefore, further investigations are needed for an engineered solution to overcome the Schottky barrier. Headed by this requirement, reversely biased electroforming was performed by applying positive voltage to the top electrode of standard nano cross-point (see fig. 4.6). To allow a comparison among all prepared samples, the sweep rate and the maximum voltage where kept constant. Higher voltage was only applied, if the electroforming does not occur under low voltage.

6.1.1 Electroforming of Ultra Thin Amorphous TiO_{2-x} Films

In the last chapter 5 ultra thin, amorphous TiO_{2-x} standard devices were demonstrated to exhibit a Schottky barrier controlled conduction behavior before electroforming takes place. In figure 6.1(a) and 6.1(b) the IV sweeps of the EF of such devices are shown. The electroforming was carried out at a sweep rate of 0.2 V/s from 0 to 3.8 V at two different temperatures. At 25 °C, the 3 nm thin amorphous films deposited at 200 °C could not be formed up to 20 V. Several attempts were undertaken, but no electroforming occurred. Only charging effects could be observed as depicted in figure 6.1(a) which may simply arise from charging the cabling or from the polarization of the dielectric TiO_{2-x} thin film. Increasing the ambient temperature to 85 °C enabled electroforming at 3.0 ± 0.4 V. It seems, that temperature-induced leakage enabled electroforming. Amorphous TiO_{2-x} thin films grown at 300 °C already formed at 25 °C at 2.5 ± 0.2 V. Increasing the measurement temperature to 85 °C lowered the forming voltage to 1.95 ± 0.10 V. Much higher voltages around 12 V were reported for Si|SiO_2|Ti|Pt|TiO_2(33 nm)|Pt devices executing ON-forming [37]. A forming voltage of 5 V on 30 nm thick sputter deposited thin films was determined by Nauenheim et al., although a sweep rate of only 0.038 V/s was applied [27]. Simulation of the electroforming kinetics revealed that higher voltages accelerate electrodegradation of pristine oxides [185]. Thus, low slew rates tend to decrease the forming voltage. From this it might be inferred, that 3 nm thin ALD grown TiO_{2-x} should generally enable to overcome the Schottky barrier at lower voltages as compared to thick sputter deposited TiO_2 thin films. This coincides with observations on only 4 nm thick sputter deposited TiO_{2-x} films in a Si|SiO_2|Ti|Pt|TiO_2|Pt which show low forming voltages [37]. Similarly, the forming voltage of amorphous HfO_x was reported to scale downward with decreasing oxide thickness [24]. To explain the non-forming behavior of the 3 nm thin TiO_{2-x} deposited at 200 °C, the deposition temperature should be further considered. Higher deposition temperatures may lead to the reduction of TiO_2 while the layer by layer ALD growth under reducing Ar flow at low pressure. By this, oxygen vacancies might be created which might result in a lowering of the Schottky barrier [182]. Another possible explanation is a partial reduction by the Ti adhesion layer beneath the Pt bottom electrode at elevated temperatures. Thus, devices from 3 nm thick TiO_{2-x} deposited at 300 °C might exhibit a lowered Schottky barrier as compared to TiO_{2-x} deposited at 200 °C. Furthermore, the current values in 3nm thick TiO_{2-x} devices were partly below the current detection limit and may falsifies the drawn picture, in addition. However, if electroforming takes place in 3 nm thin TiO_{2-x} films, the transition from the conduction mechanism in

the pristine device state to the LRS was always abrupt and lead to a very low resistance state of several kΩ, but still below the stripe resistance [186].

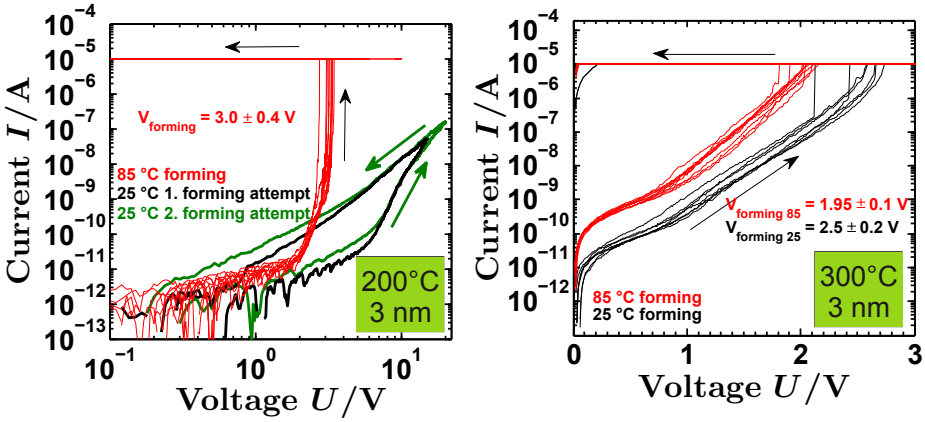

Figure 6.1: Electroforming of 3 nm thin amorphous TiO_{2-x} films. (a) TiO_{2-x} films grown at 200 °C could not electroformed at 25 °C even after second trial up to 20 V. At 85 °C electroforming was enabled. (b) Electroforming of 3 nm thin TiO_{2-x} films grown at 300 °C.

6.1.2 Electroforming of Thick TiO_{2-x} Films

The transport investigations have demonstrated that no effect of a Schottky barrier could be observed in thick TiO_{2-x} films. This is linked to a lower field strength as compared to 3 nm thick amorphous TiO_{2-x} before electroforming took place. The corresponding IV sweeps are shown in 6.2(a) and 6.2(b) for 25 °C and 85 °C ambient temperature. At 25 °C the electroforming in amorphous devices took place at a voltage of 3.8 V which was lowered to 2.8 V when the temperature was increased to 85 °C. Interestingly, abrupt forming could be only found for a temperature of 25 °C, whereas temperature-enhanced conduction caused a softening of the forming behavior which then resulted in a higher LRS state. Soft forming was also observed for the crystalline grown TiO_{2-x} samples independent of the temperature. Although different IV sweeps on the crystalline TiO_{2-x} showed a significant scattering it could be conducted that the forming voltages nearly agreed for 25 °C and 85 °C with 1.7 ± 0.1 V and 1.53 ± 0.06 V, respectively. In total, the measurements demonstrate, that electroforming of crystalline TiO_{2-x} could be carried out at considerable lower voltages as compared to amorphous devices of the same thickness.

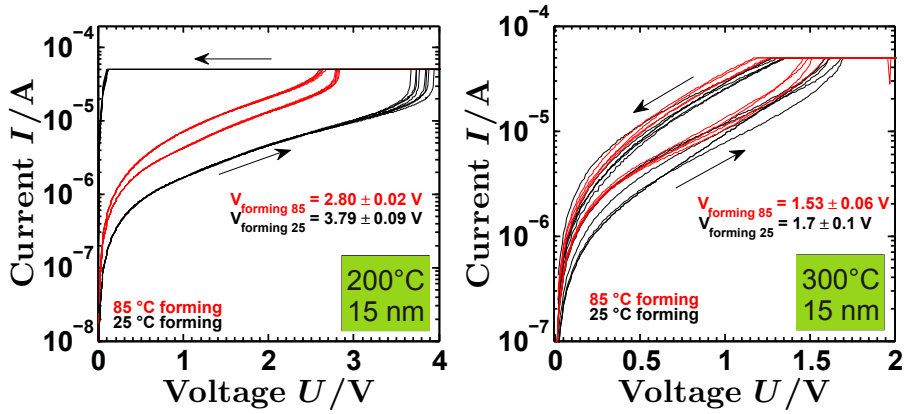

(a) (b)

Figure 6.2: Electroforming of 15 nm thick TiO_{2-x} films at 25 °C and 85 °C . Electroforming of amorphous TiO_{2-x} in (a) was more abrupt at 25 °C and tended to soft forming at 85 °C. Electroforming curves of nano-crystalline TiO_{2-x} in (b) taken at both temperatures superimposed.

6.1.3 Correlation between Crystallinity and Electroforming

The crystallization of the TiO_{2-x} ALD films was demonstrated to occur as transient process initiated at a certain thickness while the deposition. Further deposition of TiO_{2-x} changed the structure of the films from crystallites in an amorphous matrix into a system where crystallization into different phases of TiO_{2-x} happened. Anatase TiO_{2-x} was grown at considerable low thicknesses while thicker films revealed the presence of the rutile phase already at a deposition temperature of 300 °C. Therefore, electroforming was further investigated on samples of different thicknesses of TiO_{2-x} to elucidate the correlation between crystallization and forming voltage. In figure 6.3 all forming voltages are shown as a function of the thin film thickness and ambient temperature while the measurement. The forming voltage increases with increasing thickness and is lowered only by the influence of the temperature. This may convey the impression that the electric field at which forming occurs is constant as expected for the field strength of a dielectric breakdown. But in case of electroforming of amorphous TiO_{2-x} films the proportionality factor between forming voltage and film thickness turns out to be considerably smaller than 1. For films grown at 300 °C even a constant forming voltage of about 2.5 V was found at 25 °C up to 8 nm at which the thin films were fully crystallized. Above 8 nm, the forming voltage of crystalline TiO_{2-x} is slightly decreased and stabilized down to 1.5 V from 15 nm to 25 nm film thickness independent of the ambient temperature. This demonstrates, that at a certain phase composition of the TiO_{2-x} the electroforming is independent of the electric field in contradiction to amorphous grown thin films.

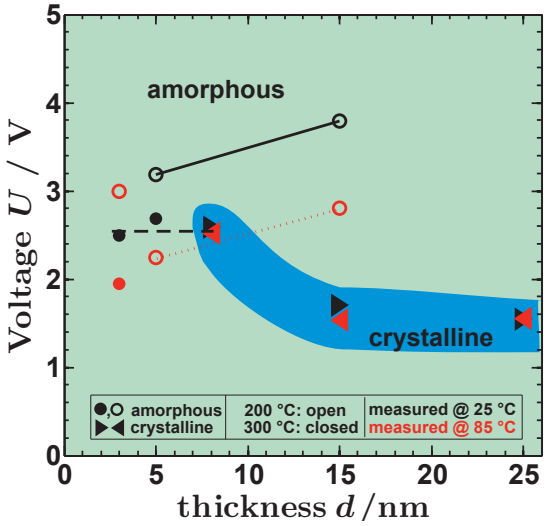

Figure 6.3: Electroforming voltages for different measurement temperatures of achieved TiO_{2-x} films as a function of the thickness. The electroforming voltage stabilizes around 1.5 V with increasing thickness for the crystalline TiO_{2-x}.

6.1.4 Model for Electroforming in TiO_{2-x}

The question arises how electroforming exactly works since the experiments reveal totally different electroforming behavior in amorphous and crystalline TiO_{2-x} thin films. Especially the reduced forming voltage of crystalline TiO_{2-x} films of higher thicknesses is an interesting feature.

From material property point of view, different parameters have to be taken into account. The XPS data revealed that all thin films are oxygen deficient, as described in chapter 3. This was supported by the found conduction mechanism in chapter 5 which additionally allowed to conclude that the defect density in the TiO_{2-x} thin films might increase with thin film thickness as shown for amorphous TiO_{2-x} devices in figure 6.4(a). Furthermore, the hopping distance was determined around a factor two higher with lower activation energies in crystallized TiO_{2-x} thin films as compared to amorphous TiO_{2-x}. The activation energies correspond to the activation energies of Magnéli-phases. LC-AFM measurements demonstrated that 25 nm thick nano-crystalline TiO_{2-x} films grown at 300 °C build up cross-linked well-conducting phases. These might have been already present in 8 nm thick crystalline TiO_{2-x} films which demonstrated a nearly area-independent pristine device resistance at low voltages. This allows to a draw a picture on the defect nature in crystalline TiO_{2-x} as depicted in figure 6.4(c). Thickness dependent crystallization of oxygen vacancy rich TiO_{2-x} films might create a growing network of well-conducting TiO_{2-x} phases. Under these boundary conditions the different electroforming

behavior could be explained. Thin amorphous TiO_{2-x} do not contain enough oxygen vacancies which enable high current densities and the abrupt overcoming of the Schottky barrier might result in the highly conducting LRS after electroforming. By this, a single filament could have been created which connects bottom and top electrode. The filament is known to be of mixed crystalline nature with Magnéli-phases after electroforming [41, 43, 187]. Thus, it might be assumed that amorphous TiO_{2-x} crystallized into Magnéli-phases. Thick amorphous TiO_{2-x} films exhibited an increased oxygen vacancy concentration which helped to overcome the Schottky barrier until soft electroforming of the amorphous material took place. This was achieved in 15 nm TiO_{2-x} at 85 °C. In nano-crystalline TiO_{2-x}, the situation changed fully because several predefined conducting filaments in a conducting network matrix might have existed, as depicted in figure 6.4(d). So, only a very small portion of material with respect to a residual distance of the switching filament has to be electroformed or just an existing path from bottom to top electrode is further transformed into much more higher conducting material. These kind of electroforming might yield in a further reduction of the preferential path by the attraction of oxygen vacancies. The oxygen vacancies might initiate a transformation of the rutile phase into Magnéli-phases or further reduce already existing Magnéli-phases. This assumption is further supported by the fact that the hopping distance is doubled at very low activation energies in crystalline TiO_{2-x} samples as compared to amorphous films. In order to strengthen this theory, an experiment was carried out to destroy such preferential conducting paths. 8 nm and 25 nm standard TiO_{2-x} devices were negatively pre-sweeped and afterward electroformed. The results are shown in figures 6.5(a) and 6.5(b). In 8 nm crystalline TiO_{2-x} films the forming voltage is changed from 2.56 ± 0.58 V to 2.94 ± 0.47 V. The data contain a lot of scatter. Nonetheless, it could be inferred, that conducting paths were broken. This was even more obvious if 25 nm TiO_{2-x} was negatively pre-sweeped. The dashed line in figure 6.5(b) strongly deviates from continuously electroforming on a different device. This non negatively pre-sweeped device only exhibit a forming voltage of around 1.5 V, whereas more than 4 V were necessary to electroform the negatively pre-sweeped device.

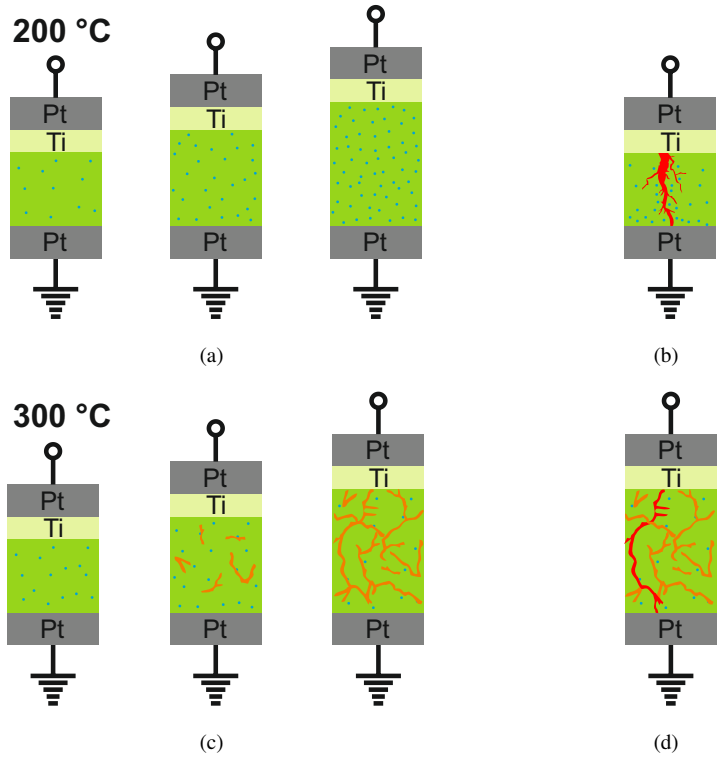

Figure 6.4: Models for the defect states of different ALD TiO_{2-x} films grown at 200 °C (a) and 300 °C (c). Crystalline films grown at 300 °C develop a nano-crystalline conducting network. The corresponding forming models are shown in (b) and (d), respectively.

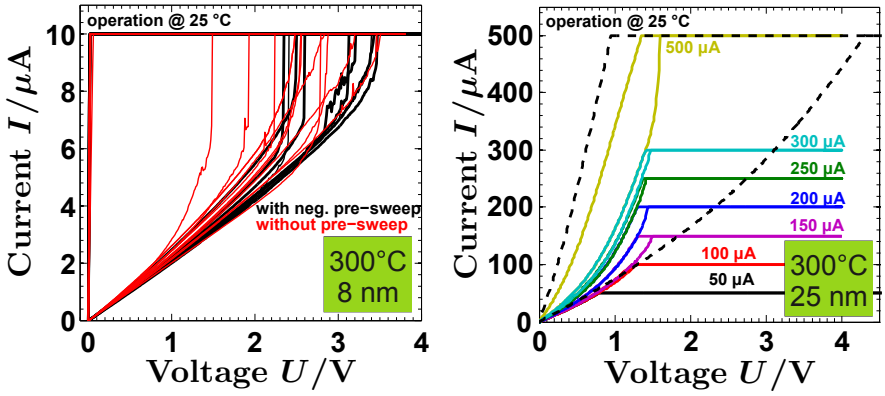

(a) (b)

Figure 6.5: (a) Influence of negative pre-sweep (red curves) on electroforming (black curves) in 8 nm thick crystalline TiO_{2-x}. (b) Two 25 nm thick crystalline TiO_{2-x} devices were electroformed. Black dashed represents a negatively pre-sweeped device, the solid lines show subsequent forming curves on another device.

In summary, amorphous TiO_{2-x} standard devices showed predominantly hard forming at high voltages which could be consistently described by the creation of conducting filaments consisting of Magnéli-phases. In crystalline devices such hard forming is not necessary since the presence of a well-conducting crystalline network enables soft forming accompanied by strongly reduced forming voltage.

6.2 Quasi-Static Switching of Electroformed TiO_{2-x} Films

The electroforming experiments revealed that the thickness and the crystallinity does strongly influence the forming voltage of the TiO_{2-x} based crossbar devices. Thus, the question arises, if these device properties also have an impact on the resistive switching properties.

6.2.1 Thin TiO_{2-x} Films

The electroforming experiments on Si|SiO_2|Ti|Pt|TiO_{2-x}|Ti|Pt structures revealed that the Schottky barrier in ultra thin devices could be overcome under reverse bias which resulted in LRS of several kΩ. Therefore, in general the first RESET required higher currents as compared to the following resistive switching hysteresis as depicted in the insets of figures 6.6(a) and 6.6(b), respectively. Besides that, the amorphous TiO_{2-x} thin films needed higher forming voltages. The devices could be SET by only 50 μA and needed RESET currents of about 70 μA. Compared to other passive nano cross-point devices, these SET and RESET currents are quite low. For example, 8 nm and 25 nm thick amorphous TiO_2 devices were reported to require a SET current of 200 μA to 250 μA and 300 μA for the RESET operation, respectively [34, 188]. Even lower currents of around 10μA were achieved on 30 nm thick TiO_2 utilizing 1T1R structures which enable better control over the current compliance [189]. Thus, in contrast the 3 nm thin passive Si|SiO_2|Ti|Pt|TiO_{2-x}|Ti|Pt devices in this work enabled low current switching without any further control. Such low currents were accompanied by intermediate LRS values as shown in figure 6.6(c). Overall, the resistive switching properties of the thin TiO_{2-x} thin films deposited at different temperatures showed no difference as is depicted in table 6.1, except the forming voltage. This allows to conclude that just the electroforming process shows significant differences in voltage and RESET process while the resistive switching in these devices from amorphous TiO_{2-x} films, although grown at different ALD temperatures, is characterized by similar values. Interesting for device application aside a low switching power is the high value of the DC non-linearity of about 10.[1]

[1] The DC non-linearity differs from the estimation of the non-linearity by the RESET pulse $\mathrm{non-linearity} = \frac{I(U_{\mathrm{RESET}})}{I(U_{\mathrm{RESET}}/2)}$. This procedure can cause problems for continuous IV sweeps because the current response at fixed maximum voltage may already correspond to an IV function of the HRS or in between. But the non-linearity is a measure of the RESET process. Hence, the voltage at the maximum $|\frac{dI}{dU}|$ has to be taken as the RESET voltage and the DC non-linearity can be extracted from the RESET sweep.

Table 6.1: Resistive Switching parameters of 5 nm and 3 nm thin TiO_{2-x} deposited at 200 °C and 300 °C, respectively.

parameter	5 nm TiO_{2-x}, 200 °C	3 nm TiO_{2-x}, 300 °C
I_{CC} / μA	50	50
U_{SET} / V	0.85 ± 0.08	1.16 ± 0.14
DC non-linearity	11.1 ± 4.2	9.2 ± 2.2
R_{OFF}/R_{ON}	≈ 5	≈ 5

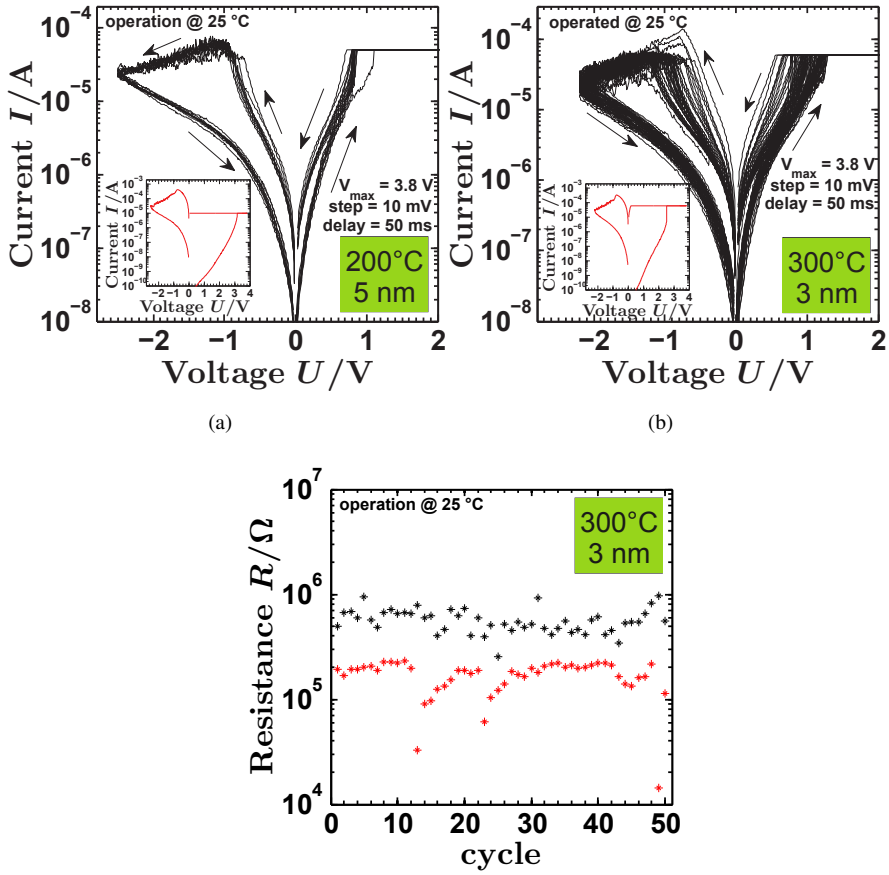

Figure 6.6: Resistive Switching of thin TiO_{2-x} films grown at 200 °C (a) and 300 °C (b). The electroforming curves are shown in the insets. (c) Corresponding memory window to switching hysteresis in (b).

6.2.2 Thick TiO_{2-x} Films

Several authors reported on the resistive switching behavior in reduced, crystallized TiO_2 films after electroforming [41, 187, 188]. In this work electroforming voltages were generally found to be lower in crystalline TiO_{2-x} as compared to amorphous TiO_{2-x} (see section 6.1). Hence, it is highly interesting to compare the resistive switching of amorphous and crystalline TiO_{2-x} as shown in figure 6.7(a) and 6.7(b), respectively. As already discussed, thick amorphous thin films needed a high forming voltage to enable resistive switching. But in contrast to the thin amorphous films the SET process of thick films took place at much lower voltages, a little above 1 V. In contradiction to that, SET and electroforming voltage in crystalline TiO_{2-x} films agree in a comparable experiment in figure 6.7(b), although the IV characteristic of pristine crystalline TiO_{2-x} does not fully matches the resistive switching curve. The same IV sweeps were repeated with lower current compliances as shown in figure 6.7(c) which reproduced the found behavior. The resistive switching measurements, whether on amorphous or crystalline thick TiO_{2-x} films, exhibit non-linear back-sweeps after the SET process. Interestingly, the exact non-linear behavior was directly observed in crystalline TiO_{2-x} after electroforming. Amorphous TiO_{2-x} tends to more ohmic behavior after electroforming. This may elucidate the general trend that soft forming nearly agrees the resistive switching in TiO_{2-x}.

6.2.3 Influence of the Switching Parameters

The comparison between resistive switching properties of the amorphous and crystalline phase of TiO_{2-x} has to be considered carefully, since electroforming and resistive switching with different parameters can influence the device properties [190]. Most striking effects were found for the SET current compliance and the RESET voltage while quasi-static resistive switching. Higher current compliances lead to lower resistance states while the SET process, as exemplary depicted in figure 6.8(a) and 6.8(b). As consequence, the maximum RESET current became a function of the SET current compliance. In this experiment, the RESET current depended exponentially on the SET current.
In contradiction to that, linear behavior was estimated for numerous materials such as NiO, TiO_{2-x}, $ZrO_x|HfO_x$, and HfO_x[190]. The difference might be attributed to the different nature of the ON state, revealing a linear IV dependence or in the case discussed here, a non-linear IV curve. In addition to that, the taken IV hysteresis demonstrates another effect by the SET current compliance: increasing the current compliance decreases the SET voltage. This might be explained by the effect, that a higher current compliance causes a lower LRS state which may be not fully reseted at the given switch OFF parameters. Thus, the RESET has to be readjusted, but this will change the characterization conditions, again. A second concern which blackballs readjustment maybe that high RESET voltages could induce a second electroforming step with opposite polarity and totally change the system. Reasonably, the effect of lowering the RESET voltage from its maximum needs to be investigated. In figure 6.8(c) such a variation is depicted,

and its effect on the HRS and LRS is shown in figure 6.8(d). Obviously, changing the RESET voltage to -1.6 V is already not low enough to reset the device. But small variations, i.e. between -2.5 V to -2.35 V, did not change the resistance states and the SET voltage much. Therefore, within this range of the RESET voltage comparative studies could be carried out.

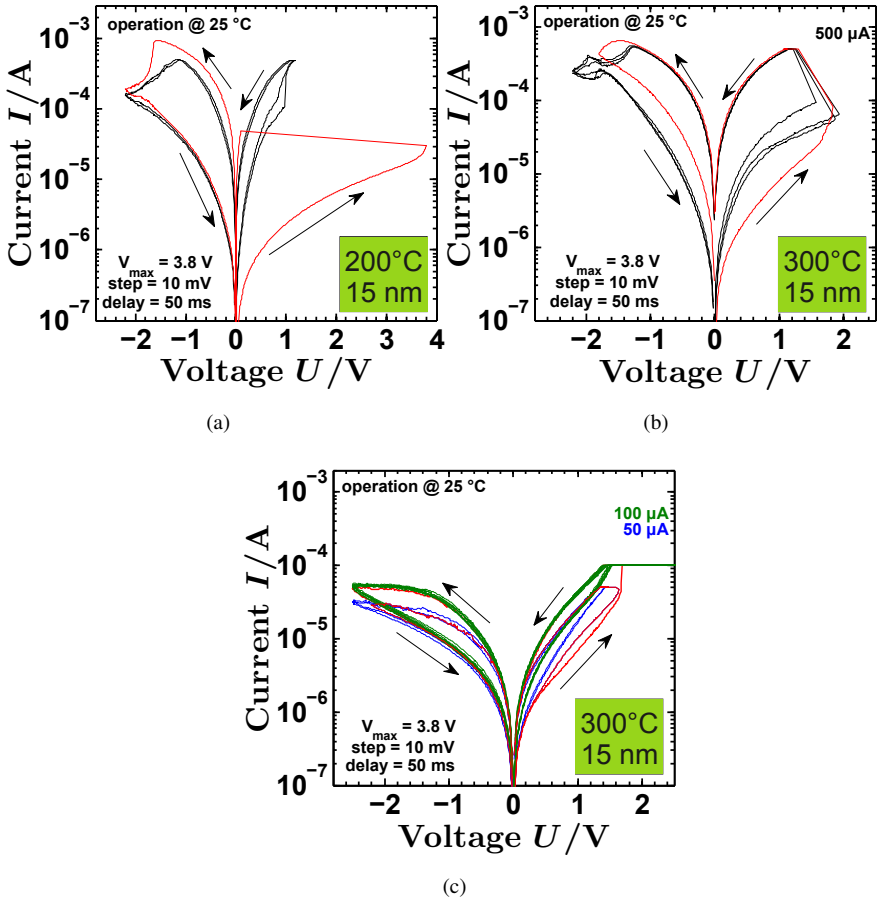

Figure 6.7: Resistive Switching of thick amorphous (a) and crystalline (b) TiO_{2-x} films. High current compliances are needed to achieve a difference in the current response for the LRS and HRS. In (c) the resistive switching at lower SET current compliance is depicted for the crystalline sample. The forming voltage and the SET voltage nearly agree for the nanocrystalline sample in (b),(c)

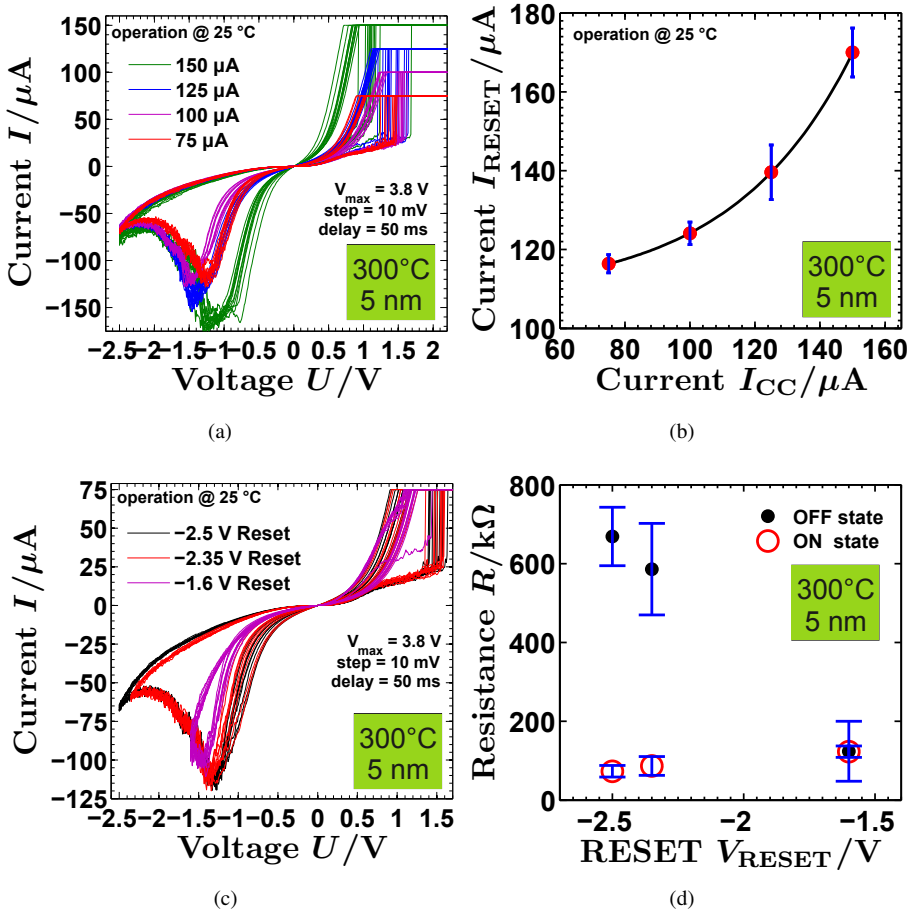

Figure 6.8: Variation of the resistive switching of a single device dependent on the switching parameters. (a) Variation of the resistive switching hysteresis on the SET current compliance. (b) Maximum RESET current as a function of the SET current. (c) The change in the hysteresis curve with decreasing RESET voltage. 6.8(d) The impact of RESET voltage on the resistance state for the hysteresis curve in 6.8(c).

6.2.4 Comparative Study on Amorphous and Crystalline TiO_{2-x} Films

It has been already demonstrated, that amorphous TiO_{2-x} films electroform at higher voltage as compared to crystalline TiO_{2-x}. Thick, nano-crystalline TiO_{2-x} films were partly switched at voltages which are identical to the forming voltage. Nonetheless, this needs to be further analyzed since the switching parameters influence the found read out parameters like the SET voltage, and the LRS as well as the RESET process. Therefore, a thoroughly investigation on the switching properties was carried out at fixed parameters. The same sweep rate and maximum voltages were chosen to qualify the influence of the crystallinity of TiO_{2-x} on the resistive switching. For that purpose, only TiO_{2-x} films deposited at 300 °C were taken which showed the transition from the amorphous to the crystalline phase. The measurements were carried out after several IV hysteresis were passed through. The forming and SET voltage, the LRS and HRS state were taken, and the non-linearity was calculated. In figure 6.9 all determined SET and RESET voltages a plotted as a function of the TiO_{2-x} thickness. In hard formed amorphous TiO_{2-x} devices, here 3 nm and 5 nm, the forming voltage is always higher than the SET voltage of about 1 V. With onset of crystallization at 8 nm the SET voltage increases while the forming voltage decreases. This is accompanied by a scatter of both voltages which may result from not fully nano-crystallized TiO_{2-x}. For these samples, only weak non-linearity after electroforming was observed. Finally, in 15 nm thick devices the forming and the SET voltage agree. Furthermore, 25 nm thick nano-crystallineTiO_{2-x} films were analyzed, too. But such films do not exhibited any switching behavior at the given current compliance.

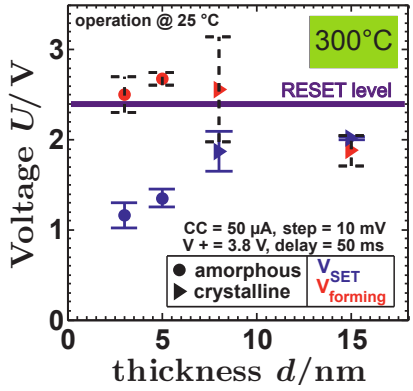

Figure 6.9: Dependence of forming and SET voltage on the thickness of TiO_{2-x} grown at 300 °C. The forming voltage of crystalline TiO_{2-x} agrees with SET voltage independent of the temperature.

In figure 6.10(a) the impact of the crystallinity on the memory window along the crystallization series is depicted. At the chosen SET current compliance, the memory window shifts continuously with the TiO_{2-x} thickness as long as the devices were hard formed. This is reason-

able because the pristine device resistance continuously decreases as well as with the thickness. If the TiO_{2-x} is crystalline, the softforming does not allow a strong jump to lower resistance states and the device stabilizes to an intermediate ON state which is only a factor ~ 1.5 lower than the OFF state. Similarly, the non-linearity is influenced. Previous discussion on resistive switching of ultra thin devices revealed, that very low RESET currents can be achieved. That means the LRS can be rapidly switched off as a function of the RESET voltage. This is not the case of thicker devices, which generally show a better conduction as a function of the electric field as already proved in the last chapter. Since switching in TiO_2 is filamentary, the resistive switching phenomena is only linked to a single filament but not to the remainder field-directed conduction mechanism in the MIM structure. This behaves as an additional parasitic path parallel to the switching filament. Reasonably, the non-linearity of an isolated filament cannot be determined as long as such a parasitic path exists. As a consequence, the non-linearity in a device is shifted to lower values with increasing thickness caused by the better conduction as compared to the conduction of 3 nm devices. The 3 nm thick devices are less influenced by such an effect, because it has been shown that a Schottky barrier has to be overcome and broken to actively create a switching filament. In addition to that, the parasitic current paths across the electrode lines may influence the non-linearity in the same way. But the electric field from line to line is lower as compared to the field which drops over the MIM structure. This has to be only taken into account in very thick TiO_{2-x} devices. This will be discussed in the next chapter.

Overall the investigation on the electroforming and the resistive switching of standard TiO_{2-x} ReRAM devices revealed that the Schottky barrier can be lowered by a sufficiently high defect concentration whether the thin films are amorphous or crystalline. In ultra thin, amorphous films the presence of defects generally helps to reduce the Schottky barrier to allow electroforming at the same condition which are used for the quasi-static characterization of TiO_{2-x} standard ReRAM. Crystalline thin films exhibit as-deposited well-conducting TiO_{2-x} phases which build up pre-defined conducting channels. These channels can be easily electroformed with the same voltage which is needed for the switching itself. Only the initial IV curve does not fully agree to the resistive switching hysteresis in crystalline TiO_{2-x}.

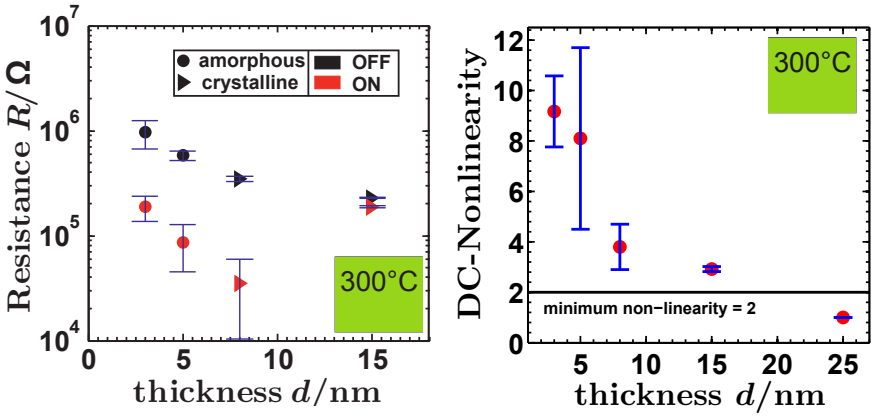

(a) (b)

Figure 6.10: (a) ON and OFF state dependent on the thickness of standard TiO_{2-x} ReRAM . (b) Scaling of the DC-non-linearity with device thickness.

CHAPTER

SEVEN

FORMING-FREE NANO CROSS-POINT DEVICES

Forming-free ReRAM is one of the main aims in research. Some of the TiO_{2-x} films discussed before exhibited a large potential to achieve this aim. Therefore, the obtained results on ALD process control, the thickness and morphology influence on the electrical properties of TiO_{2-x} were comprised, and a strategy was developed to technologically overcome the electroforming. The idea and realization are described in this chapter. The general mechanism of forming-free TiO_{2-x} ReRAM is investigated and its transport properties briefly compared to standard devices in the pristine, OFF, and ON state. Finally, a model on the working principle of the forming-free TiO_{2-x} is suggested.

7.1 Route to Forming-free TiO_{2-x} ReRAM

In the previous chapters the electrical properties and the resistive switching of TiO_{2-x} films were discussed. Well-conducting crystalline TiO_{2-x} devices exhibit very low activation energies of the electrical transport and high oxygen defect densities in a mixture of the anatase and rutile phase. The rutile structure can act as host for extended defects and second phases of titanium oxide material with O/Ti stochiometry smaller than 2 (see fig. 3.17(b)). This is known to lead to the presence of the Magnéli-phases Ti_nO_{2n-1}. The transport measurements discussed in chapter 5 clearly revealed that the activation energy values of ALD grown crystalline TiO_{2-x} range in the same order like for the bulk Magnéli-phases. Similarly, this work already demonstrated that such well-conducting phases lead to a soft forming behavior which is nearly identical to the resistive switching IV hysteresis, afterwards. In literature Magnéli-phases were demonstrated to be involved in the resistive switching phenomena in TiO_2. From these findings it could be concluded that the above described ALD TiO_{2-x} thin film devices might possess an ready-to-use resistive switching state after processsing, i.e. without the need of an additional electroforming step. But what seems to be good for resistive switching in TiO_{2-x} at a first sight caused two parasitic current paths which resulted in undesirable high switching currents, low non-linearity, and

a low resistance ratio. The first path was attributed to conduction across the cross-point electrode lines. This could be eliminated by changing the strategy in device preparation as described in chapter 4. The second severe sneak path was identified as the field dependent conduction in TiO_{2-x} sandwiched between the metallic electrodes. In case of crystalline TiO_{2-x} films these sneak path might be attributed to parallel filaments revealed by the LC-AFM measurements in chapter 5 (see sec. 5.3.2). In summary, a design of forming-free ReRAM cells would have to deal with two contradicting issues: on the one hand resistive switching requires the oxygen deficient rutile phase to establish conducting paths; on the other hand highly conducting phases will prevent good resistive switching performance. Practically, one would try to transform such phases to less conducting ones. This might be done by oxidation which requires an extra process step and the control is rather difficult. A more elegant way to achieve forming-free devices might be the initial destruction of conducting paths in the whole conducting cell matrix by means of an initial IV RESET sweep.

7.2 Electrical Characterization

The processing of the forming-free devices is described in detail in chapter 4. Here the electrical characteristics of these cells will be discussed and compared with the results on the standard cross-point cells. In the first step, the initial resistance across randomly chosen devices was analyzed as described in chapter 5. From this, the uniform initial resistance distribution depicted in figure 7.1 ensured that the changed fabrication process did not only create single forming-free TiO_{2-x} ReRAM devices due to process irregularities.
The resistive switching was analyzed with the same parameters as compared to standard ReRAM, but the DC sweep was started with negative polarity with counter-8-wise operation in order to break initially existing filaments or to initiate a defect separation within the conductive matrix. This results in a initial RESET of the pristine forming-free device as shown as red hysteresis curve in figure 7.2(a). The red hysteresis curve is nearly identical to the subsequent sweeps demonstrating the functionality of the engineered forming-free TiO_{2-x} ReRAM. The according memory window was ≥ 10 which is high enough to distinguish between the LRS and HRS at a SET current of only 100 μA in figure 7.2(b). This improvement of the resistance ratio in the forming-free TiO_{2-x} devices as compared to standard TiO_{2-x} ReRAM devices was attributed to the successful elimination of the parasitic paths.

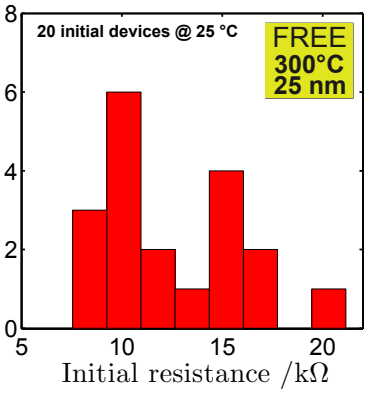

Figure 7.1: Initial state distribution of forming-free TiO_{2-x} ReRAM.

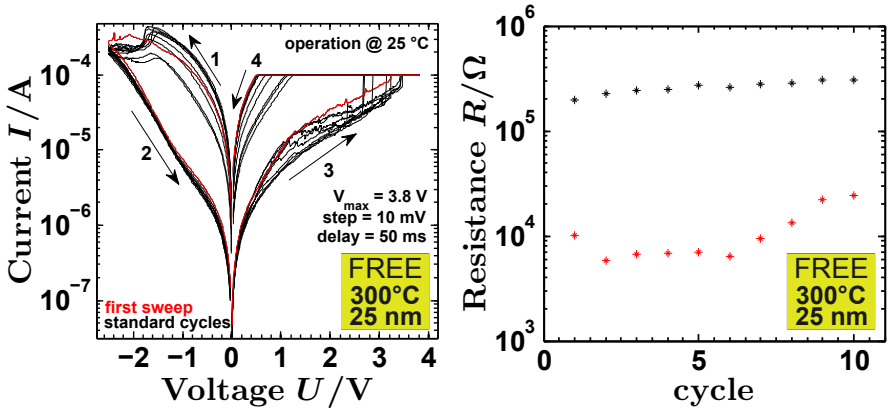

(a) (b)

Figure 7.2: (a) Resistive switching of a forming-free TiO_{2-x} ReRAM device. The red line shows the first sweep starting with an initial RESET of a pristine device from indicated by arrows 1 and 2. (b) Corresponding resistance state taken at 0.1 V for the LRS (red) and HRS (black).

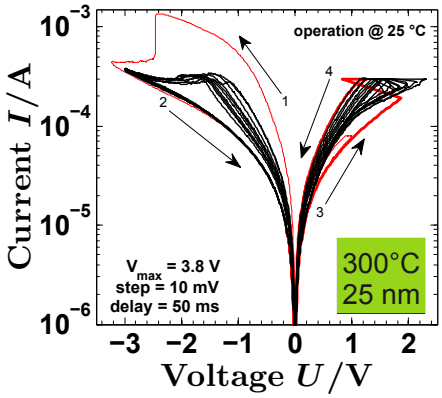

Figure 7.3: Initial RESET of 25 nm tick TiO_{2-x} in a standard device configuration.

7.2.1 Comparison to Standard TiO_{2-x} ReRAM

In order to demonstrate that the cell design is of superior importance for realizing functioning forming-free ReRAM cells, the complementary experiment was conducted on a standard cross-point cell with a continuous TiO_{2-x} layer of comparable composition. The results are shown in figure 7.3. A device was chosen, which exhibits a lower pristine resistance state as compared to the mean value determined in chapter 6. Otherwise nearly nothing would be observable. The red hysteresis curve reveals, that an initial sweep to the OFF state is also possible for standard TiO_{2-x} ReRAM devices. But the subsequent sweeps demonstrate, that the ON and OFF states can nearly not be distinguished. In addition, the device only undergoes a SET process if the current compliance is increased to 300 μA. Compared to the especially forming-free designed devices, the standard devices lack of a good resistance ratio as shown in table 7.1. Initially reseted standard devices exhibit a resistance ratio of around 1.5 whereas forming-free ReRAM allows to achieve a resistance ratio which is one order of magnitude higher. The bad resistance ratio in standard devices origins from the not fully reseted parasitic current path over the continuous film.

Table 7.1: Comparion of achieved resistance switching parameters of standard and forming free TiO_{2-x} ReRAM.

device type	standard 25 nm, nano-crystalline	forming free, nano-crystalline
I_{RESET} / μA	372 ± 7	340 ± 88
U_{SET} / V	1.63 ± 0.25	3.12 ± 0.39
I_{CC} / μA	300	100
DC non-linearity	3.4 ± 2.2	2.8 ± 0.5
$R_{\mathrm{OFF}}/R_{\mathrm{ON}}$	1.5 ± 0.2	29 ± 11
R_{pristine} / kΩ	4.1	10.1
R_{ON} / kΩ	10.3 ± 1.3	11.2 ± 6.7
R_{OFF} / kΩ	15.3 ± 0.3	262 ± 34

7.3 Filamentary Switching and Initial Area-dependent RESET

The observed results on forming-free TiO_{2-x} ReRAM further lead to the question if the type of switching in oxygen deficient ALD TiO_{2-x} films is area-related [12] or is filamentary [40]. An important result is the counter-8-wise operation in forming-free TiO_{2-x} ReRAM device as compared to the standard TiO_{2-x} ReRAM described in chapter 6. Thus, further investigations on forming-free TiO_{2-x} ReRAM were performed which address the area-dependency of the resistive switching behavior.

7.3.1 Simultaneous Switching of Forming-free Devices

A simultaneous switching experiment on two independent forming-free TiO_{2-x} devices was carried out. In figure 7.4 the principle of the experiment is schematically depicted. Two devices were connected by a set of contact tips to a sourcemeter. Four switches can be controlled independently to enable simultaneous IV sweeps either on one or both devices. The read out of each single device state can be done separately in the same manner.

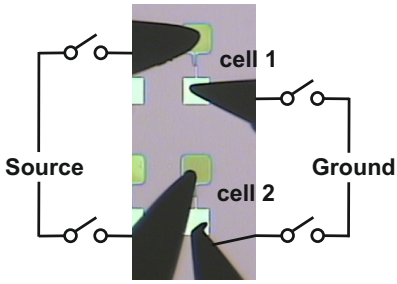

Figure 7.4: Schematical view of the setup for simultaneous resisitive switching. Switches allow the read-out of the single device states.

In a first step an initial RESET sweep was simultaneously applied to both devices as shown in figure 7.5(a). The resistance state of cell 1 and cell 2 were measured by applying a read out sweep up to 0.1 V after each half switching cycle. The respective resistance values are listed in 7.2. From step 1→2 the HRS of cell 1 was a little higher than the HRS of cell 2. Both values matches well the total resistance according to Ohm's law

$$\frac{1}{R_{\text{total}}} = \frac{1}{R_{\text{cell1}}} + \frac{1}{R_{\text{cell2}}} \tag{7.1}$$

which was extracted from the RESET sweep. However, comparing the RESET process of parallely connected devices with a separately reseted device in figure 7.5(b) reveals a two times higher maximum current. Thus, the RESET current depends on total device area. By this, resistive switching in forming-free TiO_2 ReRAM should be area-related, but the subsequent

Table 7.2: Read out states at 0.1 V after half hysteresis loop.

step	state of device / kΩ		
	device 1	device2	device 1+2
1 → 2	139	255	82
3 → 4	38	263	33

simultaneous SET process from step 3→4 revealed only one device was switched on, the other device remained in its HRS. From this it can be concluded that resistive switching in forming-free TiO_{2-x} devices is definitely filamentary-type and no inconsistence to its counter-8-wise operation exist. The resistive switching hysteresis is simply entered from a different point. The device is in a state, which can be treated as a switchable LRS.

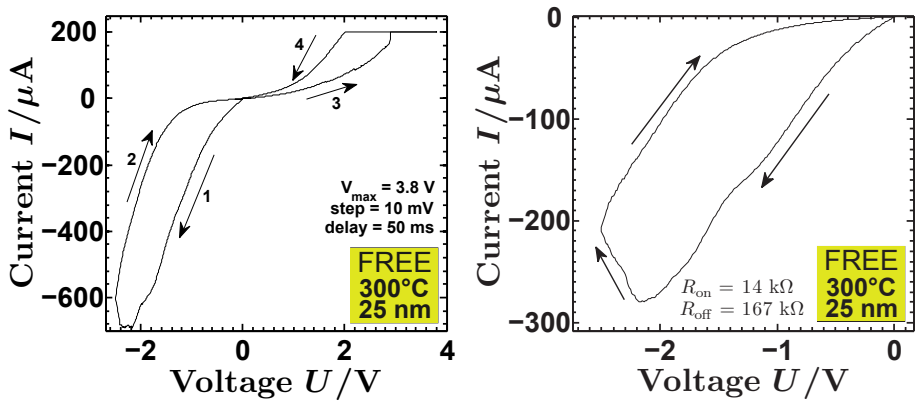

Figure 7.5: (a) Simultaneously RESET and SET of two pristine forming-free devices.(b) RESET sweep on a single pristine forming-free device.

7.3.2 LC-AFM Measurements

Although the simultaneous switching experiments prove the filamentary character of resistive switching, this does not explain the area-dependent RESET operation. The RESET process was further investigated by LC-AFM measurements on 25 nm TiO_{2-x} film with Pt bottom electrode as well as on SiO_2. In step (1) in figure 7.6(a) and 7.6(b) the thin film was reseted on a 1 μm by 1 μm large area at -1.0 V and finally read out at a small value of 0.5 V in step (2). Measurement on both samples show that the RESET process is basically area-related. But the samples do not switch off regularily. Some parts of the thin film reveal particular better conducting TiO_{2-x} structures as their surrounding. As a corollar, the whole material tend to

filament-like conduction. In addition, these filaments built up a conducting network through the thin film since the filament-like conduction can be also observed in TiO_{2-x} on insulating SiO_2.

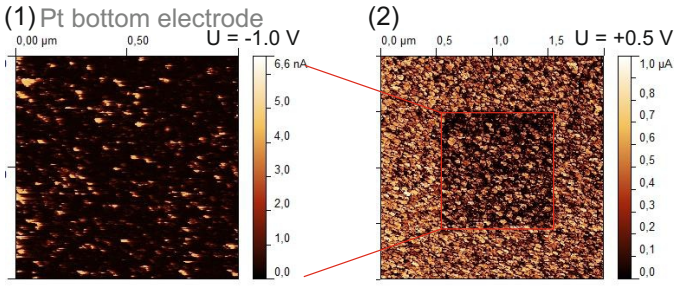

(a)

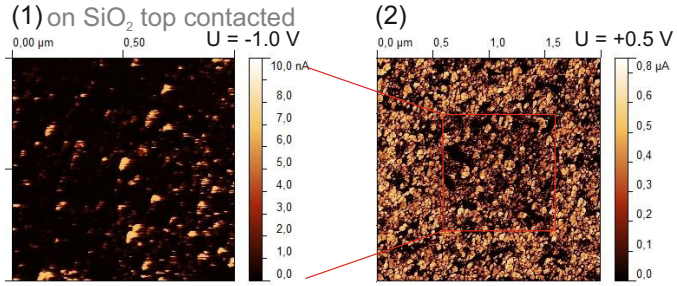

(b)

Figure 7.6: RESET by LC-AFM of pristine 25 nm thick TiO_{2-x} thin film on a Pt bottom electrode in (a) and on SiO_2 in (b). From (1) to (2): Negatively biased RESET of a smaller 1.0 µm × 1.0 µm and read out with small positive bias on a larger area (2.0 µm × 2.0 µm).

7.4 Activation Energy of Conduction

As already discussed in the preceding chapters 3 and 5 Magnéli-phases are better conducting phases of rutile TiO_{2-x}. The measured activation energies in chapter 5 section 5.3.1.1 in combination with oxygen deficiency in partly rutile TiO_{2-x} demonstrated, that by ALD derived TiO_{2-x} may incorporates Magnéli-phases. So, it is of interest to measure the activation energy of conduction before and after destruction of conducting filaments in forming-free TiO_{2-x} devices. In figure 7.7(a) and the normalized conduction vs reciprocal temperature plots of different devices in the pristine and after RESET are shown. The lowest activation energy of 42 meV was observed in pristine TiO_{2-x} devices. The RESET process leads to a higher activation energy of around 97 meV. This supports the idea that resistive switching in TiO_{2-x} thin films is based on the creation and destruction of Magnéli-phases. To finally confirm this idea, the activation en-

ergies of selected standard TiO_{2-x} ReRAM devices were measured in the OFF and ON state in addition to the pristine state. The determined activation energies are given in table 7.3 show that the activation energy of the devices after the SET process is always lower than the pristine, and OFF state as expected. Furthermore, the measurements reveal that the OFF state is always lower than the pristine device state. This is of importance because in standard devices the original pristine resistance state cannot be recovered in contradiction to forming-free devices.

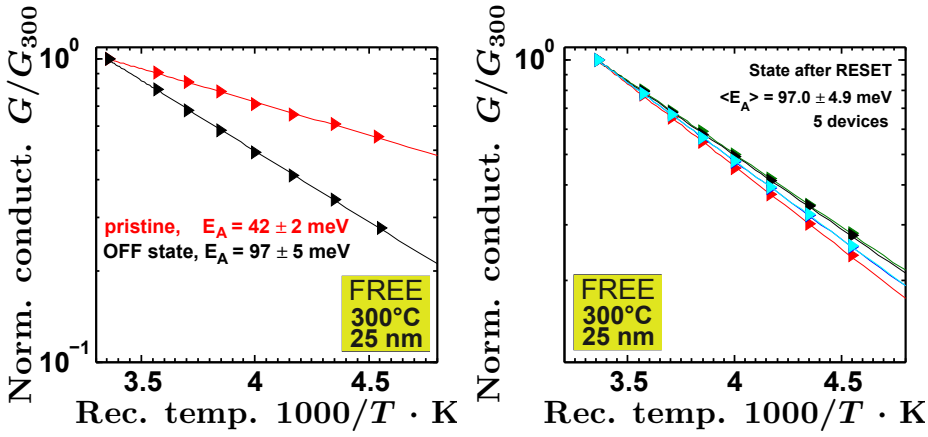

Figure 7.7: Activation energy of conduction of forming-free TiO_{2-x} ReRAM before RESET, and after RESET in (a) and for several devices after RESET in (b).

Table 7.3: Activation energies of conduction in pristine, OFF, and ON state for different standard and forming-free TiO_{2-x} ReRAM cells.

sample	crystallinity	Activation energy E_a / meV		
		pristine	OFF	ON
3nm, 300 °C	a	320	123 ± 40	89 ± 18
15nm, 200 °C	a	137	82 ± 33	70 ± 29
15nm, 300 °C	nc	112	66	42
forming-free	nc	42 ± 2	97 ± 5	42 ± 2

7.5 Working Principle of Forming-free TiO_{2-x}- ReRAM

For the following discussion it has to be defined that the general formula TiO_{2-x} which has been used in this thesis should stand for a titanium oxide composition which is oxygen deficient as compared to titanium dioxide TiO_2. Any identification of the detailed structure is beyond the scope of this study, while this work (see chapter 3) and also others microstructural investigation clearly showed the presence of Magnéli-type Ti_nO_{2n-1} phases. In chapter 5 the reduced forming voltage in nano-crystalline TiO_{2-x} is already discussed. Well-conducting crystalline phases of TiO_{2-x} built up a well-conducting network which allows to electroform the crystalline TiO_{2-x} film along preferential paths.
Within such crystalline TiO_{2-x} films parasitic current can flow which can be circumvented by the changed device design. This makes forming-free TiO_{2-x} ReRAM feasible. Negative sweeps initially reset forming-free TiO_{2-x} ReRAM. The maximum RESET current depends on the device area, nevertheless the SET process shows a filamentary character while counter-8-wise operation. Summing up all these informations, a model can developed to explain forming-free resistive switching in TiO_{2-x}thin films might be explained by the following working principle.
During RESET oxygen ions O^{2-} are repelled from the active interface, here the Pt bottom electrode. The oxygen ions can oxidize the oxygen vacancies $V_O^{\bullet\bullet}$ nested in the well-conducting crystalline phases to less oxygen deficient conducting phases.

$$y \cdot O^{-2} + TiO_{2-x} \rightleftharpoons 2y \cdot e^{-} + TiO_{2-x+y} \tag{7.2}$$

In addition, electrically induced internal oxidation from Magnéli-phase to Magnéli-phase of different order number *n* caused by electromigration might be possible, too [45]. In any case, the conducting network might represent a number of conducting filaments which are destructed by the redox reaction in the vicinity of the active Pt bottom electrode as depicted in figure 7.8. This might explain the area dependence of the pristine forming-free TiO_{2-x} ReRAM devices and the dot-like conduction through the nano-crystalline TiO_{2-x} film revealed by the LC-AFM measurements. While the SET process, the morphologically pre-defined paths are partly reduced by the reverse redox reaction in the vicinity of the active interface. By this, oxygen vacancies might be created along these paths leading to the well-conducting TiO_{2-x} phases. These are most probable Magnéli-type phases because of the presence of the rutile phase in the TiO_{2-x} thin films as already discussed in chapter 3. But the material is not reconfigurated back to the randomly oxygen deficiency of the pristine state. Here, it has to be taken into account that the electrical stimulus might cause a concurring growth of conducting filaments along the morphologically pre-defined paths. Reasonably, the resistive switching should be of filamentary-type nature as illustrated in step (4) of figure 7.8 which was found for the forming-free TiO_{2-x} ReRAM devices. This might also explains, why the SET voltage of the forming-free TiO_{2-x} ReRAM is about a factor 2 higher as compared to forming and SET voltage of the nano-crystalline standard TiO_{2-x} ReRAM devices as discussed in chapter 6. In standard devices the conducting network is not destructed before the electroforming which might result in a partly further reduction of a preferred path (see chapt. 6). In contradiction to that, in forming-free TiO_{2-x} ReRAM devices these

paths were destructed in the vicinity of the active interface which might result in a wider gap which needs to be electroreduced while the SET process. As a consequence, the SET voltage of forming-free TiO_{2-x} ReRAM should be higher as compared to standard TiO_{2-x} ReRAM.

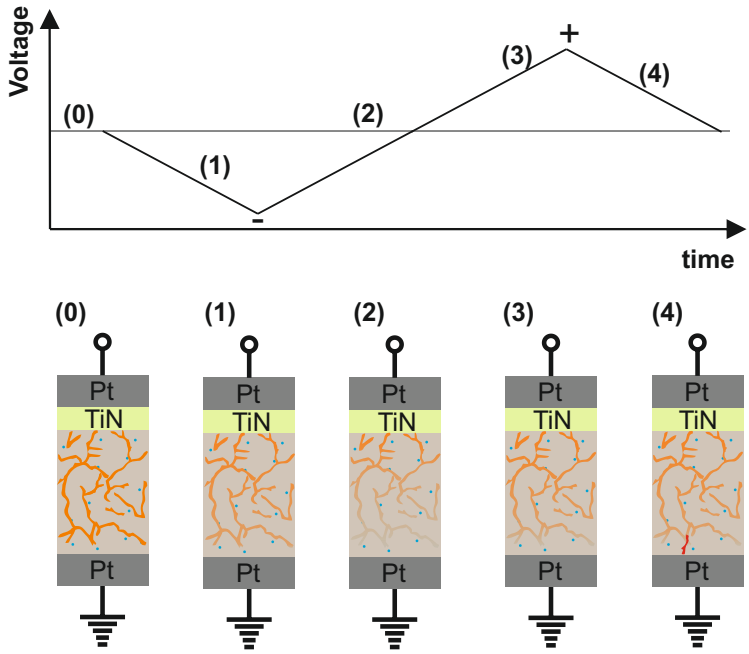

Figure 7.8: Working principle of forming-free TiO_{2-x} ReRAM. A negative bias on top destructs already conducting filaments along preferential paths from (0) to (2). A single filament is reactivated from (3) to (4).

Similar to crystalline TiO_{2-x}, the initial RESET was also observed in WO_x devices [191]. This is of interest, because in WO_x also exhibits Magnéli-phases [192, 193, 194]. Therefore, the question arises if the concept of forming-free ReRAM of highly-conducting pristine state could be observed in other materials which act as a host for Magnéli-phases, for example vanadium oxide [195, 196, 197]. However, this concept represents a very elegant way to circumvent electroforming with improved resistive switching properties as compared to standard TiO_{2-x} ReRAM devices. In HfO_x, the forming voltage increases with decreasing effective device area. Zhang et. al argue that the probability to electroform at low voltages is related to the defect density [25]. As a consequence, less forming paths are present in devices of smaller feature size. Thus, forming-free TiO_{2-x} ReRAM in this work might not necessarily show such behavior since the achieved TiO_{2-x} contains filament-like conducting phases which connect bottom and top electrode more or less. Therefore, forming-free TiO_{2-x} ReRAM should show excellent scaling properties.

In summary, the overall knowledge on material design and properties of TiO_{2-x} films combined

with the engineered device preparation enabled the suggestion and realization of forming-free TiO_{2-x} thin films devices.

CHAPTER

EIGHT

SUMMARY AND OUTLOOK

In this thesis an ALD process was developed to meet the requirements for the growth of TiO_{2-x} thin films for resistive switching applications. These requirements are oxygen deficient TiO_{2-x} thin films which contain well-conducting phases. Furthermore, the ALD process should enable the conformal deposition of dense, pinhole-free, shadow-free TiO_{2-x} films with excellent control of the thin film thickness and roughness for the fabrication of vertical ReRAM structures with high integration density.

In a first step, different water-based thermal ALD processes were analyzed for the growth of TiO_{2-x} by three different precursors, namely titanium-isopropoxide (TTIP), tetrakis-dimethyl-amido-titanium (TDMAT), and tris-(dimethylamido)-mono-(N,N'-diisopropyl-dimethyl-amido-guanidinato)-titanium (TiA_3G_1). The processes can be characterized by the difference mainly in the ALD cycle time.
Utilizing the TTIP/H_2O process creates thin TiO_{2-x} films which exhibit the development of pyramid-shaped large crystallites of the anatase phase. This happens above a temperature of approximately 240 °C. The crystallites were found to induce a transition to higher growth rates and an increase in the TiO_{2-x} thin film roughness. Generally, this growth behavior makes integration of TiO_{2-x} into ReRAM difficult. The characterization of the TDMAT/H_2O process, the TiA_3G_1/H_2O process, and the crystallization of the achieved TiO_{2-x} thin films revealed that the thin films roughness, the growth of crystallites, and the phase composition are controlled by three parameters: the thin film thickness, the temperature, and the process time. For the crystallization of TiO_{2-x} a minimum amount of material is required characterized by a minimum thin film thickness. In which phase amorphous TiO_{2-x} from an initial nuclei crystallizes or a crystalline TiO_2 phase transforms into a certain TiO_2 phase is determined by the crystallization kinetics. The crystallization kinetics take into account the free energy of transformation of a certain phase and the time for the development of crystallites described by the Johnson-Mehl-Avrami-Kolmogorov equation. The free energy of transformation is different for each phase of TiO_2 which is activated at a certain temperature. The size of the crystallites is determined by the growth time which can be described in case of an ALD process time. Reasonably, the

concurring growth of the anatase, brookite, and rutile TiO_2 phase and the amount of a specific TiO_2 phase is controlled by the ALD growth temperature and the ALD cycle time. By this, the observed correlation between ALD cycle time and the growth of large anatase-type crystallites of pyramid shape were explained: the longest cycle time was given by the TTIP/H_2O process which lead to largest crystallites as compared to the TDMAT/H_2O process where the process time was reduced by nearly 50 %. Additionally, the reduction in process time allowed to grow TiO_{2-x} films which contain the rutile phase which can be transformed to the well-conducting Magnéli-phases. Such films were found to be oxygen deficient by means of XPS analysis and exhibited the corundum Ti_2O_3 structure. This indicates the presence of Magnéli-phases within the oxygen deficient TiO_2 thin films since the thermodynamic consideration allow to infer that the Magnéli-phases are preferably grown as compared to the corundum Ti_2O_3. Furthermore, the consideration of the influence of the crystallization on the growth behavior enabled precise control over thin film thickness and conformal growth which is disturbed in case of the TTIP/H_2O process. Large anatase-type crystallite facettes were demonstrated to cause the transition to higher growth rates by the influence of the hydroxylic group density on the Ti precursor chemisorption utilizing water-based ALD processes. ALD cycle time dependent cross-over experiments on the TDMAT/H_2O process revealed that the reduction of the ALD cycle time additionally suppressed the growth of such large anatase crystallites and the amount of the anatase phase. As a consequence the growth transition was inhibited which resulted in smooth ALD TiO_{2-x} thin films. From this, the modulation of the surface chemistry while the ALD process by the physical crystallization parameters was concluded.

Amorphous and nano-crystalline TiO_{2-x} thin films were integrated utilizing the TDMAT process into nano cross-point devices to elucidate the influence of the crystallinity on the electrical transport and on the resistive switching. The investigation on the electrical transport revealed that the conductivity of the ReRAM devices generally depend on the electric field strength and the defect density of TiO_{2-x} before electroforming takes place. In case of low electrical fields the transport is dominated by hopping processes. The transport in amorphous TiO_{2-x} could be clearly assigned to field-directed Poole-Frenkel emission for high defect concentrations. By this, the conduction behavior in nano-crystalline TiO_{2-x} could be also explained, but the experimentally observed behavior might be additionally attributed to the small polaron hopping mechanism. However, the derived hopping distance changes upon crystallization of TiO_{2-x} from about 0.7 nm to 1.5 nm and the extracted defect density or small polaron density increases with increasing TiO_{2-x} film thicknesses. Above a certain field strength, a second transport channel arised in very thin TiO_{2-x} films (< 5 nm) which was assigned to ejection of electrons over the Schottky barrier at the Pt|TiO_{2-x} interface. Furthermore, temperature dependent measurements revealed activation energies of the conduction of about 42 meV to 112 meV which might be associated with the Magnéli-phases Ti_nO_{2n-1}.
The conduction phenomena were found to influence the electroforming behavior of pristine TiO_{2-x} ReRAM devices. The hopping transport lead to high currents at low electric fields which disabled the breakthrough of the Schottky barrier. From that point of view the Schottky barrier might be regarded as circumvented and no abrupt electroforming to extreme low

ON states should take place. In addition to that, the electrical characterization after electroforming demonstrated that soft electroforming to a non-linear state was preferrentially found for nano-crystalline TiO_{2-x}. Above a certain TiO_{2-x} thickness, the forming voltage settled down to a stable value in nano-crystalline devices which demonstrated a voltage dependence rather than an electric field dependence. Amorphous TiO_{2-x} exhibited inverse behavior: the forming voltage increased with thin film thickness and hard electroforming to low ON states was observed. The difference in electroforming was assigned to the presence of the well-conducting crystalline phases in nano-crystalline TiO_{2-x}. From the presence of such well-conducting phases a conductive network was concluded in which pre-defined conducting filaments might explain the reduced forming voltage. This implies, it is reasonable that electroforming does only bridge a very small non-conducting gap or simply further reduces an existing conductive filament. In pristine amorphous TiO_{2-x} the well-conducting phases do not exist. Therefore, no preferential conducting paths should exist and reasonably need to be created by abrupt hard electroforming at higher voltages.
After electroforming, the resisitive switching experiments demonstrated that no significant qualitative differences exist in the switching behavior between as-deposited amorphous and crystalline TiO_{2-x}. But the resisitive switching properties clearly changed from ultrathin TiO_{2-x} thin films ($\leq 5nm$) to thick TiO_{2-x} devices. Low SET current compliances and low RESET currents of 50μA and 70μA, respectively, were feasible for ultrathin TiO_{2-x} layers which enabled a DC-nonlinearity of about 10. Higher TiO_{2-x} thicknesses resulted in an decrease of the DC-nonlinearity and the memory window with comparable switching parameters. However, the comparison of the electroforming and resisitive switching hysteresis of nano-crystalline TiO_{2-x} exhibited that the forming and SET voltage agree independent of the SET current compliance. Furthermore, the hysteresis curves of the electroforming and the subsequent switching cycles agreed in their non-linear behavior. This accordance might be addressed to the well-conducting TiO_{2-x} phases. Nonetheless, these phases might create parasitic paths which strongly influence the resistive switching performance with respect to the memory window and the high switching currents.

To improve the resistive switching properties such parasitic paths have to be eliminated. The most striking parasitic path which short-circuits the device in parallel was successfully eliminated by changing the device design from a closed TiO_{2-x} film over the whole nano cross-point structure to a device where TiO_{2-x} is only in between the intercept point of the electrode lines. The second parasitic path, simply concurring conductive filaments, can be actively destroyed. This was demonstrated by changing the resistive switching sequence. Instead of electroforming of the device to a lower resistance state, the devices were initially reseted to actively circumvent the electroforming step and achieve the forming-free TiO_{2-x} ReRAM. By the elimination of the parasitic paths, it was possible to reduce the current compliance for the SET process and the memory window was increased by a factor at minimum greater than 10 as compared to standard TiO_{2-x} ReRAM. The working principle of such forming-free TiO_{2-x} ReRAM is suggested to be based on the active destruction of already existing parallel conductive paths which were inferred from the area-dependent initial RESET process. This further implies that this cannot

be regarded as OFF-forming as compared to area-related resistive swiching in 8-wise operation because filamentary switching was demonstrated for these forming-free TiO_{2-x} devices. In summary, the achieved knowledge on the material properties were put into application to realize forming-free TiO_{2-x} ReRAM by an engineered solution.

Future down-scaling of the minimum feature size should increase the initial ON device state because of the area dependent conduction. This makes the presented forming-free memory concept very promising. However, the current density remains and the thickness of the functional layer might be a drawback for 3D ReRAM memory, for example Vertical ReRAM. Reasonably, further investigations on such forming-free TiO_{2-x} memory are required to shift the pristine ON state to higher values and decrease the switching current density. One possibility to achieve this goal might be further tuning of the device resistance as a function of the material properties of ultrathin TiO_{2-x} films. For this, further ALD process development is needed to grow the well-conducting Magnéli-phases of TiO_2 already within ultrathin TiO_{2-x} films. The investigation of the ALD processes in this thesis demonstrated that their growth is favored at high deposition temperatures utilizing thermal ALD with water as counter-reactant. Thus, better precursors are needed to enable ALD windows with higher upper temperature limit. Such a precursor, namely TiA_3G_1 was already presented in this work. However, Magnéli-phases does not only exist in TiO_{2-x}, other binary oxides can contain Magnéli-phases, too. Therefore, the extension of this study on such materials might be worthwhile to elucidate the physical and resistive switching properties to map the route to forming-free low power initial ON ReRAM.

BIBLIOGRAPHY

[1] G.W. Burr. Storage Class Memory - Towards a disruptively low-cost solid-state non-volatile memory. IBM, 2010.

[2] G.E. Moore. Cramming more components onto integrated circuits (Reprinted from Electronics, pg 114-117, April 19, 1965). *Proc. IEEE*, 86(1):82–85, JAN 1998.

[3] Semiconductor Industry Association. The International Technology Roadmap for Semiconductors: Emerging Research Devices. Technical report, Semiconductor Industry Association, 2011 Edition.

[4] R. Waser, R. Dittmann, G. Staikov, and K. Szot. Redox-Based Resistive Switching Memories - Nanoionic Mechanisms, Prospects, and Challenges. *Adv. Mater.*, 21(25-26):2632–2663, 2009.

[5] D. Jeong, R. Thomas, R. Katiyar, J. Scott, H. Kohlstedt, A. Petraru, and C. Hwang. Emerging memories: Resistive switching mechanisms and current status. *Rep. Prog. Phys.*, 75(7), 2012.

[6] J. J. Yang and R. S. Williams. Memristive Devices in Computing System: Promises and Challenges. *ACM JETC*, 9(2):11/1–, 2013.

[7] T. W. Hickmott. Low-frequency negative resistance in thin anodic oxide films. *J. Appl. Phys.*, 33:2669–2682, 1962.

[8] W. R. Hiatt and T. W. Hickmott. Bistable switching in niobium oxide diodes. *Appl. Phys. Lett.*, 6:106–108, 1965.

[9] G. Dearnaley, A.M. Stoneham, and D.V. Morgan. Electrical Phenomena in Amorphous Oxide Films. *Rep. Prog. Phys.*, 33(11):1129–&, 1970.

[10] S. R. Ovshinsky. Reversible electrical switching phenomena in disordered structures. *Phys. Rev. Lett.*, 21(20):1450–3, 1968.

[11] D. Adler, M. S. Shur, M. Silver, and S. R. Ovshinsky. Threshold switching in chalcogenide-glass thin films. *J. Appl. Phys.*, 51(6):3289–309, 1980.

[12] A. Asamitsu, Y. Tomioka, H. Kuwahara, and Y. Tokura. Current switching of resistive states in magnetoresistive manganites. *Nature, Int. Wkly. J Sc.*, 388(6637):50–2, 1997.

[13] M. N. Kozicki, M. Yun, L. Hilt, and A. Singh. Applications of programmable resistance changes in metal-doped chalcogenides. In *Proc. of Solid-State Ionic Devices*, pages 298–309. Center for Solid State Electron Res, Arizona State Univ, Tempe, AZ, USA, J. Electrochem. Soc, 1999.

[14] A. Beck, J. G. Bednorz, C. Gerber, C. Rossel, and D. Widmer. Reproducible switching effect in thin oxide films for memory applications. *Appl. Phys. Lett.*, 77(1):139–41, 2000.

[15] R.S. Williams. How we found the missing memristor. *IEEE Spectr.*, 45(12):24–31, 2008.

[16] J. J. Yang, M. D. Pickett, X. Li, D. A. A. Ohlberg, D. R. Stewart, and R. S. Williams. Memristive switching mechanism for metal/oxide/metal nanodevices. *Nat. Nanotechnol.*, 3(7):429, 2008.

[17] A. Sawa, T. Fujii, M. Kawasaki, and Y. Tokura. Interface resistance switching at a few nanometer thick perovskite manganite active layers. *Appl. Phys. Lett.*, 88(23):232112–1–3, 2006.

[18] Sieu D. Ha, Gulgun H. Aydogdu, and Shriram Ramanathan. Metal-insulator transition and electrically driven memristive characteristics of SmNiO3 thin films. *Appl. Phys. Lett.*, 98(1), JAN 3 2011.

[19] C. Cario, L.and Vaju, B. Corraze, V. Guiot, and E. Janod. Electric-Field-Induced Resistive Switching in a Family of Mott Insulators: Towards a New Class of RRAM Memories. *Adv. Mater.*, 22(45):5193+, DEC 1 2010.

[20] I. Valov, R. Waser, J. R. Jameson, and M. N. Kozicki. Electrochemical metallization memories-fundamentals, applications, prospects. *Nanotechnol.*, 22(25):254003/1–22, 2011.

[21] G.W. Burr, M.J. Breitwisch, M. Franceschini, D. Garetto, K. Gopalakrishnan, B. Jackson, B. Kurdi, C. Lam, L.A. Lastras, A. Padilla, B. Rajendran, S. Raoux, and R.S. Shenoy. Phase change memory technology. *J. Vac. Sci. Technol., B*, 28(2):223–262, MAR 2010.

[22] S. Raoux, D. Ielmini, M. Wuttig, and I. Karpov. Phase change materials. *MRS Bull.*, 37(2):118–123, FEB 2012.

[23] D. Ielmini, R. Bruchhaus, and R. Waser. Thermochemical resistive switching: materials, mechanisms, and scaling projections. *Phase Transit.*, 84(7):570–602, 2011.

[24] B. Govoreanu, G. S. Kar, Y-Y. Chen, V. Paraschiv, S. Kubicek, A. Fantini, I. P. Radu, L. Goux, S. Clima, R. Degraeve, N. Jossart, O. Richard, T. Vandeweyer, K. Seo, P. Hendrickx, G. Pourtois, H. Bender, L. Altimime, D. J. Wouters, J. A. Kittl, and M. Jurczak. 10x10nm2 Hf/HfOx Crossbar Resistive RAM with Excellent Performance, Reliability

and Low-Energy Operation. In *2011 IEEE International Electron Devices Meeting - IEDM '11*, page S31.6. IEDM Tech. Dig., 2011.

[25] Z. Zhang, Y. Wu, H.-S.P. Wong, and S.S. Wong. Nanometer-scale hfox rram. *IEEE EDL*, 34:1005–1007, 2013.

[26] C. Nauenheim, C. Kuegeler, S. Trellenkamp, A. Ruediger, and R. Waser. Phenomenological considerations of resistively switching TiO_2 in nano crossbar arrays. In *Proceedings of 10th International Conference on Ultimate Integration of Silicon, March 18-20, Aachen*, pages 135–138. Proceedings of 10th International Conference on Ultimate Integration of Silicon, 2009.

[27] C. Nauenheim, C. Kuegeler, A. Ruediger, and R. Waser. Investigation of the electroforming process in resistively switching TiO_2 nanocrosspoint junctions. *Appl. Phys. Lett.*, 96(12):122902, 2010.

[28] T. Menke. *Investigation of the electroforming and resistive switching mechanisms in Fe-doped $SrTiO_3$ thin films*. PhD thesis, 2010.

[29] R. Muenstermann, T. Menke, R. Dittmann, and R. Waser. Coexistence of Filamentary and Homogeneous Resistive Switching in Fe-doped $SrTiO_3$ Thin-Film Memristive Devices. *Adv. Mat.*, 22(43):4819, 2010.

[30] C. Kügeler, M. Meier, R. Rosezin, S. Gilles, and R. Waser. High density 3D memory architecture based on the resistive switching effect. *Solid State Electron.*, 53(12):1287–1292, 2009.

[31] I. Baek, C. Park, H. Ju, D. Seong, H. Ahn, J. Kim, M. Yang, S. Song, E. Kim, S. Park, C. Park, C. Song, G. Jeong, S. Choi, H. Kang, and C. Chung. Realization of vertical resistive memory (VRRAM) using cost effective 3D process. In *Technical Digest - International Electron Devices Meeting, IEDM*, pages 31.8.1–31.8.4. Technical Digest - International Electron Devices Meeting, IEDM, 2011.

[32] D. S. Jeong, H. Schroeder, and R. Waser. Coexistence of bipolar and unipolar resistive switching behaviors in a $Pt/TiO_2/Pt$ stack. *Electrochem. Solid State Lett.*, 10(8):G51–G53, 2007.

[33] K. Kim, B. Choi, M. Lee, G. Kim, S. Song, J. Seok, J. Yoon, S. Han, and C. Hwang. A detailed understanding of the electronic bipolar resistance switching behavior in Pt/TiO2/Pt structure. *Nanotechnol.*, 22(25), 2011.

[34] C. Kügeler, J. Zhang, S. Hoffmann-Eifert, S. K. Kim, and R. Waser. Nanostructured resistive memory cells based on 8-nm-thin TiO_2 films deposited by atomic layer deposition. *J. Vac. Sci. Technol. B*, 29(1):1AD01/1–5, 2011.

[35] H. Schroeder and D.S. Jeong. Resistive switching in a $pt/tio_2/pt$ thin film stack: a candidate for a non-volatile reram. *Microelectron. Eng.*, 84:1982–1985, 2007.

[36] D. S. Jeong, H. Schroeder, U. Breuer, and R. Waser. Characteristic electroforming behavior in Pt/TiO_2/Pt resistive switching cells depending on atmosphere. *J. Appl. Phys.*, 104(12):123716/1–8, 2008.

[37] J. J. Yang, F. Miao, M. D. Pickett, D. A. A. Ohlberg, D.R. Stewart, C. N. Lau, and R. S. Williams. The mechanism of electroforming of metal oxide memristive switches. *Nanotechnol.*, 20(21):215201, 2009.

[38] J. P. Strachan, J. J. Yang, R. Muenstermann, A. Scholl, G. Medeiros-Ribeiro, D. R. Stewart, and R. S. Williams. Structural and chemical characterization of TiO_2 memristive devices by spatially-resolved NEXAFS. *Nanotechnol.*, 20(48):485701, 2009.

[39] R. Muenstermann, J. J. Yang, J. P. Strachan, G. Medeiros-Ribeiro, R. Dittmann, and R. Waser. Morphological and electrical changes in TiO_2 memristive devices induced by electroforming and switching. *Phys. Status Solidi-Rapid Res. Lett.*, 4(1-2):16–18, 2010.

[40] J. P. Strachan, M. D. Pickett, J. J. Yang, S. Aloni, A. L. D. Kilcoyne, G. Medeiros-Ribeiro, and R. S. Williams. Direct Identification of the Conducting Channels in a Functioning Memristive Device. *Adv. Mater.*, 22(32):3573–3577, 2010.

[41] D.-H. Kwon, K. M. Kim, J. H. Jang, J. M. Jeon, M. H. Lee, G. H. Kim, X.-S. Li, G.-S. Park, B. Lee, S. Han, M. Kim, and C. S. Hwang. Atomic structure of conducting nanofilaments in TiO_2 resistive switching memory. *Nat. Nanotechnol.*, 5(2):148–153, 2010.

[42] D. S. Jeong, H. Schroeder, and R. Waser. Mechanism for bipolar switching in a Pt/TiO_2/Pt resistive switching cell. *Phys. Rev. B*, 79(19):195317/1–10, 2009.

[43] J. P. Strachan, D. B. Strukov, J. Borghetti, J. J. Yang, G. Medeiros-Ribeiro, and R. S. Williams. The switching location of a bipolar memristor: chemical, thermal and structural mapping. *Nanotechnol.*, 22:254015, 2011.

[44] M. D. Pickett, D. B. Strukov, J. L. Borghetti, J. J. Yang, G. S. Snider, D. R. Stewart, and R. S. Williams. Switching dynamics in titanium dioxide memristive devices. *J. Appl. Phys.*, 106(7):074508, 2009.

[45] K. Szot, M. Rogala, W. Speier, Z. Klusek, A. Besmehn, and R. Waser. TiO_2 - a prototypical memristive material. *Nanotechnol.*, 22(25):254001/1–21, 2011.

[46] J.F. Watts and J. Wolstenholme. *An Introduction to Surface Analysis by XPS and AES*. Wiley and Sons, 2002.

[47] J Sherman. The Theoretical Derivation of Fluorescent X-ray Intensities from Mixtures. *Spectrochim. Acta*, 7(5):283–306, 1955.

[48] L. Spieß, G. Teichert, R. Schwarzer, H. Behnken, and C. Genzel. *Moderne Röntgenbeugung*. Vieweg, 2009.

[49] Henning Dieker. Charakterisierung von Chalkogenidlegierungsschichten mittels Röntgenreflektometrie und spektroskopischer Ellipsometrie. Master's thesis, RWTH, 2002.

[50] Hansjörg Weiss. *Untersuchung gasochrom schaltender Wolframoxide*. PhD thesis, RWTH, 2002.

[51] F. Stanglmeier, B. Lengeler, W. Weber, H. Gobel, and M. Schusrer. Determination of the Dispersive Correction f(E) to the Atomic Form-Factor From X-Ray Reflection. *Acta Crystallogr., Sect. A*, 48(4):626–639, JUL 1 1992.

[52] L NEVOT and P CROCE. Characterization of Surfaces by Grazing X-ray Reflection - Application to Study of Polishing of Some Silicate-glasses. *Revue de Physique Applique*, 15(3):761–779, 1980.

[53] D Windover, N Armstrong, JP Cline, PY Hung, and A Diebold. Characterization of atomic layer deposition using X-ray reflectometry. In DG Seiler, AC Diebold, R McDonald, CR Ayre, RP Khosla, and EM Secula, editors, *Characterization and Metrology for ULSI Technology 2005*, volume 788 of *AIP Conference Proceedings*, pages 161–165, 2 HUNTINGTON QUADRANGLE, STE 1NO1, MELVILLE, NY 11747-4501 USA, 2005. Natl Inst Stand & Technol; SEMATECH; Amer Phys Soc; Natl Sci Fdn; Semiconductor Res Corp; Semiconductor Equipment & Mat Int; Univ Texas Dallas; Semiconductor Int, AMER INST PHYSICS. 5th Conference on Characterization and Metrology for ULSI Technology, Richardson, TX, MAR 15-18, 2005.

[54] WH Bragg and WL Bragg. The reflection of X-rays by crystals. *Proc. R. Soc. London, Ser. A*, 88(605):428–438, JUL 1913.

[55] B Mierzwa and J Pielaszek. Smoothing of low-intensity noisy X-ray diffraction data by Fourier filtering: application to supported metal catalyst studies. *J. Appl. Crystallogr.*, 30(1, Part 5):544–546, OCT 1 1997.

[56] D.B. Williams and C.B. Carter. *Transmission Electron Microscopy - A Textbook for Material Science*. Springer, 2009.

[57] M. Ardenne. Improvements in electron microscopes, 1937.

[58] G. Binnig, C. F. Quate, and Ch. Gerber. Atomic Force Microscope. *Phys. Rev. Lett.*, 56:930–933, Mar 1986.

[59] A. Kurowski, J. W. Schultze, and G. Staikov. Initial stages of Ni-P electrodeposition: growth morphology and composition of deposits. *Electrochem. Commun.*, 4(7):565–569, July 2002.

[60] C.V. Raman. *Molecular Diffraction of Light*. University of Calcutta, 1922.

[61] J.R. Ferraro, K. Nakamoto, and C.W. Brown. *Introductory Raman Spectroscopy*. Elsevier, 2003.

[62] C. Kittel. *Einführung in die Festkörperphysik*. Oldenbourg Verlag, 2006.

[63] H.G. Tompkins and E.A. Irene, editors. *Handbook of Ellipsometry*. Springer, 2005.

[64] K. Kopitzki and P. Herzog. *Einführung in die Festkörperphysik*. Teubner, 2007.

[65] J Tauc, editor. *Amorphous and Liquid Semiconductors*. Plenum Press, 1974.

[66] Lakeshore Crytronics, Inc. *User's Manual TTPX Probe Station*.

[67] V.B. Aleskovskii. *Russ. J. Appl. Chem.*, 47:2247, 1974.

[68] RL Puurunen. Surface chemistry of atomic layer deposition: A case study for the trimethylaluminum/water process. *J. Appl. Phys.*, 97(12), JUN 15 2005.

[69] T Suntola and J Antson. Atomic Layer Epitaxy, 1977.

[70] L Niinisto, J Paivasaari, J Niinisto, M Putkonen, and M Nieminen. Advanced electronic and optoelectronic materials by Atomic Layer Deposition: An overview with special emphasis on recent progress in processing of high-k dielectrics and other oxide materials. *Phys. Status Solidi A*, 201(7):1443–1452, MAY 2004.

[71] M Ritala. *Handbook of thin films*, volume 2. Elsevier, 2002.

[72] Ville Miikkulainen, Markku Leskela, Mikko Ritala, and Riikka L. Puurunen. Crystallinity of inorganic films grown by atomic layer deposition: Overview and general trends. *J. Appl. Phys.*, 113(2), JAN 14 2013.

[73] M. Reiners, K. Xu, N. Aslam, A. Devi, R. Waser, and S. Hoffmann-Eifert. Study of the Growth and Crystallization of TiO_2 Thin Films by ALD using a Novel Amido Guanidinate Titanium Source and Tetrakis-dimethylamido-titanium. *Chem. Mater.*, 2013.

[74] T Hantanpää, M. Ritala, and M. Leskelä. Precursors as enablers of ALD technology: Contributions from University of Helsinki. *Coord. Chem. Rev.*, 257:3297–3322, 2013.

[75] Jaakko Niinisto, Kaupo Kukli, Mikko Heikkila, Mikko Ritala, and Markku Leskela. Atomic Layer Deposition of High-k Oxides of the Group 4 Metals for Memory Applications. *Adv. Eng. Mater.*, 11(4):223–234, APR 2009.

[76] A. Devi. 'Old Chemistries' for new applications: Perspectives for development of precursors for MOCVD and ALD applications. *Coord. Chem. Rev.*, 257:3332–3384, 2013.

[77] Timothee Blanquart, Jaakko Niinisto, Marco Gavagnin, Valentino Longo, Venkateswara R. Pallem, Christian Dussarrat, Mikko Ritala, and Markku Leskela. Novel Heteroleptic Precursors for Atomic Layer Deposition of TiO_2. *Chem. Mater.*, 24(17):3420–3424, SEP 11 2012.

[78] D. M. Hausmann, P. de Rouffignac, A. Smith, R. Gordon, and D. Monsma. Highly conformal atomic layer deposition of tantalum oxide using alkylamide precursors. *Thin Solid Films*, 443(1-2):1–4, October 2003.

[79] W. J. Maeng and H. Kim. Thermal and plasma-enhanced ALD of Ta and Ti oxide thin films from alkylamide precursors. *Electrochem. Solid State Lett.*, 9(6):G191–G194, 2006.

[80] M. K. Wiedmann, M. J. Heeg, and C. H. Winter. Volatility and High Thermal Stability in Tantalum Complexes Containing Imido, Amidinate, and Halide or Dialkylamide Ligands. *Inorganic Chemistry*, 48(12):5382–5391, June 2009.

[81] M. K. Wiedmann and C. H. Winter. Atomic layer deposition of tantalum oxide using a new amidinate-based precursor. *Abstracts of Papers of the American Chemical Society*, 237, March 2009.

[82] Yoann Tomczak, Kjell Knapas, Markku Sundberg, Markku Leskela, and Mikko Ritala. In Situ Reaction Mechanism Studies on the New (BuN)-Bu-t=M(NEt2)(3) -Water and (BuN)-Bu-t=M(NEt2)(3) - Ozone (M = Nb,Ta) Atomic Layer Deposition Processes. *Chem. Mater.*, 24(9):1555–1561, MAY 8 2012.

[83] Y Senzaki, S Park, H Chatham, L Bartholomew, and W Nieveen. Atomic layer deposition of hafnium oxide and hafnium silicate thin films using liquid precursors and ozone. *J. Vac. Sci. Technol., A*, 22(4):1175–1181, JUL-AUG 2004.

[84] K Kukli, M Ritala, J Lu, A Harsta, and M Leskela. Properties of HfO_2 thin films grown by ALD from hafnium tetrakis(ethylmethylamide) and water. *J. Electrochem. Soc.*, 151(8):F189–F193, 2004.

[85] Minha Seo, Yo-Sep Min, Seong Keun Kim, Tae Joo Park, Jeong Hwan Kim, Kwang Duk Na, and Cheol Seong Hwang. Atomic layer deposition of hafnium oxide from tert-butoxytris(ethylmethylamido)hafnium and ozone: rapid growth, high density and thermal stability. *J. Mater. Chem.*, 18(36):4324–4331, 2008.

[86] Ke Xu, Andrian P. Milanov, Harish Parala, Christian Wenger, Canan Baristiran-Kaynak, Kaoutar Lakribssi, Teodor Toader, Claudia Bock, Detlef Rogalla, Hans-Werner Becker, Ulrich Kunze, and Anjana Devi. Atomic Layer Deposition of HfO_2 Thin Films Employing a Heteroleptic Hafnium Precursor. *Chem. Vap. Deposition*, 18(1-3):27–35, MAR 2012.

[87] Jaakko Niinisto, Kaupo Kukli, Mikko Heikkila, Mikko Ritala, and Markku Leskela. Atomic Layer Deposition of High-k Oxides of the Group 4 Metals for Memory Applications. *Adv. Eng. Mater.*, 11(4):223–234, APR 2009.

[88] X. Shi, H. Tielens, S. Takeoka, T. Nakabayashi, L. Nyns, C. Adelmann, A. Delabie, T. Schram, L. Ragnarsson, M. Schaekers, L. Date, R. Schreutelkamp, and

S. Van Elshocht. Development of ALD $HfZrO_x$ with TDEAH/TDEAZ and H_2O. *J. Electrochem. Soc.*, 158(1):H69–H74, 2011.

[89] P.J. Haines, editor. *Principles of Thermal Analysis and Calorimetry*. Royal Society of Chemistry, 2002.

[90] J. Dykyj, J. Svoboda, R. C. Wilhoit, M. Frenkel, and K. R. Hall. 2 Hydrocarbons, C8 to C9. In *Landolt-Börnstein - Group IV Physical Chemistry*, volume 20 A.

[91] J. Dykyj, J. Svoboda, R. C. Wilhoit, M. Frenkel, and K. R. Hall. 2 Hydrocarbons, C1 to C7. In *Landolt-Börnstein - Group IV Physical Chemistry*, volume 20 A.

[92] K.L. Siefering and G.L. Griffin. Growth-kinetics of CVD TiO_2 - Influence of Carrier Gas. *J. Electrochem. Soc.*, 137(4):1206–1208, APR 1990.

[93] http://www.airproducts.com/~/media/downloads/t/tetrakis-dimethylamino-titanium-tdmat/data-sheets/en-tdmat-datasheet.pdf.

[94] S.K. Kim, S. Hoffmann-Eifert, M. Reiners, and R. Waser. Relation Between Enhancement in Growth and Thickness-Dependent Crystallization in ALD TiO_2 Thin Films. *J. Electrochem. Soc.*, 158(1):D6–D9, 2011.

[95] J. Aarik, J. Karlis, H. Mändar, T. Uustare, and V. Sammelselg. Influence of structure development on atomic layer deposition of TiO_2 thin films. *Appl. Surf. Sci.*, 181(3-4):339 – 348, 2001.

[96] W. D. Kim, G. W. Hwang, O. S. Kwon, S. K. Kim, M. Cho, D. S. Jeong, S. W. Lee, M. H. Seo, C. S. Hwang, Y. S. Min, and Y. J. Cho. Growth characteristics of atomic layer deposited TiO_2 thin films on Ru and Si electrodes for memory capacitor applications. *J. Electrochem. Soc.*, 152(8):C552–C559, 2005.

[97] R. Pheamhom, C. Sunwoo, and D. Kim. Characteristics of atomic layer deposited TiO_2 films and their photocatalytic activity. *J. Vac. Sci. Technol., A*, 24:1535–1539, 2006.

[98] Q. Xie, Y. L. Jiang, C. Detavernier, D. Deduytsche, R. L. Van Meirhaeghe, G. P. Ru, B. Z. Li, and X. P. Qu. Atomic layer deposition of TiO_2 from tetrakis-dimethyl-amido titanium or Ti isopropoxide precursors and H_2O. *J. Appl. Phys.*, 102(8):83521/1–6, 2007.

[99] Q. Xie, J. Musschoot, D. Deduytsche, R. L. Van Meirhaeghe, C. Detavernier, S. Van den Berghe, Y. Jiang, G. Ru, B. Li, and X. Qu. Growth kinetics and crystallization behavior of TiO_2 films prepared by plasma enhanced atomic layer deposition. *J. Electrochem. Soc.*, 155:H688–H692, 2008.

[100] Gyeong Taek Lim and Do-Heyoung Kim. Characteristics of TiO_x films prepared by chemical vapor deposition using tetrakis-dimethyl-amido-titanium and water. *Thin Solid Films*, 498(1-2):254 – 258, 2006.

[101] J. W. Elam, M. Schuisky, J. D. Ferguson, and S. M. George. Surface chemistry and film growth during TiN atomic layer deposition using TDMAT and NH_3. *Thin Solid Films*, 436:145–156, 2003.

[102] S. J. Kim, K. Xu, H. Parala, D. Barecca, C. Maccoto, C. Sada, R. Beranek, R.A. Fischer, and A. Devi. Intrinsic Nitrogen-doped CVD-grown TiO_2 Thin Films from All-N-coordinated Ti Precursors for Photoelectrochemical Applications. *Chem. Vap. Deposition*, 19:45–52, 2013.

[103] M. Egashira, S. Kawasumi, S. Kagawa, and T. Seiyama. Temperature Programmed Desoprtion Study of Water Adsorbed on Metal-Oxides .1. Anatase and Rutile. *Bull. Chem. Soc. Jpn.*, 51(11):3144–3149, 1978.

[104] K. Morishige, F. Kanno, S. Ogawara, and S. Sasaki. Hydrated Surfaces of Particulate Titanium-Dioxide Preprared by Pyrolysis of Alkoxide. *J. Phys. Chem.*, 89(20):4404–4408, 1985.

[105] Guido Ketteler, Susumu Yamamoto, Hendrik Bluhm, Klas Andersson, David E. Starr, D. Frank Ogletree, Hirohito Ogasawara, Anders Nilsson, and Miquel Salmeron. The nature of water nucleation sites on TiO_2(110) surfaces revealed by ambient pressure X-ray photoelectron spectroscopy. *J. Phys. Chem. C*, 111(23):8278–8282, JUN 14 2007.

[106] C Arrouvel, M Digne, M Breysse, H Toulhoat, and P Raybaud. Effects of morphology on surface hydroxyl concentration: a DFT comparison of anatase-TiO_2 and gamma-alumina catalytic supports. *J. Catal.*, 222(1):152–166, FEB 15 2004.

[107] S. K. Kim, S. Y. Lee, M. Seo, G. J. Choi, and C. S. Hwang. Impact of O_3 feeding time on TiO_2 films grown by atomic layer deposition for memory capacitor applications. *J. Appl. Phys.*, 102(2):24109/1–6, 2007.

[108] B. Predel. O-Ti (Oxygen-Titanium). In O. Madelung, editor, *Landolt - Börnstein - Group IV Physical Chemistry*, volume 51. SpringerMaterials - The Landolt-Börnstein Database.

[109] P. Waldner and G. Eriksson. Thermodynamic Modelling of the System Titanium-Oxygen. *Calphad*, 23(2):189, 1999.

[110] P. Villars, K. Cenzual, J. Daams, R. Gladyshevskii, O. Shcherban, V. Dubenskyy, V. Kuprysyuk, I. Savysyuk, and R. Zaremba. *TiO_2 rutile*, volume 43A10. SpringerMaterials - The Landolt-Börnstein Database, 2011.

[111] P. Villars, K. Cenzual, J. Daams, R. Gladyshevskii, O. Shcherban, V. Dubenskyy, V. Kuprysyuk, and I. Savysyuk. *TiO_2 anatase*, volume 43A9. SpringerMaterials - The Landolt-Börnstein Database, 2010.

[112] U. Müller. *Inorganic Structural Chemistry*. Wiley & Sons, 2nd edition, 2006.

[113] International Crystal Structure Database.

[114] Leandro Liborio and Nicholas Harrison. Thermodynamics of oxygen defective Magneli phases in rutile: A first-principles study. *Phys. Rev. B*, 77(10), MAR 2008.

[115] L. Liborio, L. Harrison, and G. Mallia. Thermodynamics of Oxygen Defective TiO_2: The Magneli Phases. In *Towards Reality in Nanoscale Materials*, September 2007.

[116] L. Liborio, N. Harrison, and G. Mallia. The Electronic Structure of the Ti_4O_7 Magneli Phase. In *CMSG Scientific Meeting*, 2008.

[117] D. Regonini, A. C. E. Dent, C. R. Bowen, S. R. Pennock, and J. Taylor. Impedance spectroscopy analysis of Ti_nO_{2n-1} Magneli phases. *Mater. Lett.*, 65(23-24):3590–3592, DEC 2011.

[118] R.F. Bartholomew and D.R. Frankl. Electrical Properties of Some Titanium Oxides. *Phys. Rev. Lett.*, 187(3):828–&, 1969.

[119] A.D. Inglis, Y. Lepage, P. Strobel, and C.M. Hurd. Electrical Conductance of Crystalline Ti_nO_{2n-1} for n= 4-9. *J. Phys. C*, 16(2):317–333, 1983.

[120] S. Lakkis, C. Schlenker, B.K. Chakraverty, R. Buder, and M. Marezio. Metal-Insulator-Metal Transitions in Ti_4O_7 Single-Crystals - Crystal Characterization, Specific-Heat, and Electron-Paramagnetic Resonance. *Phys. Rev. B*, 14(4):1429–1440, 1976.

[121] S. Asbrink and A. Magneli. Note on the Structure of Trititanium Pentoxide. *Acta Chem. Scand.*, 11(9):1606–1607, 1957.

[122] S. Asbrink and A. Magneli. Crystal Structure Studies on Trititanium Pentoxide, Ti_3O_5. *Acta Cryst.*, 12(8):575–581, 1959.

[123] Landolt-Börnstein. *Ti_2O_3: crystal structure, lattice parameters, density*, volume 41D. SpringerMaterials - The Landolt-Börnstein Database, 2013.

[124] International centre for diffraction data, diffraction pattern file 29-1360.

[125] Jaan Aarik, Aleks Aidla, VÃino Sammelselg, Teet Uustare, Mikko Ritala, and Markku Leskelä. Characterization of titanium dioxide atomic layer growth from titanium ethoxide and water. *Thin Solid Films*, 370(1-2):163 – 172, 2000.

[126] I. Jogi, M. Pars, J. Aarik, A. Aidla, M. Laan, J. Sundqvist, L. Oberbeck, J. Heitmann, and K. Kukli. Conformity and structure of titanium oxide films grown by atomic layer deposition on silicon substrates. *Thin Solid Films*, 516(15):4855–4862, JUN 2 2008.

[127] A. K. Podshivalova and I. K. Karpov. Thermodynamic analysis of the stability of titanium oxides in the TiO-TiO_2 range. *Russ. J. Inorg. Chem.*, 52(7):1147–1150, JUL 2007.

[128] K Kukli, M Ritala, M Schuisky, M Leskela, T Sajavaara, J Keinonen, T Uustare, and A Harsta. Atomic layer deposition of titanium oxide from TiI_4 and H_2O_2. *Chem. Vap. Deposition*, 6(6):303–310, NOV 2000.

[129] M. Watanabe. Raman spectroscopy of charge-ordered states in Magneli titanium oxides. In T Itoh, K Tanaka, and M Schreiber, editors, *Phys. Status Solidi C*, volume 6 of *Physica Status Solidi C Current Topics in Solid State Physics*, pages 260–263, PAPPELALLEE 3, W-69469 WEINHEIM, GERMANY, 2009. Kyoto Univ, Inst Integrated Cell Mat Sci; HORIBA; Mitsubishi Elect Corp; Spectra Phys KK; USHIO; Wiley VCH, WILEY-V C H VERLAG GMBH. 8th International Conference on Excitonic Processes in Condensed Matter (EXCON 2008), Kyoto, JAPAN, JUN 22-27, 2008.

[130] S. K. Kim, W. D. Kim, K. M. Kim, C. S. Hwang, and J. Jeong. High dielectric constant TiO_2 thin films on a Ru electrode grown at 250 degrees C by atomic-layer deposition. *Appl. Phys. Lett.*, 85(18):4112–4114, NOV 1 2004.

[131] Seong Keun Kim, Susanne Hoffmann-Eifert, Shaobo Mi, and Rainer Waser. Liquid Injection Atomic Layer Deposition of Crystalline TiO_2 Thin Films with a Smooth Morphology from Ti(O-i-Pr)(2)(DPM)(2). *J. Electrochem. Soc.*, 156(8):D296–D300, 2009.

[132] M Avrami. Kinetics of phase change I - General theory. *J. Chem. Phys.*, 7(12):1103–1112, DEC 1939.

[133] W A Johnson and R F Mehl. Reaction kinetics in processes of nucleation and growth. *Trans. Am. Inst. Min. Metall. Pet. Eng.*, 135:416–442, 1939.

[134] Johannes Kalb. *Crystallization kinetics in antimony and tellurium alloys used for phase change recording*. PhD thesis, RWTH, 2006.

[135] P. Scherrer. Bestimmung der Größe und der inneren Struktur von Kolloidteilchen mittels Röntgenstrahlen. *Göttinger Nachrichten Math. Phys.*, 2:98, 1918.

[136] J. Aarik, J. Karlis, H. Mandar, T. Uustare, and V. Sammelselg. Influence of structure development on atomic layer deposition of TiO_2 thin films. *Appl. Surf. Sci.*, 181(3-4):339–348, SEP 21 2001.

[137] K. Vos and H.J. Krusemeyer. Reflectance and Electroreflectance of TiO_2 Single-Crystals.1. Optical-Spectra. *J. Phys. C: Solid State Phys.*, 10(19):3893–3915, 1977.

[138] J Aarik, A Aidla, AA Kiisler, T Uustare, and V Sammelselg. Effect of crystal structure on optical properties of TiO_2 films grown by atomic layer deposition. *Thin Film Solids*, 305(1-2):270–273, AUG 15 1997.

[139] H. Tang, K. Prasad, R. Sanjines, P.E. Schmid, and F. Levy. Electrical and Optical-Properties of TiO_2 Anatase Thin-Films. *J. Appl. Phys.*, 75(4):2042–2047, FEB 15 1994.

[140] G.K. Boschloo, A. Goossens, and J. Schoonman. Photoelectrochemical study of thin anatase TiO_2 films prepared by metallorganic chemical vapor deposition. *J. Electrochem. Soc.*, 144(4):1311–1317, APR 1997.

[141] C.E. Ekuma and D. Bagayoko. Ab-initio Electronic and Structural Properties of Rutile Titanium Dioxide. *Jpn. J. Appl. Phys.*, 50(10, 1), OCT 2011.

[142] H.S. Waff and K. Park. Structure in 2-photon Absoprtion Spectrum of TiO_2 (Rutile). *Phys. Lett. A*, A 32(2):109–&, 1970.

[143] P. J. Hardman, G. N. Raikar, C. A. Muryn, G. van der Laan, P. L. Wincott, G. Thornton, D. W. Bullett, and P. A. D. M. A. Dale. Valence-band structure of TiO_2 along the Γ-Δ- *X* and Γ-Σ- *M* directions. *Phys. Rev. B*, 49:7170–7177, Mar 1994.

[144] M. Landmann, E. Rauls, and W. G. Schmidt. The electronic structure and optical response of rutile, anatase and brookite TiO_2. *J. Phys. Condens. Matter*, 24(19), MAY 16 2012.

[145] S.Y. Chou, P.R. Krauss, and P.J. Renstrom. Imprint lithography with 25-nanometer resolution. *Science*, 272(5258):85–87, APR 5 1996.

[146] M. Meier. *Entwicklung einer Nanotechnologie-Plattform für die Herstellung Crossbar-basierter Speicherarchitekturen*. Key Technologies. Forschungszentrum Jülich GmbH Zentralbibliothek, Verlag, 2009.

[147] Florian Lentz. *Integration of redox-based resistive switching memory devices*. PhD thesis, Forschungszentrum Jülich, 2013.

[148] R. Tsu and L. Esaki. Tunneling in a Finite Superlattice. *Appl. Phys. Lett.*, 22(11):562–564, 1973.

[149] Andreas Gehring. *Simulation of Tunneling in Semiconductor Devices*. PhD thesis, Technische Universität Wien, 2003.

[150] K.F. Schuegraf and C.M. Hu. Hole Injection SiO_2 Breakdown Model for Very-low Voltage Lifetime Extrapolation. *IEEE Trans. Electron Devices*, 41(5):761–767, MAY 1994.

[151] M.A. Kinch. Electronic-properties of hgcdte. *J. Vac. Sci. Technol.*, 21(1):215–219g, 1982.

[152] Q.K. Yang, F. Fuchs, J. Schmitz, and W. Pletschen. Investigation of trap-assisted tunneling current in inas/(gain)sb superlattice long-wavelength photodiodes. *Appl. Phys. Lett.*, 81(25):4757–4759, DEC 16 2002.

[153] W. Schottky. For the theory of semiconductor junction and peak rectifier . *Z. Angew. Phys.*, 113(5-6):367–414, MAY 1939.

[154] E.H. Rhoderick and R.H. Williams. *Metal-Semiconductor Contacts*. Clarendon Press, 2 edition, 1988.

[155] B.J. Baliga. *Advanced Power Rectifier Concepts*. Springer, 2009.

[156] S.M. Sze, C.R. Crowell, and D. Khang. Photoelectric determination of image force dielectric constant for hot electrons in Schottky barriers. *J. Appl. Phys.*, 35(8):2534–&, 1964.

[157] A. Rose. Space-Charge-Limited Currents In Solids. *Phys. Rev. Lett.*, 97(6):1538–1544, 1955.

[158] P. Mark and W. Helferich. Space-Charge-Limited Currents in Organic Crystals. *J. Appl. Phys.*, 33(1):205–&, 1962.

[159] Sergei Baranovski. *Charge Transport in Disordered Solids with Applications in Electronics*. Wiley, 2006.

[160] J Frenkel. On pre-breakdown phenomena in insulators and electronic semi-conductors. *Phys. Rev. Lett.*, 54(8):647–648, OCT 1938.

[161] Karlheinz Seeger. *Halbleiterphysik: eine Einführung*. Vieweg, 1992.

[162] R.M. Hill. Poole-Frenkel Conduction in Amorphous Solids. *Philos. Mag.*, 23(181):59–&, 1971.

[163] A.K. Jonscher. Electronic properties of amorphous dielectric films. *Thin Solid Films*, 1:213–234, 1967.

[164] H. Fröhlich, H. Pelzer, and S Zienau. Properties of Slow Electrons in Polar Materials. *Phil. Magazine Series 7*, 41:221–242, 1950.

[165] H. Fröhlich. Electrons in Lattice Fields. *Adv. Phys.*, 3(11):325, 1954.

[166] H. Böttger and V.V. Bryksin. *Hopping Conduction in Solids*. VCH, 1985.

[167] N.F. Mott and E.A. Davis. *Electronic Processes in Non-crystalline Materials*. Clarendon Press, 1979.

[168] J. Borghetti, D. B. Strukov, M. D. Pickett, J. J. Yang, D. R. Stewart, and R. S. Williams. Electrical transport and thermometry of electroformed titanium dioxide memristive switches. *J. Appl. Phys.*, 106(12):124504/1–5, 2009.

[169] N. Aaron Deskins and Michel Dupuis. Electron transport via polaron hopping in bulk TiO_2: A density functional theory characterization. *Phys. Rev. B: Condens. Matter*, 75(19), MAY 2007.

[170] A.K. Ghosh, F.G. Wakim, and R.R. Addiss. Photoelectronic processes in rutile. *Physical Review*, 184(3):979–988, 1969. cited By (since 1996)94.

[171] R.G. Breckenridge and W.R. Hosler. Electrical Properties of Titanium Dioxide Semiconductors. *Phys. Rev. Lett.*, 91(4):793–802, 1953.

[172] A.A. Ansari and A. Qadeer. Memory Switching in Thermally Grown Titanium-Oxide Films. *J. Phys. D: Appl. Phys.*, 18(5):911–917, 1985.

[173] S. Schramm, J. Hoffmann, and Ch Jooss. Transport and ordering of polarons in CER manganites PrCaMnO. *J. Phys. Condens. Matter*, 20(39), OCT 1 2008.

[174] J.G. Traylor, H.G. Smith, R.M. Nicklow, and M.K. Wilkinso. Lattice Dynamics of Rutile. *Phys. Rev. B: Condens. Matter*, 3(10):3457–&, 1971.

[175] I. Jacob, R. Moreh, O. Shahal, and A. Wolf. Effective and Debye Temperatures of Ti in TiC, TiO_2, and TiH_2. *Phys. Rev. B: Condens. Matter*, 35(1):8–12, JAN 1 1987.

[176] A. Yildiz and D. Mardare. Polaronic transport in TiO_2 thin films with increasing Nb content. *Philos. Mag.*, 91(34):4401–4409, 2011.

[177] Kwang-Hyuk Choi, Kwun-Bum Chung, and Han-Ki Kim. d-orbital ordering of oxygen-deficient amorphous and anatase TiO_{2-x} channels for high mobility thin film transistors. *Appl. Phys. Lett.*, 102(15), APR 15 2013.

[178] L. Forro, O. Chauvet, D. Emin, L. Zuppiroli, H. Berger, and F. Levy. High-Mobility n-type Charge-Carriers in Large Single-Crystals of Anatase (tio_2). *J. Appl. Phys.*, 75(1):633–635, JAN 1 1994.

[179] M. Bonn, F. Wang, J. Shan, T.F. Heinz, and E. Hendry. Ultrafast scattering of electrons in TiO_2. In J Hynes and JT Hynes, editors, *Femtochemistry and Femtobiology: Ultrafast Events in Molecular Science*, pages 517–520. Elsevier Science BV, 2004. 6th International Conference on Femtochemistry, Paris, FRANCE, JUL 06-10, 2003.

[180] E. Hendry, F. Wang, J. Shan, T.F. Heinz, and M. Bonn. Electron transport in TiO_2 probed by THz time-domain spectroscopy. *Phys. Rev. B: Condens. Matter*, 69(8), FEB 2004.

[181] E. Hendry, M. Koeberg, B. O'Regan, and M. Bonn. Local field effects on electron transport in nanostructured TiO_2 revealed by terahertz spectroscopy. *Nano Lett.*, 6(4):755–759, APR 2006.

[182] H. Schroeder, A. Zurhelle, S. Stemmer, A. Marchewka, and R. Waser. Resistive switching near electrode interfaces: Estimations by a current model. *J. Appl. Phys.*, 113(5):053716 1–6, 2013.

[183] D.K. Schroeder. *Semiconductor Material and Device Characterization*. Wiley-Interscience, 2006.

[184] F. Miao, J. J. Yang, J. Borghetti, G. Medeiros-Ribeiro, and R. S. Williams. Observation of two resistance switching modes in TiO_2 memristive devices electroformed at low current. *Nanotechnol.*, 22(25):254007/1–7, 2011.

[185] D. Li, M. Li, J. Zahid, F.band Wang, and H. Guo. Oxygen vacancy filament formation in TiO_2: A kinetic Monte Carlo study. *J. Appl. Phys.*, 112(7), OCT 1 2012.

[186] R. Rosezin, C. Nauenheim, S. Trellenkamp, C. Kuegeler, and R. Waser. Electrical properties of Pt interconnects for passive crossbar memory arrays. *Microelectron. Eng.*, 86:2275–2278, 2009.

[187] J. P. Strachan, M. D. Pickett, J. J. Yang, S. Aloni, A. L. D. Kilcoyne, G. Medeiros-Ribeiro, and R. S. Williams. Direct Identification of the Conducting Channels in a Functioning Memristive Device. *Adv. Mater.*, 22(32):3573–3577, 2010.

[188] J. P. Strachan, D. B. Strukov, J. Borghetti, J. J. Yang, G. Medeiros-Ribeiro, and R. S. Williams. The switching location of a bipolar memristor: chemical, thermal and structural mapping. *Nanotechnol.*, 22:254015, 2011.

[189] C.R. Hermes. *Interaction between Redox-Based Resistive Switching Mechanisms*. PhD thesis, RWTH Aachen, 2012.

[190] F. Nardi, S. Larentis, S. Balatti, D. Gilmer, and D. Ielmini. Resistive switching by voltage-driven ion migration in bipolar RRAMPart I: Experimental study. *IEEE Trans. Electron Devices*, 59(9):2461–2467, 2012.

[191] W. C. Chien, Y. R. Chen, Y. C. Chen, A. T. H. Chuang, F. M. Lee, Y. Y. Lin, E. K. Lai, Y. H. Shih, K. Y. Hsieh, and C. Y. Lu. A Forming-free WOx Resistive Memory Using a Novel Self-aligned Field Enhancement Feature with Excellent Reliability and Scalability. In *International Electron Devices Meeting (IEDM), San Francisco, CA*. 2010 international electron devices meeting - technical digest, 2010.

[192] U. Schwingenschlögl. *The Interplay of Structural and Electronic Properties in Transition Metal Oxides*. PhD thesis, Universität Augsburg, 2003.

[193] D. B. Migas, V. L. Shaposhnikov, V. N. Rodin, and V. E. Borisenko. Tungsten oxides. I. Effects of oxygen vacancies and doping on electronic and optical properties of different phases of WO_3. *J. Appl. Phys.*, 108(9), NOV 1 2010.

[194] D. B. Migas, V. L. Shaposhnikov, and V. E. Borisenko. Tungsten oxides. II. The metallic nature of Magneli phases. *J. Appl. Phys.*, 108(9), NOV 1 2010.

[195] U. Schwingenschlögl, V. Eyert, and U. Eckern. The metal-insulator transition of the Magneli phase V_4O_7: Implications for V_2O_3. *Europhys. Lett.*, 64(5):682–688, DEC 2003.

[196] U. Schwingenschlögl, V. Eyert, and U. Eckern. From VO_2 to V_2O_3: The metal-insulator transition of the Magneli phase V_6O_{11}. *Europhys. Lett.*, 61(3):361–367, FEB 2003.

[197] U. Schwingenschlögl and V. Eyert. The vanadium Magneli phasesV_nO_{2n-1}. *Ann. Phys.*, 13(9):475–510, SEP 2004.

Band / Volume 22
Fabrication of Nanogaps and Investigation of Molecular Junctions by Electrochemical Methods
Z. Yi (2012), 132 pp
ISBN: 978-3-89336-812-9

Band / Volume 23
Thermal Diffusion in binary Surfactant Systems and Microemulsions
B. Arlt (2012), 159, xlvi pp
ISBN: 978-3-89336-819-8

Band / Volume 24
Ultrathin Gold Nanowires - Chemistry, Electrical Characterization and Application to Sense Cellular Biology
A. Kisner (2012), 176 pp
ISBN: 978-3-89336-824-2

Band / Volume 25
Interaction between Redox-Based Resistive Switching Mechanisms
C. R. Hermes (2012), iii, 134 pp
ISBN: 978-3-89336-838-9

Band / Volume 26
Supported lipid bilayer as a biomimetic platform for neuronal cell culture
D. Afanasenkau (2013), xiv, 132 pp
ISBN: 978-3-89336-863-1

Band / Volume 27
15th European Workshop on Metalorganic Vapour Phase Epitaxy (EWMOVPE XV) June 2-5, 2013, Aachen, Germany
A. Winden (Chair) (2013)
ISBN: 978-3-89336-870-9

Band / Volume 28
Characterization, integration and reliability of HfO_2 and $LaLuO_3$ high-κ/metal gate stacks for CMOS applications
A. Nichau (2013), xi, 177 pp
ISBN: 978-3-89336-898-3

Band / Volume 29
The role of defects at functional interfaces between polar and non-polar perovskite oxides
F. Gunkel (2013), X, 162 pp
ISBN: 978-3-89336-902-7

Band / Volume 30
Parallelisation potential of image segmentation in hierarchical island structures on hardware-accelerated platforms in real-time applications
S. Suslov (2013), xiv, 211 pp
ISBN: 978-3-89336-914-0

Band / Volume 31
Carrier mobility in advanced channel materials using alternative gate dielectrics
E. Durğun Özben (2014), 111 pp
ISBN: 978-3-89336-941-6

Band / Volume 32
Electrical characterization of manganite and titanate heterostructures
A. Herpers (2014), ix, 165 pp
ISBN: 978-3-89336-948-5

Band / Volume 33
Oxygen transport in thin oxide films at high field strength
D. Weber (2014), XII, 115 pp
ISBN: 978-3-89336-950-8

Band / Volume 34
Structure, electronic properties, and interactions of defects in epitaxial GaN layers
P. H. Weidlich (2014), 139 pp
ISBN: 978-3-89336-951-5

Band / Volume 35
Defect Engineering of $SrTiO_3$ thin films for resistive switching applications
S. Wicklein (2014), xi, 144 pp
ISBN: 978-3-89336-963-8

Band / Volume 36
Integration and Characterization of Atomic Layer Deposited TiO_2 Thin Films for Resistive Switching Applications
M. Reiners (2014), xiv, 166 pp
ISBN: 978-3-89336-970-6

Information / Information
Band / Volume 36
ISBN 978-3-89336-970-6

JÜLICH
FORSCHUNGSZENTRUM